How to obtain equivalent occupant protection levels in vehicle independently of vehicle mass and size?

Pascal Delannoy
Safran Engineering, SAFRAN Group
France

Jean Philippe Lepretre
CERAM, UTAC CERAM Group
France

Paper number 13-0007

ABSTRACT

Recent accident studies [3] show and confirm that occupant severity in frontal car to car accident depends on vehicle mass and size.

Despite the introduction of the Frontal Impact regulation ECE R94, the aggressivity rates of heavy vehicles in front to front accidents are mostly unchanged or worse in some countries. A difference between cars which comply with R94 compared to all ages of cars has been observed. This phenomenon has a direct influence on injury rates of light cars compared to heavy ones.

However, this situation is not a 'fait accompli' and can be solved by changing front end force and compartment strength difference amongst cars mainly responsible for this situation.

This paper evaluates and explains why the current frontal impact test using deformable element did not solve this problem and shows its impact on accident data.

It proposes also some different approaches of possible improvements in test protocol and car design for solving this main passive safety issue. Slight modifications will allow light cars to reach the same level of protection as heavy cars in frontal impact accident.

Possible reductions in severe injuries and fatalities are forecast based on the slight modifications to the test protocol. This will allow rates of serious injury and fatalities in light cars to more closely match those in heavy cars.

The influence of vehicle mass on injury severity rate cannot be completely eliminated. However, the effects could be reduced. The same severity rate for vehicles of different mass and size will remain an unreachable goal. However, reducing and harmonizing impact severity rates among vehicles in a regulatory test is one of the first priorities to reduce the number of accident victims.

INTRODUCTION

Frontal impact car to vehicle accidents represent about 30% of all car occupant fatalities, whereas single vehicle frontal impact stands for 15% of these fatalities [3] [4]. According to that, car to car accident is one of the most important issues to reduce and solve in terms of road fatalities and severely injured.

Frontal impact crash protection is legislated for in Europe UNECE Regulation 94.

Under a GRSP informal working group in Geneva a review of the requirements of Regulation 94 has been initiated which should potentially lead to proposals to amend this Regulation. One of the problems found during preliminary work performed was that the accident data available to review the current frontal impact situation in Europe was limited.

TRL was commissioned by the European Commission (EC) to perform a comprehensive European accident study for frontal impact [3] to help prioritize potential future changes to frontal impact legislation for both the short and longer term. In July 2010, TRL published "Technical assistance and economic analysis in the field of legislation pertinent to the issue of automotive safety: provision of information and services on the subject of accident analysis for the development of legislation on frontal impact protection," for the European Commission.

Over the past ten years, with introduction of regulation, rating, insurance test and pedestrian vehicle front end design has changed a lot. Solutions have been optimized to comply with the R94 regulation and self protection, but not to reduce aggressivity in case of car to car frontal impact accident. Both configurations are not considering in

the same time, improving safety against fix obstacles was considered as the priority at that time.

This paper aims at bringing evidence of the impact of UNECE R94 regulation on car designs and the need to amend and correct its side effect to converge towards equivalent severity rates for all vehicles independent of their mass and size. This approach will allow covering on one hand single and one the other hand car to car accident in the same time.

RELEVEVANCE OF VEHICULE AGRESSIVITY

The "aggressivity" metric was used to investigate the relationship between vehicle mass and its partner protection. This was defined by Gabler and Hollowell (1998) as follows:

$$Aggressivity = \frac{Driver\ fatalities\ in\ collision\ partner}{Number\ of\ crashes\ of\ subject\ vehicle}$$

Generally, as vehicle mass or size increases, aggressivity also increases. This relationship is true and observed for all countries, and for all combinations of vehicle age.

The aggressivity of R94 vehicles in impacts with other R94 vehicles is generally less than the aggressivity of R94 vs all vehicles. As the fleet becomes saturated with Regulation 94 compliant vehicles this suggests that casualty rates will reduce and the aggressivity problem will be lessened.

However, the differences in aggressivity between mass categories for R94 vs R94 vehicles is greater than for R94 vs All and indeed the aggressivity for vehicles > 1600 kg is for R94 vs R94 vehicles is equal or greater than for all ages vs all ages. (**Figure 1 and 2**).

This suggests that the introduction of R94 may be making the situation worse in terms of aggressivity (partner protection), although self protection may be improving as aggressivity overall is decreasing..

This means that the aggressivity problem in a R94 compliant fleet is worse than before Regulation 94 was introduced for certain categories of vehicles.

Improved occupant protection against fixed and rigid obstacle may have contributed to the increased 'aggressiveness' of vehicle front ends towards other vehicles, especially for heavy vehicles that need to absorb their own kinetic energy.

This important issue is not yet treated.

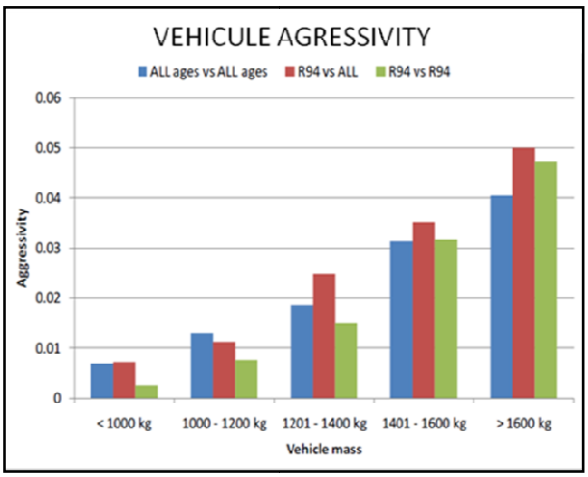

[3] Figure 1: Vehicle aggressivity from national data in Germany split by vehicle mass

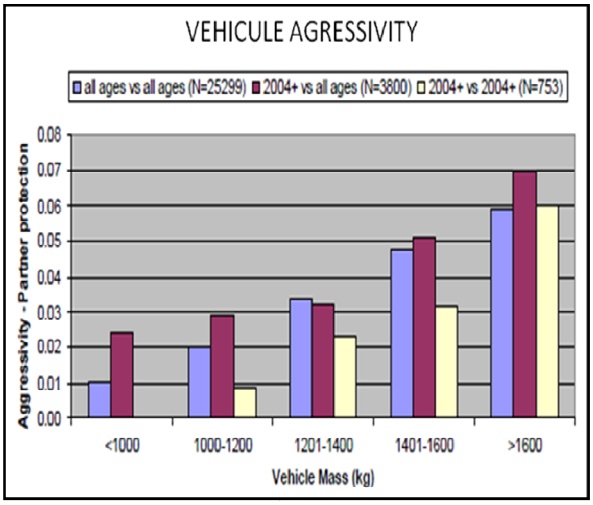

[3] Figure 2: Vehicle aggressivity from national data France split by mass

RELEVANCE OF SEVERITY RATE

Definition of severity rate

Severity rate (SR) is defined as the proportion of fatal and serious injuries observed in the considered car model (internal injuries)

$$Severity\ proportion = \frac{Fatal + Serious\ drivers}{Fatal + Serious + Slight\ drivers}$$

The following figures show it as a function of the vehicle weight for cars that comply with R94 against All.

Distributions in different countries (**Figure 3 and 4**) are similar in terms of level and evolution.

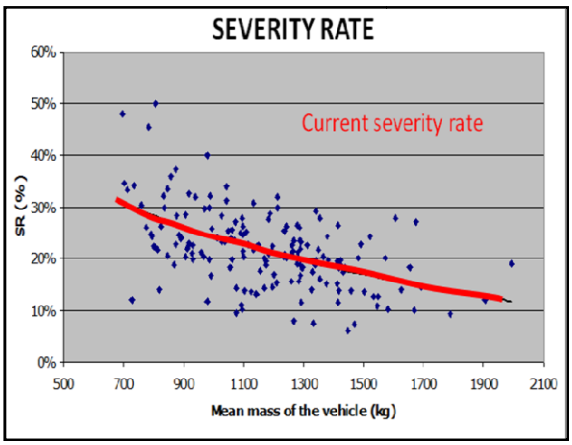

[2] Figure 3: Current severity rate situation from national France - R94 vs all cars

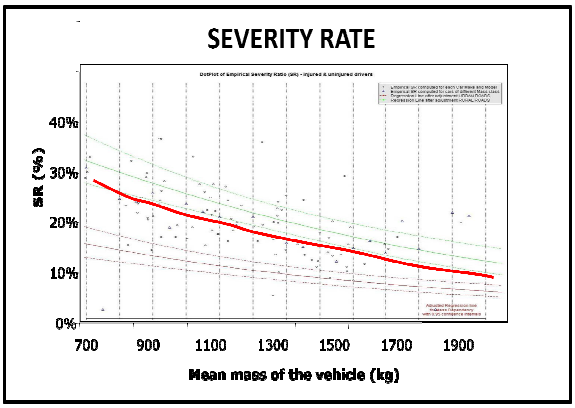

[2] Figure 4: Current severity rate situation from national Germany- R94 vs all cars

Figures 3 and 4 clearly illustrate that severity rates decrease as mass of the cars increase.

This shows that the chance to be killed or seriously injured in a frontal car to car accident is three time higher in the light car than a heavy one. The protection level in case of a frontal accident is clearly mass dependent. However, this situation is not a 'fait accompli' and can be improved.

Explanation of severity rate curve

In case of car to car accident, homogeneous severity rate is dependent upon a correct distribution of the kinetic energy between the two vehicles involved.

Contrary to certain perceived ideas, the mass plays no significant role in the energy distribution. In fact, the force deflection is the main parameter; the weaker vehicle absorbing the energy even it is the heavy one.

If one vehicle supplies higher force than other, it stopsdeforming, and then all the remaining energy is absorbed by the other vehicle. In the following example (**Figure 5**) by virtue of its greater stiffness (force deformation), the vehicle on the right stops deforming, immediately resulting in a larger deformation of vehicle on the left.

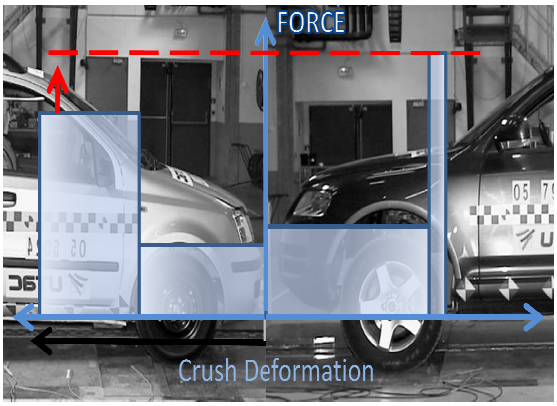

Figure 5: Force mismatch responsible for higher severity rate for light car

Adequate situation to solve this problem

To solve this problem, the two cars involved must supply approximately similar deformation forces to absorb their share of the impact energy. In other words, both cars should provide an acceptable force matching (**Figure 6**).

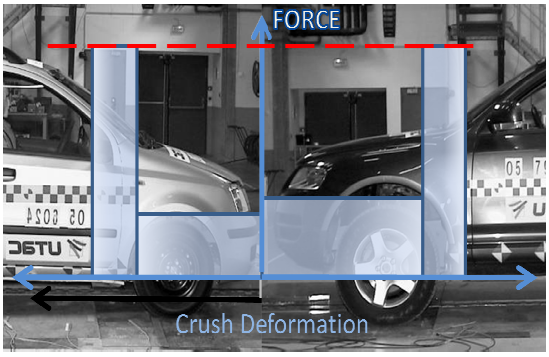

Figure 6: Ideal energy absorption to obtain equivalent severity rate

Unfortunately, this situation is difficult to reach because the most common situation is a difference in force that makes the homogeneous deformation and the adequate energy absorption distribution unreachable.

Unreachable because the heavy car must provide an acceptable level of self protection. In case of single obstacle accident, its structure generates higher force, by design, than a small car to compensate for its greater mass.

But it is not the only one parameter that explains higher force level. The test protocol today using weak deformable element is also partly responsible for this situation.

The approximately constant energy absorbed by the barrier makes the test more severe for heavy cars.

Because of this, heavy cars are penalized two times:

- by their mass,
- by the test protocol.

Even if there are no obvious solutions to compensate for the higher mass problem, it is easy to address the test protocol problem.

RELEVANCE OF ECE R94 ON THIS SITUATION

Vehicles are designed to fulfill ECE R94 using EEVC barrier. However, over time and with the new generation of vehicles which are safer and stiffer, now the barrier fully collapses and vehicles bottom out against rigid wall behind.
Hence, the energy absorbed by the barrier is now more or less constant independent of vehicle size, so the severity of the test depends on the vehicle's mass. This means that the test severity represented by EES (Energy Equivalent Speed) is mass dependent and rises up with the mass (**figure 7**)

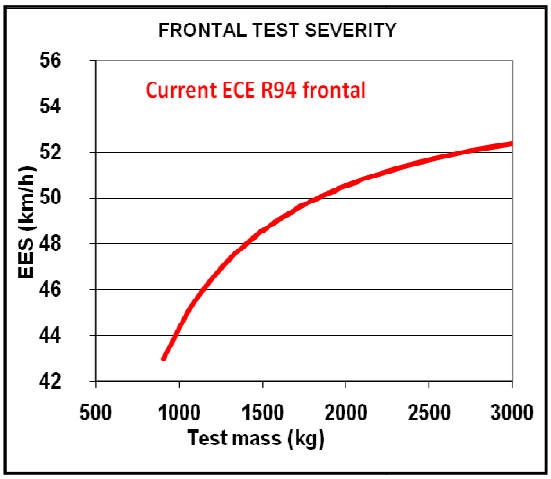

Figure 7: ECE R94Frontal test severity

So in order to reach the same level of self-protection, cars designed to comply with the deformable barrier test which bottom out, results directly in even stiffer heavy cars.

The test severity for a 2000 kgs mass car is 16% more severe than for a 1000 kgs ones.

Current ODB barrier is not yet adapted to the new generation of cars. It was raised by EEVC WG 15 in its final report [3] .This test severity which is dependent on the vehicle mass is partly responsible for the aggressity level and severity rate observed.

Therefore, it is urgent to harmonize the test severity for vehicle range mass to reach a homogeneous fleet that lead to better balance in terms of severity rates.

INFLUENCE ON CURRENT DESIGN

The current situation observed by studies ***(figure 1 and 2)*** directly comes from this test severity inhomogeneity.

Force deformation determines the distribution of energy between the two vehicles. If one of these vehicles stops deforming, because it is stiffer, then all the remaining energy is absorbed by the other vehicle

Due to the specific nature of self-protection tests (more stringent for large vehicles), these improvements have driven manufacturers to increase the stiffness not only of their small vehicles, but that of larger ones also. Large vehicles which due to their design are stiffer already...

In effect, the quest for similar intrusion performance, whether for a small or a large vehicle, leads naturally to greater stiffness in the front unit and passenger compartment.
Figures 9 and 10 explain how the increase of deformation loads has allowed the degree of passenger-compartment intrusion to be significantly reduced. Note that large vehicles - even if they are for the most part longer - require higher deformation loads.
In recent years, all car manufacturers have made significant progresses in structures and restraint systems.

Kinetic energy and Energy absorbed

By laws of physics, heavy cars must absorb more energy than small ones.

Figure 8: Amount of energy to be absorbed by light and heavy car in current frontal offset test

Part of the amount of additional energy is absorbed by the front but also by the compartment. However, the front end is not long enough to absorb the full additional energy (**figure 10 and 9**).

Figure 9: Force level and Energy absorbed for light car

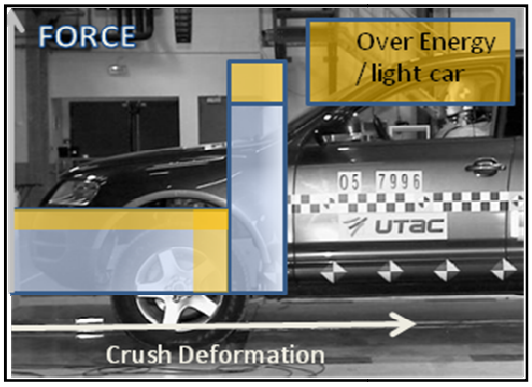

Figure 10. Current front end design of heavy car to absorb over energy compare to light car

Reducing the intrusion level for single accident involves increasing front force deformation of the front end but also of passenger compartment.

This increase in force deformation is likely to be greater for heavy vehicles.

The difference in force levels has been measured in offset tests (**Figure 11**). The maximum force generated by a 2000 kg car can be twice the force generated by a 1000 kg one.

In this condition with lack of force matching, adequate energy distribution between vehicles is unreachable and severity rate cannot be harmonized.

These force deformations increases have already been proven dangerous for older-generation vehicles, but now are also proving to be detrimental for vehicles of the same generation.

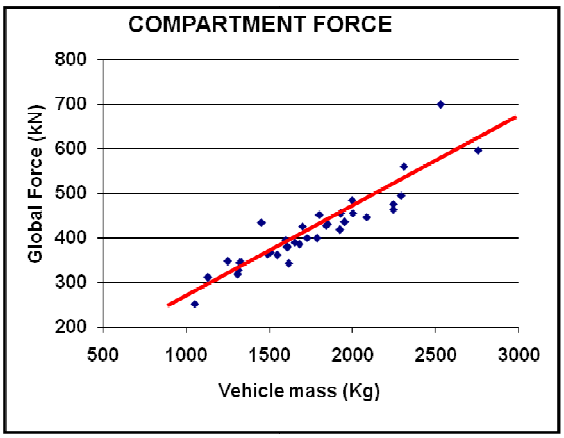

Figure 11. Global force generated by compartment (measured on offset test)

Heavy cars cannot be developed today with force deformations that match with small ones.

The severity rate curves cannot be improved without changing this trend.

POSSIBLE IMPROVEMENTS

The main issue is to switch towards adapted designs that reduce force mismatch and indirectly severity rate differences.

There are two possibilities for improving the situation. The first one is to adapt the car design to the current regulation, the second is to change the test protocol towards a better comprehensive one that solve the side effect introduced by the current deformable barrier.

Keep the current R94 test protocol and change the vehicle design

To obtain acceptable force matching independent of vehicle mass, two possibilities have been proposed for limiting the compartment force:

- increase intrusion level in compartment space,
- increase front end overhang.

<u>Intrusion level</u>

Limiting compartment force for better compartment force balance is one of possibilities to solve the problem.

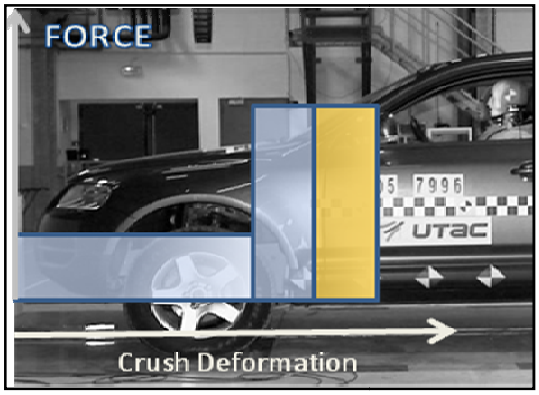

Figure 12: increase compartment intrusion

However, the self protection level would be seriously compromised with higher intrusion in the compartment space.
Even if this solution is a good answer to better force mismatch, it is not acceptable for self protection.
The risk associated with compartment intrusion is too important to accept this design.

Increase overhang

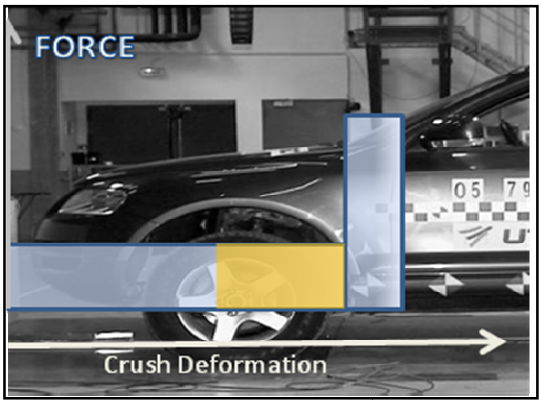

Figure 13: increase overhang to absorb over energy

This solution allows absorption of the additional energy from the mass and the test protocol in the front end and limits the compartment force. Unfortunately, this front end design is not realistic.

The trend is to reduce size of this part of the car instead of increasing it, in order to give more space in the compartment for occupants. Furthermore, it is counter productive for reducing mass and CO2 emissions.

Change the current R94 test protocol and adapt vehicle design

To obtain homogenous test severity independent of vehicle mass, three possibilities have been proposed:

- adapt the deformable element to new vehicles generation,
- remove deformable element
- introduce test speed dependent on the vehicle mass

The goal of the different improvements proposed in this chapter is to change the test severity EES towards a stable and constant one independent of mass.
The **figure 14** illustrates this approach to switch the curve from the red that represent the current situation to the blue one that represents the target for the future.
The blue severity is more appropriate for having a chance to reduce the severity rate.

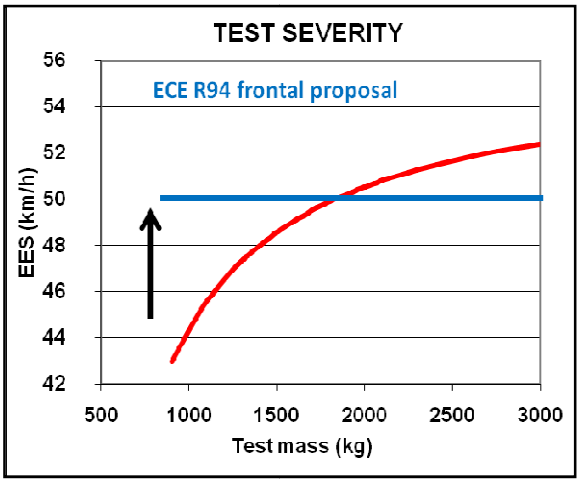

Figure 14: possible test severity harmonization among vehicle masses

Introduce test speed depending on vehicle mass

According to the behavior of the barrier which bottoms out and absorbs a constant amount of energy independently of the car mass, one possibility is to introduce a test speed depending on the kerb weight of the tested vehicle.

This solution can be adopted without any change in the test protocol. The heavy car would be tested at lower speed than light car to switch towards a constant test severity.

Rule makers could decide the test severity (52 kph for example) and by easy calculation, the test speed curve could be defined.

However, another issue regarding aggressivity (structural interaction) highlighted by expert communities as a priority will not be solved by this solution.

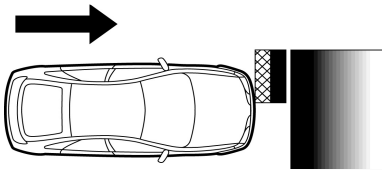

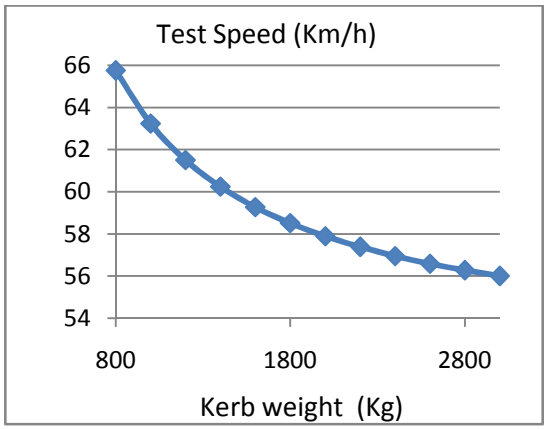

Figure 16: test speed corresponding to a test severity of 52 kph

This approach for limiting test severity for heavy car was adopted in part by Euro NCAP **[1]**. Aware of that situation and the risk of increasing aggressivity of heavy cars,the Euro NCAP test protocol fixes the test speed to 56 km/h for vehicles above 2500 kg and 8 seats and more.

Adapt deformable element to new car generation

Change the deformable element to a new one able to absorb more energy that makes the bottoming out phenomenon rare and allows heavy cars to put more energy into the barrier than light ones.

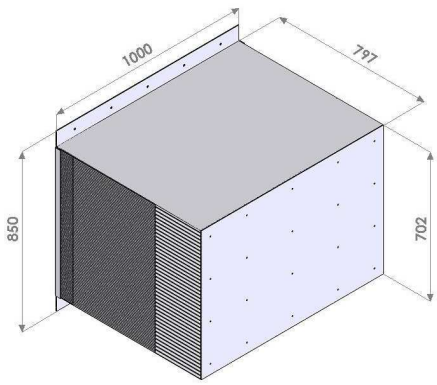

Figure 15: Progressive Deformable Barrier [10]

The PDB barrier showed good capability for absorbing different amounts of energy. Thus it seems possible to normalize test severity with the use of the deformable element, which will allow for controlling other parameters, such as partner protection and structural interaction [10]. The PDB barrier also showed its capability to answer the problem of heavy cars. NHTSA considers after numerous evaluations that PDB performed as designed for heavy vehicle [5].

Remove the current deformable element

This solution is the easiest and the cheapest approach to solve the problem.

The current ODB barrier is obsolete and its stiffness is too low for modern vehicle **[7]**. Removing it should be possible without any change in test results. This operation must be accompanied by fixing lower speed equal to the desired test severity.

Without deformable element, the EES is equal to the testing speed, test severity is constant and not dependent on the vehicle mass.

However, even if it solves test severity and creates a better force mismatch, structural interaction will not be improved. For the structural interaction issue, the potential of this solution is limited.

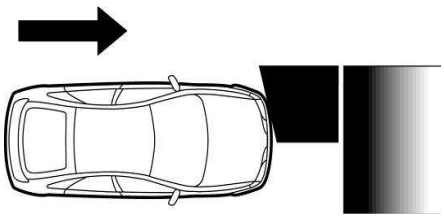

Figure 17: Test severity against rigid wall is equivalent to test speed

IMPACT OF THE CHANGING TEST PROTOCOL

Harmonized test severity gives the opportunity to have better force matching and to solve part of severity rate difference.

Impact on compartment force (figure 18)

The heavy car could be designed according to its mass without higher forces due to increased test severity introduced by the test protocol.

Naturally the light car will become “stiffer” (higher force) and the heavy vehicle will become “weaker” (lower force).

The global force curve generated by the structure will be more “horizontal” which makes the force matching easier to achieve.

However, the perfect horizontal cannot be reached. To compensate for its mass, a heavy vehicle will always have to stay stiffer than a light cone.

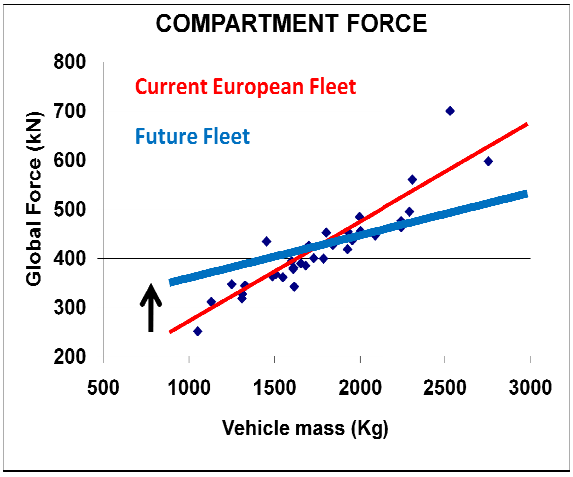

Figure 18: Influence of harmonized test severity on vehicle compartment force

The global force limitation will not be counter productive for self protection against a single obstacle. Due to high stiffness of load, the current efficiency of structure involved in terms of energy absorption in real life accident is limited. Load paths collapse without absorbing the kinetic energy due to lack of stability.

That's why, introducing weaker load paths will improve energy absorption efficiency, and furthermore, load paths will be able to work in many more situations. That it is not the case today.

Impact on severity rate

The lower force differences between light and heavy cars will strongly influence the severity rate distribution (**figure 19**).

Homogeneity of fleets will lead to better force matching in case of car to car accidents. Heavy cars will become less aggressive because of better energy distribution between vehicles involved.

After renewing the fleet, the severity rate curve should decrease, especially for light cars.

Furthermore, the current high difference in terms of Severity Rate will be reduced. However, similar Severity Rate independent of the mass is not reachable. The heavy cars will stay safer than the small car in case of car to car accident.

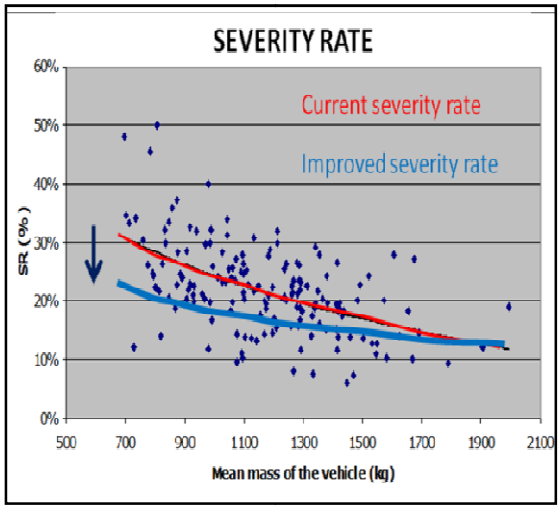

Figure 19: influence of test harmonisation on severity rate

The mass of the car and associated self protection requirements make a horizontal curve unreachable. The Severity Rate curve slope is inversely proportional to the force one.

Impact on safety benefit [4]

An accident analysis carried out in 2010 on population of cars that complied with R94 showed that such evolution of severity rate harmonization, associated to better force mismatch and structural interaction, would lead to avoid 40% of fatalities or severe injuries in head on collision. It represented 7% of victims involved in all impact road accident.

	Head on collisions	All impacts
	Victims reduction (front occupant, belted, head on collision between two cars of conception > 1999 or model year > 2003)	Victims reduction extrapolated to the whole set of car occupants
fatalities and severe injuries	40.3%	7.0%

Figure 20 [4]: reduction in fatalities and serious injuries

Summary

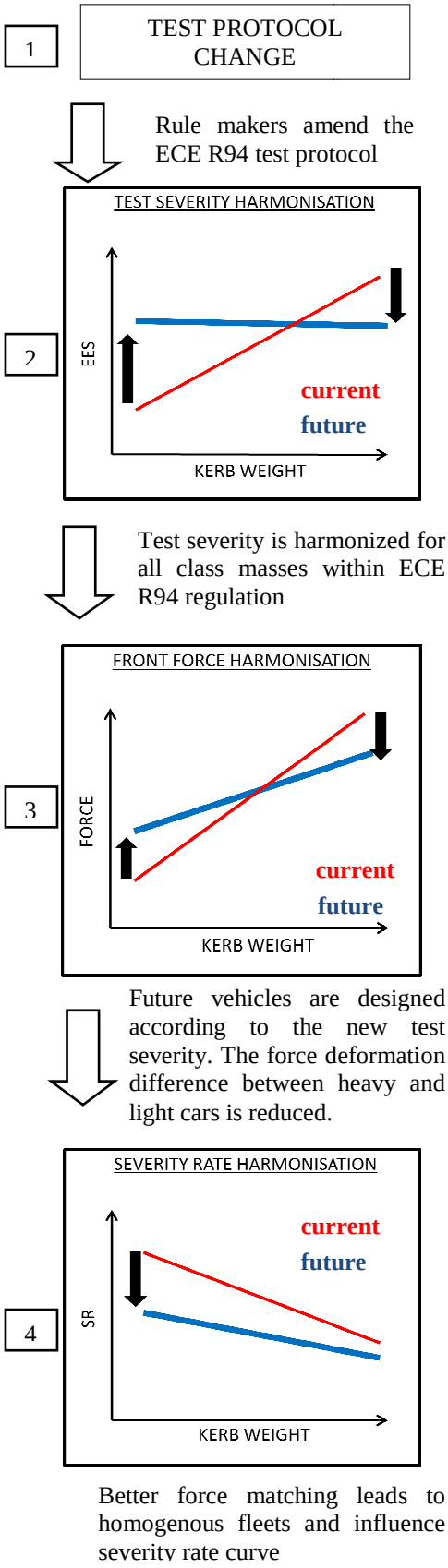

Figure 21: Impact of test protocol change on severity rate

Figure 21 summarizes the global approach and the change in regulation that influence the test severity that influence the vehicle design, that influence the fleet and severity rate and at the end reduce number of fatalities and injured.

CONCLUSIONS

Recent accident studies confirm and show that severity rate harmonization is one of the most effective ways to reduce the number of road accident victims.

Part of the problem comes from the ODB test itself being more severe for heavy vehicle than light one. Hence, the test is considered as mass dependent.

According to different examples shown, adapting the vehicle front end to compensate for the current side effect of the ODB test is not adequate and doable for economic, design and safety reasons.

In contrast, making the test more realistic and adapting it, should be introduced as a first priority to harmonize the test severity for all mass classes. This introduction will allow switching towards a homogeneous fleet that seriously reduces aggressivity and severity rate issues.

Three approaches were proposed with different added value. These are, from the lowest to the highest potential for a desired homogeneous test severity:

- remove the deformable element and fix the test speed to the desired test severity,
- adapt the test speed to the kerb weight of the vehicle taking into account the energy absorbed by the current barrier,
- change the deformable element and fix the test speed according to the desired severity.

These three propositions answer the problem of force matching and global aggressivity, however, only the last one is able to fix the structural interaction, problem, also raised as a priority.

REFERENCES

[1] Heavy vehicle and Assessment Protocol , Euro NCAP 2012.

[2] NHTSA: Evaluation of the Enhancing Vehicle-to-Vehicle Crash Compatibility Agreement: Effectiveness of the Primary and Secondary Energy-Absorbing Structures on Pickup Trucks and SUVs – may 2012

[3] Technical assistance and economic analysis in the field of legislation pertinent to the issue of automotive safety: provision of information and services on the subject of accident analysis for the development of legislation on frontal impact protection –TRL, 2010- D Richards, M Edwards and R Cookson-

[4] Self Protection and partner protection for new vehicles (UNECE R94 amendment) - Cyril Chauvel-ESV Washington 2010 - Paper number 11.0209

[5] Results of NHTSA's Comparison of the Offset Deformable Barrier and the Progressive Deformable Barrier Test Procedures ESV 2009, J. Saunders paper 09-0549

[6] Informal document No. GRSP-41-25, 41st GRSP, 7-11 May 2007, ECE/TRANS/WP.29/GRSP/2007/17 –

[7] EEVC WG 15 Final Report to EEVC Steering Committee, May 2007,

[8] PDB Barrier face evaluation by DSCR and NHTSA'S joint research program, Pascal Delannoy, 20th ESV Conference 2007, Paper No. 07-0303

[9] Australian Research To Support The Ihra Vehicle Compatibility Working Group, K A Seyer, C A Newland and M B Terrell, ESV 2003 Paper No: 274

[10] Compatibility assessment proposal close to real life accidents P.Delannoy, ESV Nagoya 2003, paper number 94

[11] Design Considerations for a Compatibility Test Procedure, Stephen Summers, William T. Hollowell, Aloke Prasad, Society of Automotive Engineers Paper No. 2002-02B-169. March 2002,

Occupant Behavior in Small Front Overlap Event – A Parametric Study

Kapil Butala
David Gotwals
Ravi Tangirala
Kurt Shanks
Hyundai-Kia America Technical Center, United States
Paper 13-0135

ABSTRACT

Frontal crash tests have always been at the forefront of vehicle safety evaluation. However, the full frontal testing and 40% oblique testing that is included in the National Highway Traffic Safety Administration (NHTSA) and the Insurance Institute for Highway Safety (IIHS) rating system does not represent some of the severe crashes recorded in the field. NHTSA and IIHS have been investigating frontal oblique impacts with narrow, offset objects to increase the coverage of replicating real world crashes with controlled testing procedures.

The objective of this paper is to study and understand the effect of vehicle structural performance on the occupant kinematics and related injury during small front overlap crashes. As occupant kinematics and injuries are directly influenced by structural response of the vehicle, this paper focuses on effect of various structural responses with corresponding intrusions and rotations. It also investigates effectiveness of the restraint system to reduce the occupant injuries.

MADYMO software was used to create a small front overlap environment. A driver occupant was represented by 50th percentile Hybrid III dummy model. All the intruding parts (floor, dash, hinge pillar, IP, steering column, A-pillar, door, door trim) were represented by planes and hyper-ellipsoids. Time based intrusions were extracted from the small front overlap test data and applied to all intruding parts. Seat belt system, driver airbag, side airbag and curtain airbag were modeled as part of restraint system. Longitudinal (X) and lateral (Y) structural responses were applied to the MADYMO dummy. A parametric study was then designed to understand the effect of various vehicle structural responses, restraint system deployment timing, seat belt load limiters and steering wheel lateral and vertical movements on occupant kinematics and injuries.

INTRODUCTION

In designing a small overlap test condition, the IIHS researched over 20 years of crash scene data. In 2009, Sherwood et al [1], stated that one-quarter of severe crashes had loading on less than 40% of the vehicle's front end structure. The test procedure consists of impacting a 6 inch diameter rounded barrier at 64 km/h with a 25% overlap of the front width of the vehicle. There are three categories for the rating evaluation; (1) restraints and dummy kinematics, (2) dummy injury measures, (3) and vehicle structural performance. The restraints and dummy kinematic assessment allows for further evaluation besides injury measurements from the test dummy, and can be applied to occupants of other sizes and seating positions. This category uses a demerit system for Frontal Head Protection, Lateral Head Protection, Frontal and Lateral Chest Protection, and Occupant Containment. Four groups of dummy injury ratings utilize the instrumentation in the dummy's (1) head and neck, (2) chest, (3) hip and thigh, and (4) legs and feet. Each of these body regions receives one of the ratings, Good, Acceptable, Marginal, or Poor, based on the performance. The lowest score of the four regions is used as the overall dummy injury rating. The vehicle structural rating is based upon the pre-test and post-test measurements of seven various locations. It is further divided into upper and lower occupant compartment regions. The upper region includes measurements of the steering column, upper hinge pillar, upper dash, and left instrument panel (knee bolster). The lower region includes lower hinge pillar, footrest, left toe-pan, brake pedal, parking pedal, and rocker panel. Each region receives a sub-rating, and the overall structural rating is based upon the worst performing region.

METHOD

Model

In this paper, correlation refers to the kinematic and injury comparison between CAE model and test data. Baseline vehicle refers to the in-house test that was conducted on one of the vehicles.

The data in this paper was gathered using a MADYMO small overlap simulation model (Figure 1). A correlated NCAP model was used to develop a small front overlap baseline model. Hybrid III 50th percentile dummy was used as a driver occupant. This model used driver airbag, retractor pretensioner and anchor pretensioner as a part of restraint system. A generic finite element model of curtain airbag was included. Multi-Body (MB) surface planes were created for the upper and lower interior door trim, along with the armrest. A-pillar segments and the side rail were represented by cylinders. Hinge pillar and dash were modeled using planes. Each surface was given a translational joint in the primary direction of relevant movement; dash, a-pillar, and side rail in the X direction, and hinge pillar and door trim in the Y direction. The steering column joint was given Y rotation capabilities to replicate the vehicle test.

Structural intrusion data was extracted from a full vehicle test and from an LS-DYNA structural simulation model. The intrusions of surfaces were derived from pre and post test measurements, along with a dynamic estimation based on the LS-DYNA model and baseline comparison injury results.

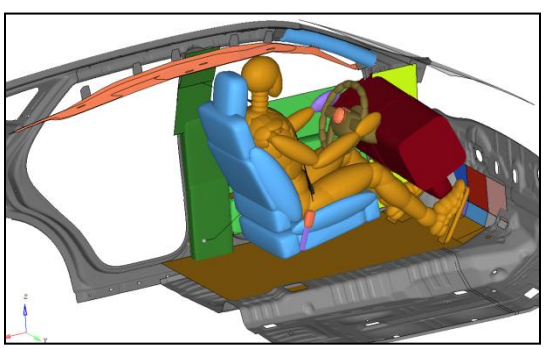

Figure 1. Baseline Small Overlap Model

Parameter Study

The parameter study of adjustable component characteristics and performance assessment was used to understand the resulting effects on the kinematics of the dummy. IIHS has shared the structural responses from the small overlap tests performed in the last year. Vehicles were selected from all performance categories of the IIHS rating system. The vehicles' structural responses were analyzed and used in the model for any notable contributions of peak, duration, timing, and trends based on the accelerometer data. Restraint system deployment timing, seat belt load limiters and steering wheel lateral and vertical movements were varied to understand their effect on occupant kinematics and injuries.

RESULTS

The baseline model used for this study demonstrated good correlation with NCAP test. For small front overlap test condition, occupant kinematics showed good correlation with the small front overlap test. Due to generic curtain airbag used in the model, injury correlation was not performed. Injury correlation showed some trends and peak as per the test though. This correlation is displayed in Figure 2, with the test vehicle data displayed in blue, and the simulation data in red.

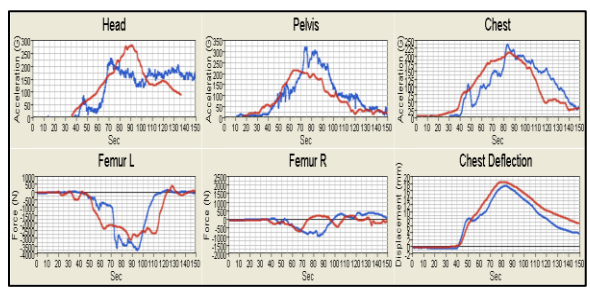

Figure 2. Baseline Correlation

With this correlation, focus of the study was to understand occupant kinematics, injury trends and associated demerits with variation in parameters.

Following injury reference values were used to compare injury percentage in the paper.

HIC: 700
Chest Acceleration: 60 G
Chest Deflection: 50 mm
Femur Force: 10,000 N

Parametric study:

1) Vehicle structural response

In-house full vehicle small front overlap test showed that the upper body injury values were

low and had more than 50% margin for a Good rating. Lower body injury values were high due to excessive structural intrusion. For Good or Acceptable structural performance for this test, structural countermeasures have to be developed.

These structural countermeasures can be divided into 2 categories.

Category 1: Deflection strategy where vehicle rotates at the point of contact and deflects away from the barrier, and

Category 2: Energy absorption and occupant cage protection strategy where vehicle rotation occurs when barrier contacts occupant cage.

For this parametric study, a wide variety of vehicle structural response data was analyzed using baseline model. Due to unavailability of the data, structural intrusions were maintained constant. This structural data was divided into 2 categories defined above. These two categories were simplified and represented by step function. Figure 3 shows vehicle X acceleration in G's versus time in seconds. Acceleration data was collected from accelerometer located at the bottom of B-pillar.

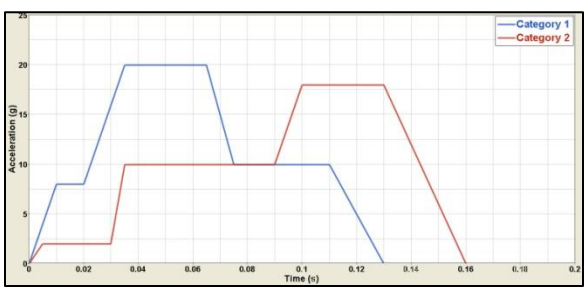

Figure 3. Simplified Acceleration versus Time Data based on Vehicle Categories

It was observed from the data that category 1 vehicles showed more rotational tendency about Z axis. This rotational tendency of the vehicle resulted into more lateral motion of the occupant.

Figure 4 compares injuries for these 2 categories. HIC value and chest acceleration were higher for category 1 vehicles. Chest deflection was very similar for both the categories.

Early loading of the vehicle for category 1 initiated early occupant motion. Occupant had more energy to dissipate. This excessive energy resulted in higher upper body injuries. Note that, lower body injuries are not compared here due to constant intrusion values. Category 2 vehicles experience higher structural intrusions and higher lower body injuries.

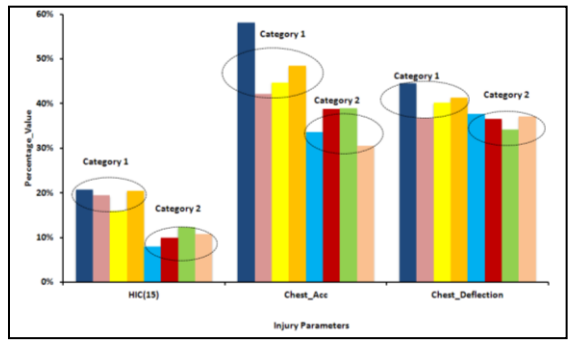

Figure 4. Occupant Injury based on Structural Response

Vehicles with category 1 structural response experienced higher lateral motion for the occupant. Based on the lateral motion, occupant showed partial or no driver airbag interaction (figure 5). This led to 1 or 2 demerits respectively.

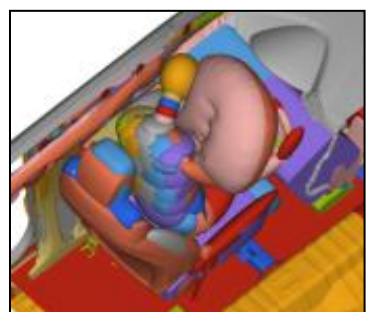

Figure 5. Partial Driver Airbag Interaction

2) Time-to-fire (ttf)

For the baseline model, time-to-fire for retractor pretensioner, driver airbag and curtain airbag was 34 ms. This time was based on in-house small front overlap test conducted.

The purpose of this parameter study was to understand the effectiveness of the restraint system based on its time-to-fire. To achieve this, restraint system ttf was varied starting from 15 ms till 65 ms at every 10 ms step (ttf: 15, 25, 34, 45, 55, 65 ms).

Figure 6 compares HIC, chest acceleration, chest deflection, head and chest displacement for various ttf.

Time-to-fire variation analysis showed that due to nature of the event, occupant did not have much energy to dissipate during first 30 ms. Deploying restraint system during this time period (15 and 25 ms) ended up driver interacting with deflating driver airbag. Driver head slid over the airbag with partial contact (demerit) and went closer to the A-pillar. Higher head and chest X travel demonstrated this motion.

Restraint system deployment at 34 proved to be the most efficient deployment. Due to structural response, occupant experienced energy transfer at 30 ms and started gaining momentum. Part of the occupant energy was dissipated immediately through fired retractor pretensioner and anchor pretensioner. Driver started interacting with driver airbag when it was in position and inflating. Most of the driver energy was dissipated through driver and curtain airbag. HIC and chest acceleration showed lower values. Head and chest displacements were minimum.

When restraint system was deployed at 45, 55 and 65 ms, driver already had gained the momentum from vehicle structural response. Delayed restraints did not help to dissipate energy efficiently. HIC value, chest acceleration, head displacement and chest displacement showed increasing trend with delay in time-to-fire.

Driver head moved into the gap between driver and curtain airbag (demerit). It went very close to the A-pillar.

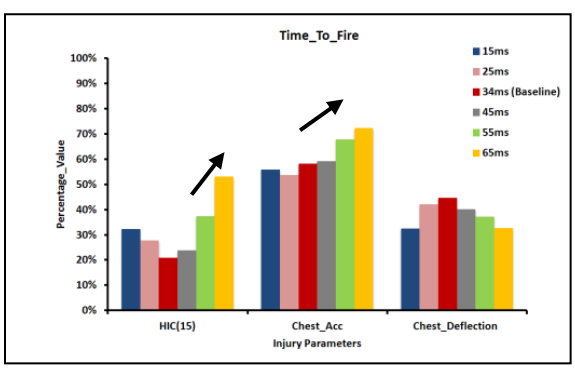

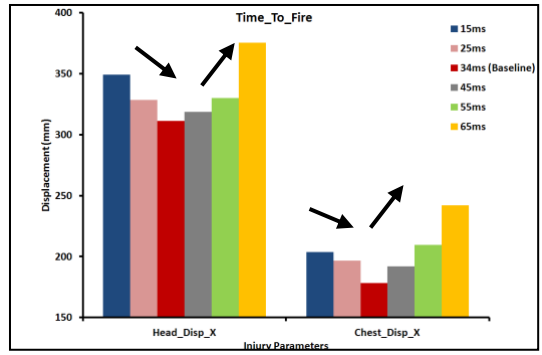

Figure 6. Occupant Injury based on Time-to-fire

3) Seat Belt Load Limiter

Seat belt load limiter plays a vital role in dictating dummy chest deflection which in turn dictates vehicle USNCAP front star rating. With the stringent criteria to achieve 5 star rating, it is observed that many vehicles use lower load limiter values.

For small front overlap, it is required to hold the dummy in place to avoid dummy excursion and dummy hard contact with occupant compartment. This requires higher load limiter.

The purpose of this parameter study is to understand effect of various levels of load limiters on dummy injury and dummy excursion.

The baseline model used a load limiter with 4 kN force. For the study, the load limiter level was varied by increments of 500 N from1.5 kN to 5.0 kN.

Figure 7 compares head and chest injury and its relative displacement due to variation of load limiter values.

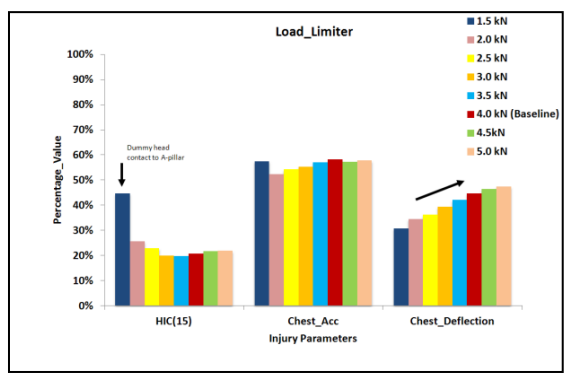

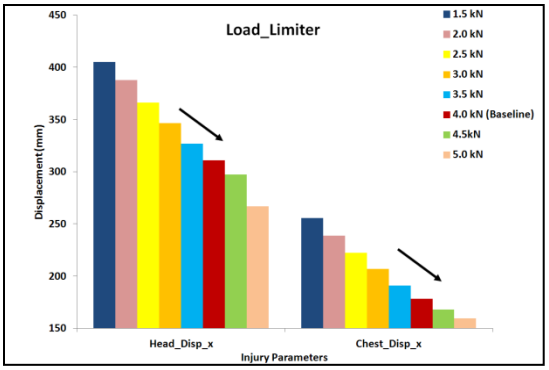

Figure 7. Occupant Injury based on Seat Belt Load Limiter Level

From the injury analysis, it was observed that with decrease in load limiter level, chest deflection was decreased significantly. It was seen at the lowest level for 1.5 kN load limiter and at the highest level for 5.0 kN load limiter.

Head and chest travel was increased with decrease in load limiter level. Since belt force was reduced, it allowed dummy head and chest to travel farther increasing the risk of dummy hard contact to occupant compartment. A head strike to the A-pillar was observed for 1.5 kN load limiter (demerit).

4. Steering Wheel Movement

IIHS rating includes a demerit qualifier for excessive vertical (>100 mm) and lateral (>150 mm) steering wheel movement. If steering wheel moves away from the occupant before occupant loads on the driver airbag, it fails to provide sufficient dummy coverage to dissipate energy through driver airbag. It may lead to higher injury values and a demerit.

This parametric study looked into 3 aspects of steering wheel:

a. Steering wheel lateral motion
b. Steering wheel vertical motion
c. Steering wheel lateral motion timing

a. Steering wheel lateral motion:

In the baseline model, steering wheel moved laterally by 55 mm. A study was conducted with 80 mm, 110 mm, 180 mm and 220 mm of lateral movement to understand its effect on dummy injury numbers. Figure 8 compares head and chest injury and its relative displacement due to variation of steering wheel lateral movement.

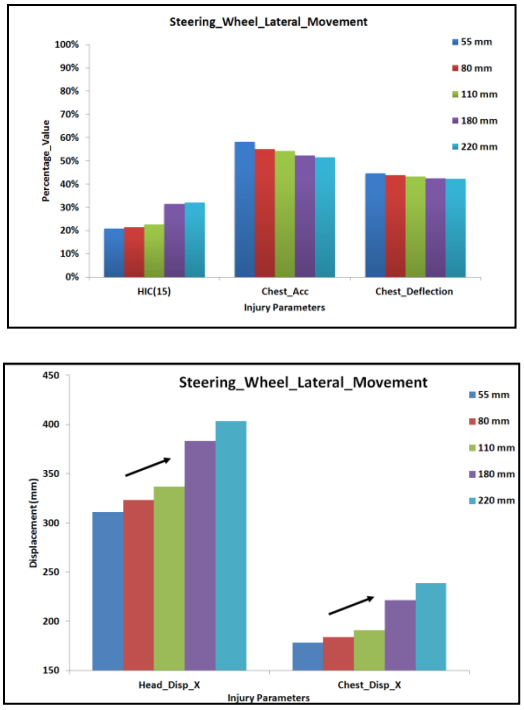

Figure 8. Occupant Injury based on Steering Wheel Lateral Movement

With the increase in steering wheel lateral movement, driver airbag coverage was significantly decreased (demerit). Lack of coverage led to increase in head and chest displacements. Lateral movements more than 150 mm affected dummy head acceleration considerably.

b. Steering wheel vertical motion:

Steering wheel vertical motion study was conducted with 55 mm, 100 mm and 150 mm vertical motion (55 mm being baseline). Figure 9 below compares head and chest injury and its relative displacements due to variation of steering wheel vertical movement.

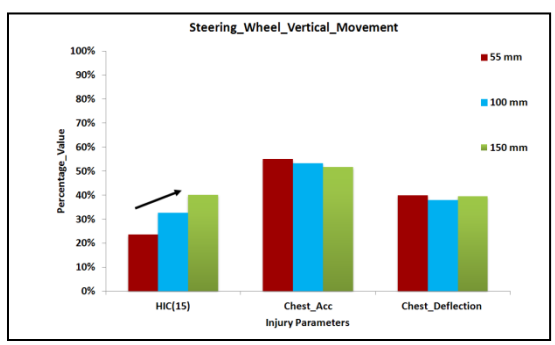

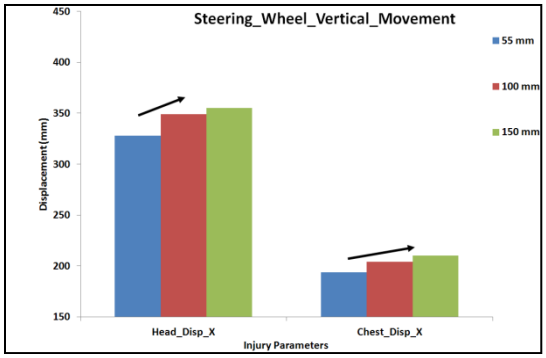

Figure 9. Occupant Injury based on Steering Wheel Vertical Movement

Driver head injury was mainly affected by steering wheel vertical movement. There was head strike to the steering wheel for 100 mm and 150 mm movement (demerit). Chest injury did not show significant change with the variation in steering wheel vertical movement.

c. Steering wheel lateral motion timing:

In the baseline model, steering wheel moved at 60 ms. In this study, steering wheel motion timing was delayed to 110 ms to understand its effect on occupant injury.

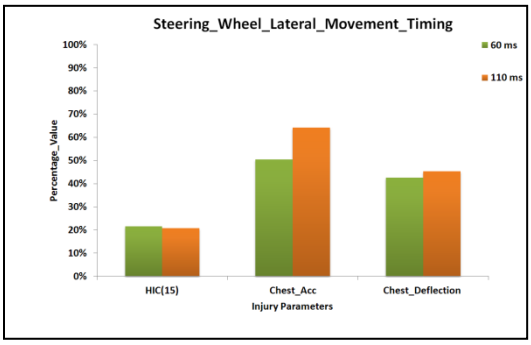

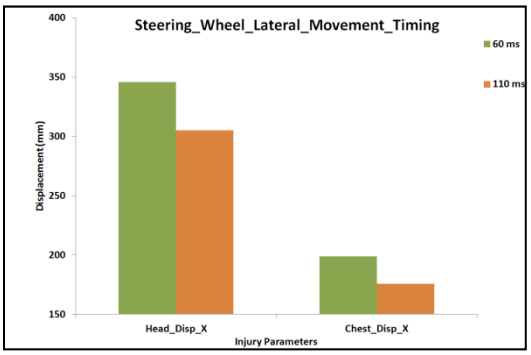

Figure 10. Occupant Injury based on Steering Wheel Lateral Movement Timing

Figure 10 compares the injury differences for steering wheel lateral movement timing. When steering wheel was moved at 110 ms, it supported dummy head and chest for longer time. This was demonstrated in reduced dummy head and chest displacements.

DISCUSSION AND CONCLUSION

- For vehicle structural response, vehicle deflection strategy leads to higher lateral and longitudinal dummy accelerations. Energy absorption and occupant cage protection strategy leads to higher structural intrusions in occupant cage. A well balanced vehicle structure and restraint system needs to be developed in order to mitigate impact energy efficiently

- Sensing strategy should complement to the structural and occupant performance

- With introduction of IIHS small overlap event, same seat belt load limiter has to comply with various impact event requirements. The strategy that is used to achieve highest STAR rating in frontal USNCAP event should be revisited and modified to comply with small front overlap event requirements

- IIHS rating includes a modifier for post test static position of steering wheel in lateral and vertical direction. If lateral or vertical motion occurs later in the event, it is not direct contributor to occupant injury. Efforts have to be taken to measure time history motion of steering wheel. A modifier has to be linked with time history data and video analysis

References

[1] Sherwood, C.; Nolan, J.; Zuby, D. 2009 Characteristics of Small Overlap Crashes, *The proceedings from the 21st International Technical Conference on the Enhanced Safety Of Vehicles (ESV)*

[2] Scullion P; Morgan R; Mohan P; Kan C; Shanks K; Jin W; Tangirala R. 2010A Reexamination of the Small Overlap Frontal Crash

[3] IIHS: Small Overlap Frontal Crashworthiness Evaluation Rating Protocol

[4] MADYMO Reference Manual Release 7.1

ADVANCED FE MODELING OF VEHICLE INTERIOR STRUCTURES TO ENHANCE THE PREDICTION FOR CRASH INDUCED INJURY RISK OF THE OCCUPANT

Dae-Young Kim
Youngwan Kim
Ngoc-Trung Nguyen
Heon Young Kim
Kangwon National University, Department of Mechanical and Biomedical Engineering
Korea, Republic of
Hyung Yun Choi
Hongik University, Department of Mechanical System Design Engineering
Korea, Republic of
Paper Number 13-0237

ABSTRACT

Vehicle occupant's contact with the interior structure is the second collision at a crash event following the vehicle collision to foreign objects. Vehicle interior structure such as door trim, arm rest, instrumental panel, knee bolster, pillar trim, roof trim, and seat pad are made of various kinds of plastics and foams. The deformation and failure of these materials largely affect the kinematics and injury risks of the occupant. The major effort on virtual simulations of car crashworthiness has been focused on the precise modeling of load carrying primary metallic structures and crash dummies until now. The objective of this study is to advance the numerical modeling scheme of vehicle interior materials for their mechanical behaviors to simulate more realistic response of dummy kinematics and its associated injury risks. Plastic materials exhibit softening, dilatational, pressure dependent and anisotropic characteristics which should be considered during the modeling process as vehicle interior parts. In this paper, pros and cons of various material types in a crash code were comparatively analyzed. Both conventional modeling method for the steel material and Phenomenological model in LS-DYNA were respectively used to simulate plastic materials. Few coupon tests were conducted to identify basic material data for the Phenomenological model. Seating occupant is basically supported by the car seat and their interactions during the crash event affect the kinematics of occupant.
The dynamic force-indentation characteristics of low density urethane foam at seat cushion and back are newly analyzed by measuring the exhalant airflow at impact test of pre-strained seat foams with trimming cover. A constitutive equation taking this airflow through the trimming into account is under development and to be built in the existing material library of crash code.

INTRODUCTION

The interior parts of vehicles are constructed of plastic and foam materials, due to their lightweight structure, ease of formability, and cost effectiveness in terms of manufacturing costs and fuel efficiency. However, these materials make it increasingly difficult to satisfy the crash performance and strength standards required by the enhanced safety regulations. Plastics are classified as crystalline or amorphous structures, according to the arrangement of cross-links that connect their molecular structure. Most vehicle interior parts consist of a combination of these two types of plastics, referred to as semi-crystalline plastics. The behavior of plastics can be described in terms of their softening characteristics, strength, and extension, as shown in (Figure 1).[1~3)]

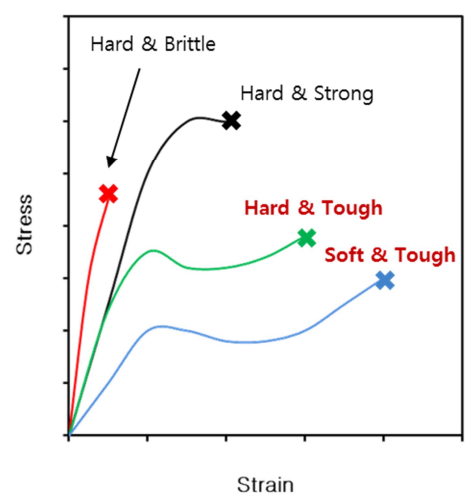

Figure 1. Classification of stress-strain curve of plastics

Constructing a material model for plastics, in terms of their structural analysis, is difficult due to their pressure dependency, dilatation, softening, and anisotropic properties. A von-Mises yield function and an isotropic hardening model have been used most often to represent the behavior of plastics in finite element analysis; however, this approach is not suitable for large deformation problems.[4~6] So, the advanced or enhanced material model for plastics is needed and the test/calibration/correlation process are needed to improve the reliability.

In this paper, several material models, that are able to apply the plastic materials, are compared and analized. Also, SAMP-1 (Semi Analytical Model for Plastics) model is described in detail.[7~9] Material test process and correlation process to obtain the parameter or data for SAMP-1 model are described. Finally, the SAMP-1 model is applied to FMH (free motion head-foam) impact analysis using the correlated parameters and data. Then the analysis results are compared with the analysis result of general material model.

In order to characterize the compression behavior (e.g., force-deformation relationship) of occupied (i.e., pre-strained) and trimmed (i.e., covered) low density PU foam in seat cushion and back, a dynamic compression machine using electromagnetic force is designed and built in this study. The design of the device enables to control the loading level and the amount of pre-strain of foam block. It is also feasible to measure exhalant air flow which significantly affects the reaction force at compression of PU foam, an highly porous material. The design of this electromagnetic machine and preliminary test result are introduced in this paper.

MATERIAL MODELS

The deformation behavior of plastics can be explained by the molecular chain state. Yield appears after undergoing nonlinear elastic behavior, in which the molecular chains become unbound by application of an external force. After the occurrence of yield, softening, hardening, and rupture behaviors appear. LS-DYNA®, commercial FE code, provides several potential material models for plastics; these models are compared in (Table 1).

Although the Piecewise_Linear_Plasticity model (MAT24), generally applied to plastics, provides strain rates and fracture expressions, it cannot reflect the general characteristics of plastics.[10] The Plasticity_with_damage model (MAT82) applies the von-Mises yield function and isotropic hardening model, similar to the Piecewise_Linear_Plasticity model, in addition to the Wilkins fracture model by considering triaxial and asymmetric stress. The Polymer model (MAT168) is a physical model based on the mechanical behavior of the molecular structure.[11] It has the advantage of being able to simulate both the elastic and plastic behaviors of plastics. However, this model does not consider strain rates, dilatation, or fracture characteristics, and requires an data of microscopic physical phenomena. The SAMP-1 model (MAT187) is based on a phenomenological model, and is much easier to apply than the Polymer model; it also has the advantage of being able to consider most characteristics of plastics.

Table 1.
Comparison of material models for plastics in LS-DYNA®

Material model	24	82	89	101	106	112	141	168	187
Pressure dependent	N	N	N	Y	N	N	N	Y	Y
Volumetric response	N	N	N	N	N	N	N	N	Y
Failure	Y	Y	Y	Y	N	N	N	N	Y
Strain rate dependent	Y	Y	Y	Y	Y	Y	Y	N	Y
Temp. dependent	N	N	N	N	Y	N	N	Y	N
Softening	N	Y	N	N	N	N	N	Y	Y

The SAMP-1 model applies a yield model based on an isotropic C-1 smooth yield surface, expressed using a non-associated plastic flow rule. (Equation 1) shows the yield function, (Equation 2) describes the plastic potential, and (Equation 3) represents the relationship between the plastic Poisson's ratio, ν_p, and the proportionality constant, α. Because changes in the plastic Poisson's ratio affect the yield function, the SAMP-1 model can also consider characteristics of a plastic in terms of changes in its volume.

$$f = \sigma_{vm}^2 - A_0 - A_1 P - A_2 P - A_3 P^2 \le 0 \qquad (1).$$

$$g = \sigma_{vm}^2 - \alpha P^2 \qquad (2).$$

$$\nu_p = \frac{9-2\alpha}{18+2\alpha} \Rightarrow \alpha = \frac{9(1-2\nu_p)}{2(1+\nu_p)} \qquad (3).$$

Where σ_{vm} gives the von-Mises stress, P is the pressure, and A_0, A_1, and A_2 correspond to the material constants. The material constants of the yield function, obtained from stress tests, are presented in (Equation 4) :

$$A_0 = 3\sigma_s^2; \quad A_1 = 9\sigma_s^2\left(\frac{\sigma_c - \sigma_t}{\sigma_c \sigma_t}\right); \quad A_2 = 9\left(\frac{\sigma_c \sigma_t - 3\sigma_s^2}{\sigma_c \sigma_t}\right) \qquad (4).$$

where σ_t is the uniaxial tensile stress, σ_c is the uniaxial compression stress, and σ_s is the shear stress. A simple damage model is used to express the softening characteristic:

$$D(\varepsilon_p) = 1 - \frac{E_d(\varepsilon_p)}{E} \quad (5).$$

where D is the function for plastic strain, E is the elasticity coefficient, and E_d is the elasticity coefficient when a load is reapplied after removal of the previous load.

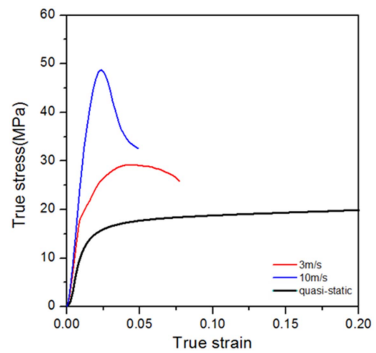

(a) Dynamic tension test

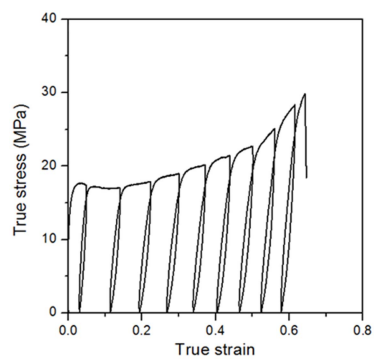

(b) Loading-Unloading test

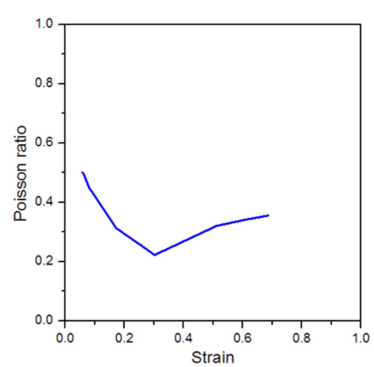

(c) Measurement of Poisson's ratio

Figure 2. Results of material tests

MATERIAL TESTS

Plastics

Uniaxial tensile, shear, uniaxial compression, and biaxial tensile tests are required to apply the yield function of the SAMP-1 model. It is also necessary to measure changes in Poisson's ratio under uniaxial tensile conditions to evaluate the plastic characteristics as a function of volume change. Additionally, loading–unloading and dynamic tensile tests are required to study changes in the elasticity coefficients and strain-rate characteristics, respectively.

In this study, several tests were performed on PP-EPDM (polypropylene/ethylene-propylene-diene-monomer) materials. Specimens with a thickness of 3.2 mm were molded for the material tests. The uniaxial tensile tests made use of ASTM D 638 Type 1 specimens and an Instron 5882 univeral testing machine (UTM).[12] A cyclic loading tester, constructed specifically for this study, was used to test ASTM E 8 specimens for the uniaxial compression and loading–unloading tests.[13] The dynamic tensile tests were performed on ASTM D 638 Type 4 specimens at speeds of 3 and 10 ms^{-1}. To measure Poisson's ratio, 2 mm × 2 mm square lattices were printed on the surface of the specimens for the uniaxial tensile tests, and the displacement was traced by capturing the deformation conditions in each strain section. Based on the traced displacement, the strain ratio along the longitudinal and transverse directions was calculated to verify the data for Poisson's ratio. The test results are presented in (Figure 2).

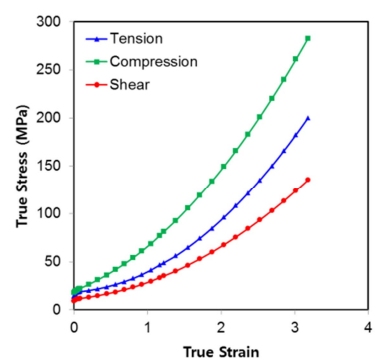

Figure 3. Plastic stress-strain curves

Seat foam

Mostly due to the difficulties of controling the amount of prestrain of foam block with the conventional drop weight type impact machine, a dynamic compression machine with utilizing electromagnetic force is substitutingly designed and built as shown in (Figure 4). Loading part of the device consists of two adjoined electromagnets and control unit. When control

unit is triggered to supply an electric current, both electromagnets are magnetized with same polarity and sudden repulsive force will be produced. Upper electromagnet is fixed at the frame of the barrel which has square cross section (100x100mm) but the lower electromagnet freely moves downward along the barrel and strikes the foam block. The peak striking force is modulated by the voltage level upto 100V and the prestrain of foam block can be easily adusted by positioning the initial electromagnets along the barrel upto 40% prestrain. The bottom plate supporting the foam block has 25 vent holes (5X5 with Φ6mm, D3574-08 ASTM[14]) through which the exhalant air can be gauged by flux sensors (ASF1430 Bidirectional Mass Flow, SENSIRION). Seat cover may be placed between foam block and perforated bottom plate to quantify the effect of air flow on the reaction force. Reaction force is measured by a loadcell (1kN, Testometric) positioned at the bottom of the supporting structure, i.e., barrel and perforated bottom plate.

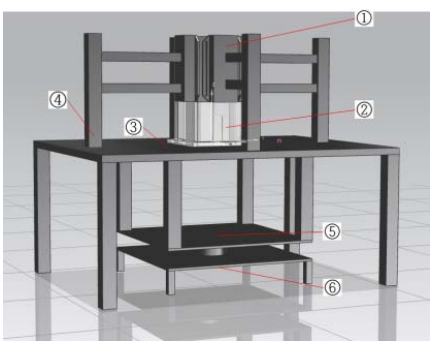

Figure 4. Dynamic compression device using electromagnets 1 Electromagnets, 2. Foam block, 3 Perforated bottom plate 4 Frame, 5 Upper load cell plate 6 Lower load cell plate

The preliminary test result is shown in (Figures 5-7). A foam block (Density: 48kg/m3, size: 100X100X100) and trimming pad cover for small sedan vehicle are employed. The reaction force profile measured at the load cell shows an initial sharp peak followed by a plateau and they both increase linearly with applied electric voltage level to the electromagnets (See Figure 5). The prestrain decrease the reaction force as shown in (Figure 6) but this possibly associates a misleading since the presented reaction force does not include initial preload developed by the given prestrain. As expected, the trimming pad placed between foam block and perforated bottom plate restricted exhalant air flow as shown in (Figure 7).

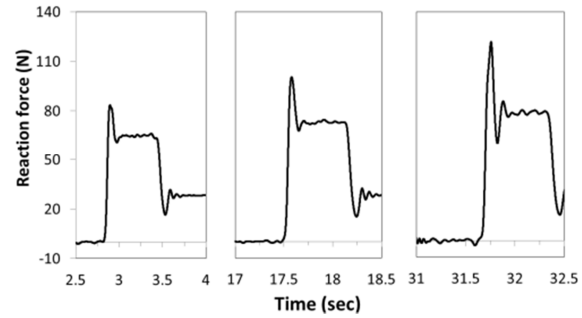

Figure 5. Reaction force profiles with electric voltage applied to the electromagnets, With no prestrain and trimming pad, left: 60V, middle: 80V, right: 100V

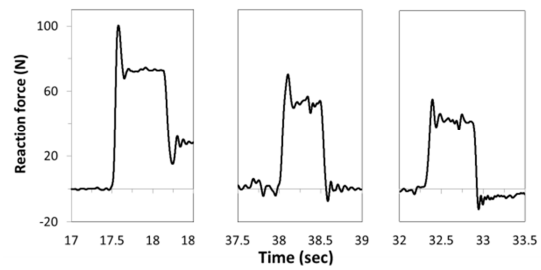

Figure 6. Reaction force profiles with prestrain, applied voltage to the electromagnets: 80V, left: 0% prestrain, middle: 20% prestrain, right: 40% prestrain.

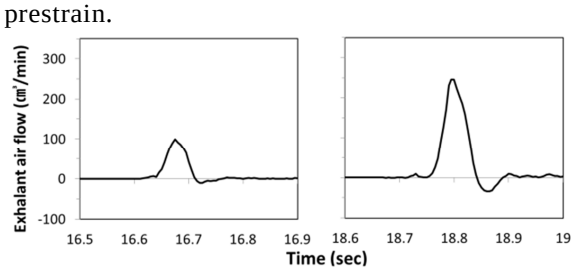

Figure 7. Reaction force profiles with and without trimming pad, applied voltage to the electromagnets: 50V, left: with pad, right: without pad

CALIBRATION AND VERIFICATION

The various parameters from the material tests were calculated and supplied to the SAMP-1 model. The plastic regions after a yield point were also defined based on the results of the uniaxial tension and compression tests. The relationship between the shear stress and shear strain was determined based on the Drucker–Prager theory that defines the relationship between uniaxial tension, uniaxial compression, and shear stress:

$$\sigma_s = \frac{2\sigma_t \sigma_c}{\sqrt{3}(\sigma_t + \sigma_c)} \qquad (6).$$

The stress–strain diagram of the uniaxial tension, uniaxial compression, and shear in the plastic region is presented in (Figure 3). However, it was necessary to transform the stresses because their scales varied according to changes in the observed damage and Poisson's ratio.
FE analysis of a unit shell element model and ASTM D 638 tests for Type 1 specimens were used to verify the material model. As shown in (Table 2), an analysis was performed to determine the differences between a conventional material model and the SAMP-1 model.

Table 2.
Analysis cases to compare the conventional model and SAMP-1 model

Case	Model	Mode	Material model	S-S curve	Plastic Poisson's ratio	Damage
Case 1	Unit shell element	Tension Compression Shear	Piecewise Linear Plasticity	Tension	0.5	N
Case 2	Unit shell element	Tension Compression Shear	SAMP-1	Tension	0.5	N
Case 3	Unit shell element	Tension Compression Shear	SAMP-1	Tension Compression Shear	0.5	N
Case 4	Specimen	Tension	Piecewise Linear Plasticity	Tension	0.5	N
Case 5	Specimen	Tension	SAMP-1	Tension Compression Shear	Curve	Curve

For cases 1, 2, and 3, the differences with respect to the yield functions of the Piecewise_Linear_Plasticity and SAMP-1 models were determined using the unit shell element model. The results are presented in (Figure 4). There was good agreement between the SAMP-1 model and the test results for uniaxial tension, uniaxial compression, and shear conditions. However, the Piecewise_Linear_Plasticity model results differed, indicating a constant yield stress for various pressures. Cases 4 and 5 compared the Piecewise_Linear_Plasticity and SAMP-1 models using ASTM D 638 Type 1 specimens. SAMP-1 was defined with respect to the observed damage and Poisson's ratio. The results of these cases are presented in (Figure 8) and (Figure 9). The Piecewise_Linear_Plasticity model indicated large localized deformations, while the SAMP-1 model was in good agreement with the test results. The SAMP-1 model showed transverse changes in the surrounding elements after necking, similar to the tests, because dilatation was considered in this model.

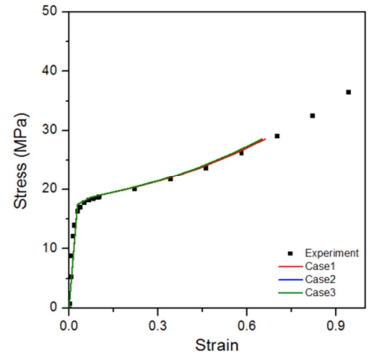

(a) Tension mode

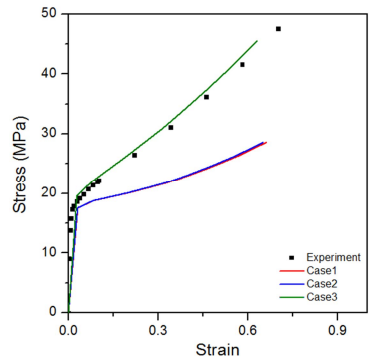

(b) Compression mode

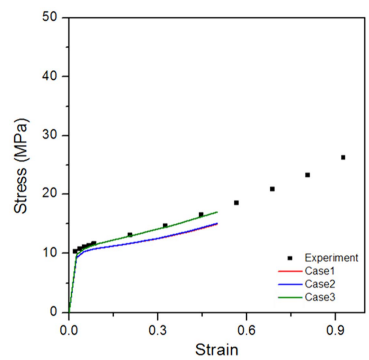

(c) Shear mode

Figure 8. Analysis results using unit shell model

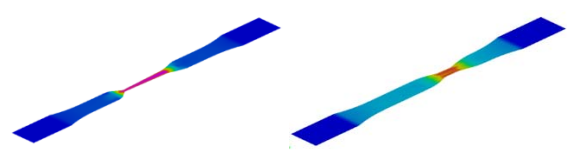
(a) MAT24 (b) MAT187

Figure 9. Comparison of deformed shapes

APPLICATION

To apply the SAMP-1 model to the interior materials in vehicles, an impact analysis for the pillar inner trim was performed based on FMVSS201U for the impact of interior materials established by the

National Highway Traffic Safety Administration (NHTSA).[15] FMVSS201U regulates the value of the head injury criterion (HIC). HIC(d), the equivalent value of the head injury criterion, did not exceed 1000 free-motion head (FMH) strikes against 16 impact points on the upper interior parts of the vehicle for a vehicle traveling at a speed of 15 mph. The FMH model, provided by Livermore Software Technology Corporation (LSTC), was used for the impact analysis and to determine the boundary conditions required to introduce bending and collapse deformations, as shown in Figure 11. The strain rates obtained from the PIECEWISE_LINEAR_PLASTICITY and SAMP-1 models were compared. Also, the true stress–true strain curve, measured from the dynamic tensile tests, was fitted using the G'Sell–Jonas model presented in (Equation 7).[16] The G'Sell–Jonas model includes the material behavior characteristics of viscoelasticity, viscoplasticity, and temperature,

$$\sigma(\dot{\varepsilon}, \varepsilon, T) = K(\dot{\varepsilon})^m e^{h\varepsilon^2}(1-e^{-w\varepsilon})e^{\frac{a}{T}} \qquad (7).$$

where K, a, w, h, and m are the material constants, and T is the absolute temperature.

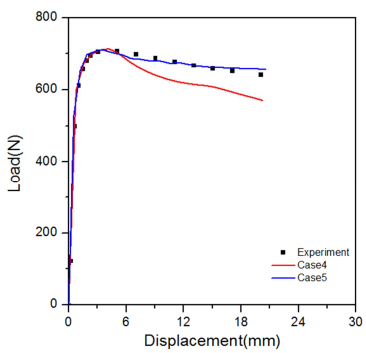

Figure 10. Comparison of L-D curve

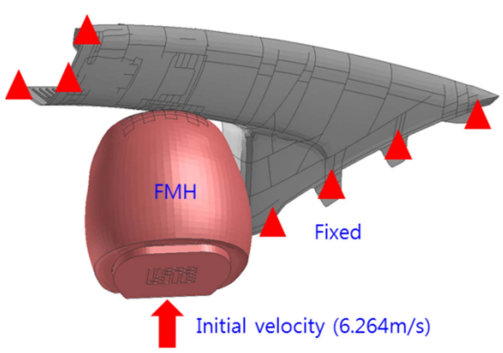

Figure 11. Boundary condition for FMH impact analysis

From the analysis results, it was possible to obtain the contact pressure and acceleration diagram, as shown in (Figure 12). HIC (d) is calculated using the acceleration diagram; the HIC value is given by (Equation 8), in which $a(t)$ is the three-axis composition acceleration of the center of mass in the FMH model, and t_1 and t_2 represent random times of presenting the maximum injury below 36 ms in the impact event. HIC(d) can be represented by (Equation 9) to determine the correlation to the head injury level in a practical impact test using a test dummy.[17~19]

$$HIC = \max\left[\left(\frac{1}{t_2 - t_1}\int_{t_1}^{t_2} a(t)dt\right)^{2.5}(t_2 - t_1)\right] \qquad (8).$$

$$HIC(d) = 166.4 + (0.75446 \times HIC) \qquad (9).$$

The results from the PIECEWISE_LINEAR_PLASTICITY model, with and without consideration of the strain rate, were 12.67 and 18.45, respectively. This varied significantly from the results provided using the SAMP-1 model, which were 11.71 and 14.97 with and without strain-rate consideration, respectively.

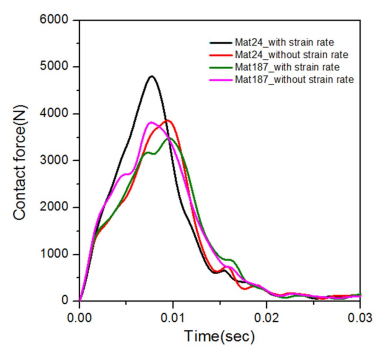

(a) contact force curves

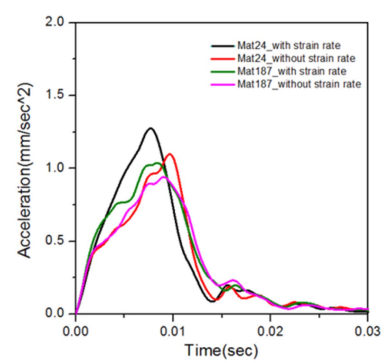

(b) Acceleration curves

Figure 12. Comparison of results for FMH impact analysis

CONCLUSION

Material models that could be applied to the LS-DYNA simulation software were compared to implement material modeling for plastic materials. Several material tests were performed using the SAMP-1 model. A method for obtaining the parameters and material data was proposed based on these tests. The proposed models were verified using a unit model and a specimen model of a shell element. Differences between the proposed material model and the conventional material model were analyzed. There was good agreement between the SAMP-1 model and the test results for material tests. The large differences in the results for each model could be explained based on whether or not a model considered the strain rates determined from FMH impact analysis for the pillar inner trim of vehicles. In order to effectively realize the prestrain of seat foam which represents an occuppied condition into the dynamic compression test, elecromagnets are introduced to substitute the conventional test device such as drop weight. From the preliminary test result even though in a limited range, the device verified its good repeatibilty and efficiency for characterizing the compression behavior of seat foam with various loading and prestrain conditions. Utilizing flux sensors, it becomes also feasible to gause the exhalant air and thus quantify the effect of trimming pad cover which interferes with the air flow. This new and additional characterization in deformation behavior of seat foam will be incorporated into crash codes as a more advanced material card.

REFERENCES

[1] Andrzej Pawlak and Andrzej Galeski. 2005. “Plastic Deformation of Crystalline Polymers.” American Chemical Society, Vol. 38, No. 23, 9688-9697

[2] A. Blaga. 1973. “Properties and Behaviour of Plastics.” NRC

[3] G’Sell, C. 1986. “Plastic deformation of glassy polymers: constitutive equations and macromolecular mechanisms.” Ocfor, 1943-1982

[4] Arild Holm Clausen, Mario Polanco-Loria, Torodd Berstad and Odd Sture Hopperstad. 2011. “A CONSTITUTIVE MODEL FOR THERMOPLASTICS WITH SOME APPLICATIONS.” 8th European LS-DYNA Users Conference

[5] M. Avalle, M. Peroni and A. Scattina. 2010. “Mechanical models of the behaviour of plastic materials: influence of time and temperature.” Latin American Journal of Solids and Structures, 41-61

[6] M.C. Boyce, S. Socrate, P.G. Llana. 2000. “Constitutive model for the finite deformation stress–strain behavior of poly (ethylene terephthalate) above the glass transition.” Polymer, Vol. 41, No. 6, March: 2183-2201

[7] LIVERMORE SOFTWARE TECHNOLOGY CORPORATION (LSTC). 2007. “LS-DYNA KEYWORD USER'S MANUAL VOLUME I”

[8] S. Kolling, A. Haufe, M. Feucht & P.A. Du Bois. 2005. “SAMP-1: A Semi-Analytical Model for the Simulation of Polymers.” LS-DYNA Anwender forum

[9] Kunio TAKEKOSHO and Kazukuni NIWA. 2012. “Validation and Material Modeling of Polymers by Employing MAT_SAMP-1.” 12th International LS-DYNA Users Conference

[10] M. Vogler, S. Kolling, A. Haufe. 2007. “A Constitutive Model for Plastics with Piecewise Linear Yield surface and Damage.” LS-DYNA Anwender forum

[11] M. Polanco-Loria1, H. Daiyan and F. Grytten. 2012. “Material parameters identification: An inverse modeling methodology applicable for thermoplastic materials.” Polymer Engineering & science, Vol. 52, No. 2, February: 438-448

[12] ASTM D638-10. 2010. “Standard Test Method for Tensile Properties of Plastics” ASTM International, Vol. 08.01

[13] ASTM E8-11. 2011. “Standard Test Method for Tension Testing of Metallic Materials.” ASTM International, Vol. 03.01

[14] ASTM D3574-08 Standard Test Methods for Flexible Cellular Materials - Slab, Bonded, and Molded Urethane Foams

[15] Hyoung Gon Kim, Shinill Kang. 2001. “Optimum Design of A-Pillar Trim for Occupant Protection.” KSAE, Vol. 9, No. 2, 99-106

[16] Marcus Schoßig, Christian Bierogel, Wolfgang Grellmann, Thomas Mecklenburg. 2008. “Mechanical behavior of glass-fiber reinforced thermoplastic materials under high strain rates.” Polymer Testing, Vol. 27, July: 893-900

[17] FMVSS 201U: Occupant Protection in Interior Impact Upper Interior Head Impact Protection. 1998. Federal Motor Vehicle Safety Standard, National Highway Traffic Safety Administration, U.S. Department of Transportation

[18] Younghan Youn, Youngki Kim, Hyeongyo Park, Heesang An. 2005. “Analytical Studies on the Pillar Trim Impact Test Using FMH.” Autumn conference of proceedings of the KSAE, 1491-1495

[19] Bharatendra Rai, Nanua Singh, Mustafa Ahmed. 2004. “Robust design of an interior hard trim to improve occupant safety in a vehicle

crash." Reliability Engineering and System Safety, Vol. 89, 296-304

THE CRASHWORTHINESS OF MINICARS IN FRONTAL IMPACT TESTS

Koji Mizuno
Nagoya University
Yuji Arai
Japan Automobile Research Institute
Naruyuki Hosokawa
National Traffic Safety and Environment Laboratory
Japan
William Hollowell
WTH Consulting LLC
United States

Paper number 13-0255

ABSTRACT

In Japan, the number of minicars is increasing due to market demands resulting from environmental and economic concerns, and constitutes 32% of the registrations among passenger cars (2012). The safety of the minicar for various crashes is a technological challenge due to its small size and mass. In this paper, the crashworthiness of minicars was investigated and the issues that should be addressed are discussed. The crash pulse, deformation, and dummy responses of minicars were examined for various frontal impact tests: full-width rigid barrier (FWRB), offset deformable barrier (ODB), full-width deformable barrier (FWDB), and car-to-car tests.

In the FWRB tests, the car accelerations were high and large crash loadings were applied to the occupants. The dummy injury measures were less than injury thresholds because of the high performance of occupant restraint systems: the early and timely restraint system. In the FWDB tests, the deformation mode was relatively comparable to that in the car-to-car tests, and dummy injury measures were higher than those in the FWRB tests. An analysis using a simple spring-mass model indicated that a later restraint trigger time in the FWDB test led to high injury measures of the occupants.

In the ODB tests, the passenger compartment was intact for all of the tested minicars. Since the car acceleration in the ODB test was lower than that in the FWRB tests, all of the injury measures of the driver dummy in the ODB tests were smaller than those in the FWRB tests except for the tibia index. In the car-to-car tests, though the minicar has a single-load path, the structural interaction was acceptable since the engine was located forward in the vehicle and interacted with structures of the other car. The passenger compartments of the minicars were intact and injury measures were lower than the injury thresholds until the loading on the vehicles reached the NCAP crash severity level. The crashworthiness of Japanese minicars could be representative of the safety of future mini electric vehicles.

INTRODUCTION

In Japan, a category of mini vehicle has been introduced as of 1949 in order to disseminate more detailed information of passenger cars to the public. Since then, the specifications of the mini vehicle were revised several times, and in 1998 the specifications stated that the engine dimension was equal or less than 0.660 l; and that the length, width, and height were equal or less than 3.4 m, 1.48 m, and 2.0 m respectively (Road Trucking Vehicle Act). According to the Automobile Inspection and Registration Information Association, the number of registered vehicles is 79,871,540 in Japan on November of 2012. Among them, the number of mini vehicles including minicars and mini trucks is 28,274,642 (35.4%). For passenger cars, the number of registered minicars and other size cars is 19,216,040 (32.4%) and 40,184,214 (68.6%), respectively. This trend of a large portion of minicar registration is anticipated to continue especially when the economic situation is taken into consideration.

The crashworthiness of the minicar has been addressed in the regulation and New Assessment Car Program (NCAP). Since 1994, a full-width rigid barrier (FWRB) test has been introduced to passenger cars in the Japanese regulation. At that time, the test velocity of the minicars was 40 km/h. In 1998, the velocity of minicars was increased to 50 km/h, and the minicar dimensions were extended to satisfy this severe impact condition. The Japan New Car Assessment Program (JNCAP) started at 1995, and the FWRB tests at 55 km/h were conducted though minicars were not included among the tested cars. The minicars have been involved in JNCAP tests as of 1999. In 2000, JNCAP started an overall more comprehensive evaluation test program. The tests consisted of the FWRB (55 km/h) tests, the offset deformable barrier (ODB) tests (64 km/h), and the side impact test (55 km/h). In 2007, the ODB tests at 56 km/h (ECE R94) were applied to passenger cars including the minicars in the Japanese regulation. At present, the same crash tests and their requirements are applied to minicars as to the other passenger cars.

National accident data (2009) show that the probability of fatal injury to occupants in minicars (0.23%) was comparable to that of other size passenger cars (0.22%) in all accidents. However, in car-to-car collisions, the injury risks to occupants are higher for minicars as compared to larger size cars. The Institute of Traffic Accident Research and Data Analysis (ITARDA) investigated the injury risk to drivers in vehicle-to-vehicle collisions classified from vehicle category and driver age [1]. The number of fatal and serious injuries to drivers of minicars constitutes 24.3% of these injuries among all vehicle types.**Error! Reference source not found.** Figure 1 shows the probability of fatal and serious injuries to drivers. They are high for minicars, particularly for elderly people.

In this research, the crashworthiness of minicars in various front impact tests was examined. The test data included in the analysis were from the FWRB and ODB tests conducted by JNCAP from 2008 to 2011, the full-width rigid barrier (FWDB) and car-to-car crash tests conducted by both the Ministry of Land, Infrastructure, Transport and Tourism (JMLIT) and the Japan Automobile Manufacturers Association (JAMA).

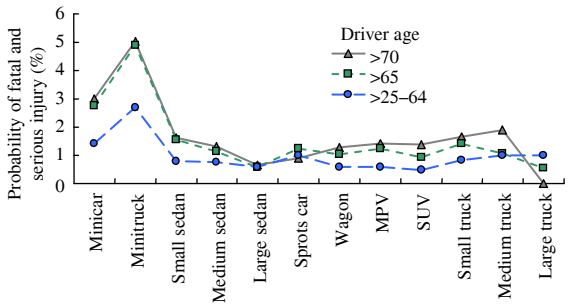

Figure 1. The probability of injuries to drivers for vehicle types in vehicle-to-vehicle collisions [1]

STRUCTURES

Though the engine compartment of the minicars is short, there are no significant differences in the structures of minicars as compared to other size cars (Figure 2). The minicar A has front rails connected by the bumper cross beam. The lower cross member of the driver side is connected with the suspension member by a tube. The minicar B does not have a bumper cross beam; however, the tall front rails of the minicar B are connected by the stiff lower cross member. The lower cross member is connected by tubes with the suspension member. In general, the engine of minicars is located forward, and the air conditioner compressor and the catalytic device (which are stiff structures) are installed in front of the engine. In car-to-car crashes, they can interact with structures of other cars.

The height of the front rail and subframe of cars are shown in Figure 3. The cross section of the front rails of the minicars are included within the Part 581 zone, but are inclined to be lower than that of cars of larger size. The lower front rails of the minicars could cause insufficient energy absorption of the front rails, and lead to underride in car-to-car crashes.

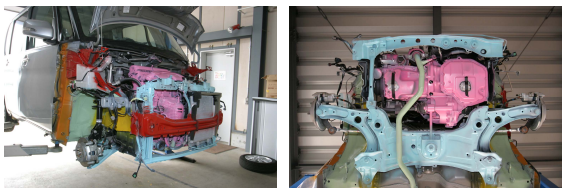

(a) Minicar A

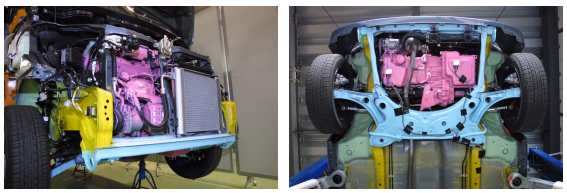

(b) Minicar B

Figure 2. The structure of minicar [2]

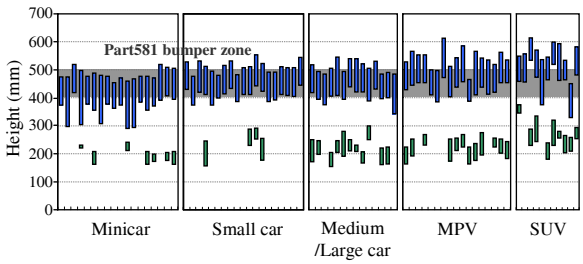

Figure 3. The ground clearance of front rails (blue bars) and subframes (green bars)

FWRB TESTS

In the FWRB tests, the acceleration of the passenger compartment is high and provides a demanding environment for the evaluation of the performance of the restraint system.

Vehicle Acceleration

The vehicle deceleration-time histories in the FWRB tests are shown in Figure 4(a). The deceleration was measured at the driver side B-pillar. There are two stages in the vehicle deceleration. The first stage is characterized by the collapse of the front rails, and the second stage is characterized by the deformation of the structures behind the engine including passenger compartment. The average deceleration of minicars over the crash pulse time duration is about 300 m/s^2 and that of other cars is 180 m/s^2. The time duration of the mini cars (60–80 ms) is shorter than that of other size cars (80–100 ms). The deceleration-displacement curves are shown in Figure 4(b). The front rail axial collapses within 0.2 m of the vehicle deformation, and the maximum minicar deformation is 0.4 m. For other size cars, the maximum deformation is distributed from 0.5 to 0.7 m. The high decelerations of the minicars indicate a high stiffness of front structures relative to their mass.

Occupant Response

The decelerations of a vehicle and driver dummy (Hybrid III AM50th) in the FWRB tests are compared for a minicar and a small sedan in **Error! Reference source not found.**. As the vehicle deceleration of the minicar is higher, the dummy chest and head decelerations in the forward direction (x) are also higher for minicars. The seatbelt pretensioner activates at 12 ms for the minicar and at 18 ms for the small sedan. In general, the time to fire (TTF) of the restraint system is 9–10 ms for minicars, whereas it is 15–18 ms for other size cars. Therefore, the early TTF is one of key parameters to consider for optimizing the occupant protection provided by minicars.

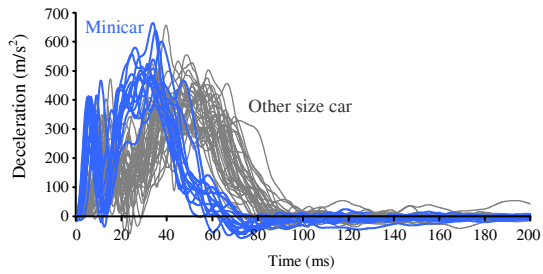

(a) Vehicle deceleration-time history

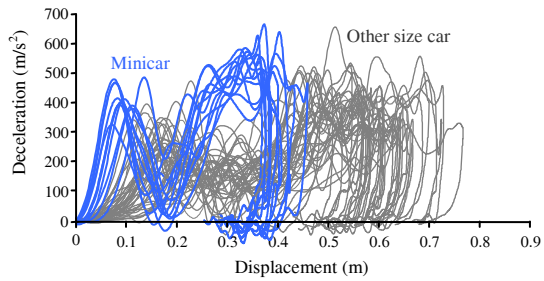

(b) Vehicle deceleration-displacement curve

Figure 4. Vehicle deceleration-time history and deceleration-displacement curve in FWRB tests at 55 km/h

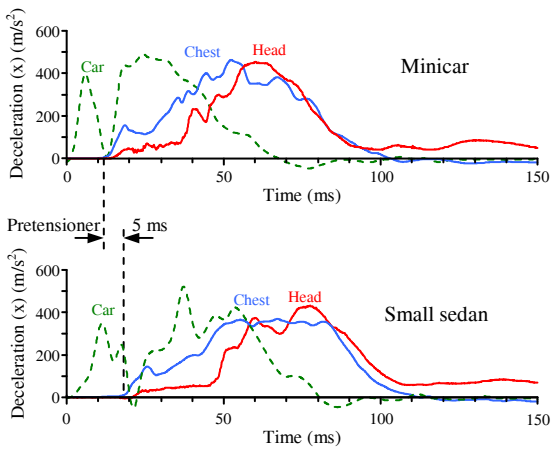

Figure 5. Vehicle and driver dummy deceleration in the forward direction vs. time for a minicar and small sedan in FWRB tests at 55 km/h

In frontal crashes, the occupant motion energy is absorbed by the restraint system energy and vehicle deformation energy. The sum of restraint system energy and ridedown energy is equal to the initial kinetic energy. When normalized by the occupant mass, this can be written as:

$$V_0^2/2 = e_{rs} + e_{rd} \quad (1)$$

where V_0 is the initial velocity, e_{rs} is the restraint energy density and e_{rd} is the ridedown energy density. The ridedown efficiency μ that indicates that the ratio of vehicle deformation energy to initial occupant motion energy, is defined as [3]:

$$\mu = \frac{\int_0^{X_{max}} (-\ddot{x})\, dX}{V_0^2/2} \quad (2)$$

where x and X is the chest displacement and the vehicle displacement, respectively. Figure 6 shows the ridedown efficiency calculated using the chest acceleration of driver dummy. The ridedown efficiency decreases with the average deceleration of the vehicle. The ridedown efficiency of minicars is distributed from 0.2 to 0.35, whereas that of other size cars is distributed from 0.3 to 0.65. Accordingly, a greater portion of the initial occupant motion energy should be absorbed by the restraint system in minicars.

Figure 7 provides a plot of the chest deceleration of the driver dummy vs. the chest displacement relative to the vehicle. Two minicar models are shown in addition to the other size cars. The area surrounded by the acceleration and displacement curve (up to the point of maximum displacement) represents the restraint energy. This area tends to be larger for minicars because the ridedown energy of the minicar is large. Both minicars shown is this plot have a high chest deceleration since their seatbelt force limiters have been designed with higher force levels (two stages: 5–7 kN, 3–5 kN) in order to absorb the restraint energy within the limited chest deceleration and displacement available. The minicar C has a double seatbelt pretensioner, so that the initial chest deceleration level is high. The minicar D has a steering axis collapse system to absorb the energy, and as a result provides a larger chest displacement. Thus, with these design features, the seatbelt system of the minicars have been optimized for the high decelerations associated with the FWRB tests.

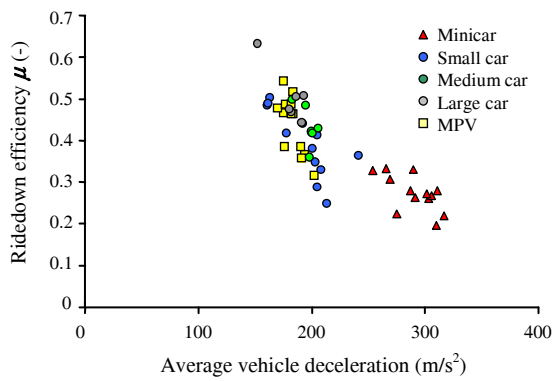

Figure 6. Ridedown energy calculated by driver chest acceleration in forward direction in FWRB tests

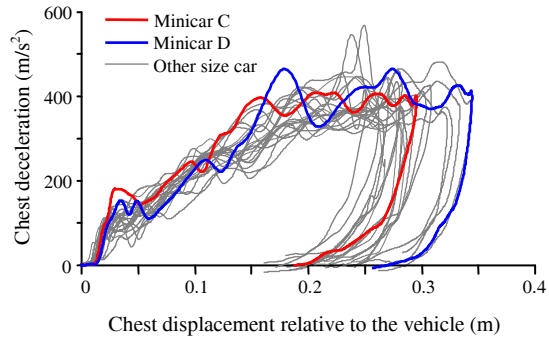

Figure 7. Driver dummy chest forward deceleration vs. chest forward displacement relative to the vehicle

In Figure 8, the head forward decelerations are shown for the minicars E and F, and the small sedan. The head deceleration is high for minicar because of high vehicle deceleration. As shown in Figure 8, the airbag of the minicar E could absorb the head motion energy effectively whereas the head deceleration of minicar F was delayed and the ensuing head deceleration was higher. For a minicar, the airbag could bottom out in more severe vehicle decelerations than experienced in NCAP tests.

The injury measures of the driver dummies are shown in Figure 9. It is found that the injury measures are affected by the upper and the lower limits set by NCAP. The chest acceleration and deflection of minicars tend to be high compared to other size cars. The tibia index is also high because of this high deceleration though the intrusion is small.

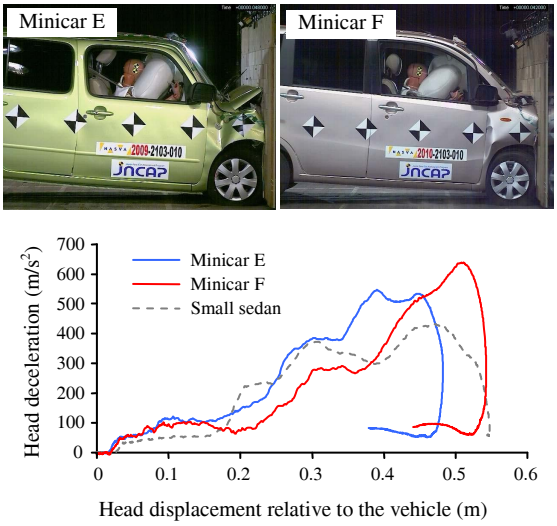

Figure 8. Head deceleration in FWRB tests

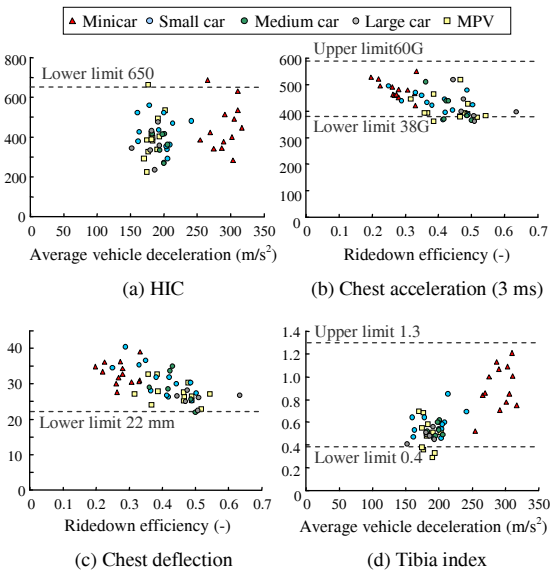

Figure 9. Injury measures of the driver dummy in FWRB tests (55 km/h)

FWDB TESTS

In the FWDB tests, the vehicle is impacted into a honeycomb barrier face that consists of two-layers (each layer of 150 mm depth) [2]. The honeycomb is effective in making the deformation mode of the vehicle structures in this test comparable to that in car-to-car crashes, and can mitigate the engine dump force which is a significant contribution toward evaluating the structural force distribution with the load cell wall. The honeycomb face had little effect on the vehicle deceleration pulse, so that the FWDB test also provides a high deceleration test from which to evaluate the performance of the restraint system.

Vehicle Deformation and Acceleration

Figure 10 presents the deformation of minicars after the FWDB tests. The front structures does not deform uniformly in the FWDB test because of the honeycomb resistance force. The stiff front rails penetrated into the honeycomb, whereas the weak bumper cross beam could not push through the honeycomb to the same level as the front rails. The other structures deformed and the engine moved rearward. Accordingly, the intrusion into the passenger compartment of the minicars was larger in the FWDB tests as compared to that in the FWRB tests. In car-to-car crashes, the front structures also do not deform uniformly since the car crashes into structures with various stiffnesses. It has been determined that the structural deformation mode in the FWDB test is more comparable to that in car-to-car crashes as compared to that in the FWRB test.

Figure 10. The deformation of minicars in a FWDB test (55 km/h)

The accelerations of the vehicle and the occupant chest in a minicar are shown in Figure 11 for a FWRB and DWDB test (impact velocity was 55 km/h). The crash pulse of the vehicle in the FWDB test is rear-loaded as compared to that in FWRB test. In the FWRB tests, a high initial acceleration occurred due to the immediate axial loading and collapse of the front rail. On the other hand, in the FWDB test the initial acceleration was low since the axial collapse of the front rails did not occur to the degree experience in the FWRB test. The TTF, based on a sensor algorithm which activates the seatbelt pretensioner and the airbag deployment, would late in the FWDB tests if the sensor algorithm was designed to activate by detection of an initial high acceleration caused by the front rail axial collapse in an FWRB test.

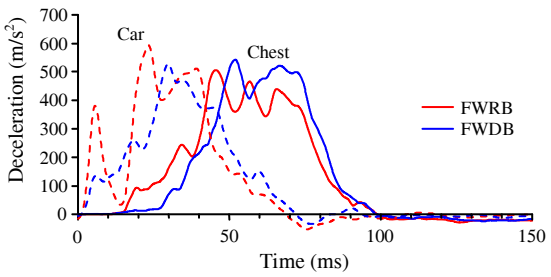

Figure 11. The vehicle and the chest deceleration in forward direction of a minicar in FWDB test (55 km/h) and FWRB test (55 km/h)

Occupant Response

The vehicle acceleration in the FWDB as well as the FWRB tests provides a large loading on occupant dummies provides a severe crash condition with which to evaluate the performance of restraint system. The injury measures of the driver dummies (Hybrid III AM 50th) between the FWRB and the FWDB tests were compared. Figure 12 shows the HIC and the chest acceleration. In general, these acceleration-base injury measures of minicars in the FWDB tests are higher than those in the FWRB tests. The injury measures of the lower extremities, such as the femur force and tibia index, were comparable between the two tests though they were distributed significantly (not shown in Figure 12).

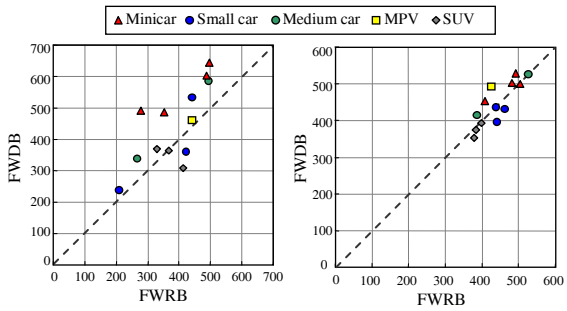

(a) HIC (b) Chest 3ms (m/s²)

Figure 12. The comparison of injury measures of driver dummies in FWRB and FWDB tests

In order to understand the reason that led to the higher injury measures of the dummies in minicars in the FWDB tests, a simulation using a simple spring-mass model was carried out. The restraint spring characteristics were estimated from the Hybrid III chest forward acceleration and the chest displacement relative to the vehicle (Figure 13(a)). The stiffness of the restraint system spring normalized by the occupant mass (k/m) was approximated from the initial acceleration-displacement curve. In the FWRB test, the chest acceleration increased with chest displacement since the seatbelt pretensioner activated immediately. The TTF was later in the FWDB test, and this delay was incorporated as the slack in the seatbelt spring (0.028 mm).

The vehicle accelerations measured in the FWRB and FWDB tests (see Figure 11) were applied to the simple-mass spring model as an acceleration field. Figure 13(b) shows the occupant acceleration calculated from the simulation. The initial acceleration agrees with that in the experiments up to the time when the seatbelt force limiter started to work. Accordingly, the loading on the dummy can be estimated with the maximum deceleration of the occupant mass in the model. The maximum occupant decelerations were 632 m/s^2 and 647 m/s^2 in the models of the FWRB and FWDB, respectively. When the seatbelt slack was set to zero in the FWDB test, it was found that the maximum deceleration dropped to 607 m/s^2. Consequently, the chest acceleration of the Hybrid III in a FWDB test can be higher than that in a FWRB test because of the late TTF, even though the vehicle crash pulse in FWRB test is more severe for occupants.

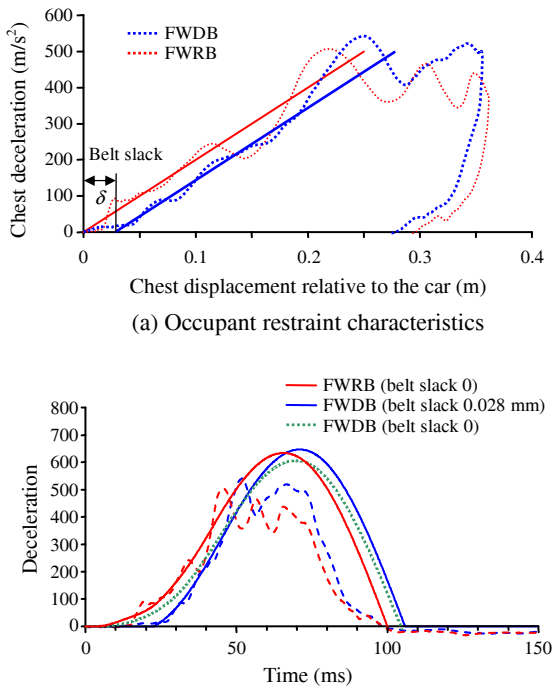

(a) Occupant restraint characteristics

(b) Occupant response

Figure 13. The chest forward acceleration in FWRB and FWDB based on simple spring-mass model

The delay in the initiation of the airbag deployment led to a higher pressure of the airbag because the forward moving dummy resulted in the airbag deployment space being smaller. The airbag force was exerted on the dummy face in the upper direction. The neck rearward moment (My) increased, and the neck shear force (Fx) was higher. In addition to the deceleration force of the airbag, this neck shear force (Fx) that was applied to the head in the rear direction induced a high deceleration of the head, which in turn led to high HIC value. The high airbag pressure also resulted in a large rebound of the dummy head, and caused the time duration of the head acceleration to be longer. These also contributed to the higher HIC.

There was an observed trend that the TTF of minicars was late in the FWDB tests. This TTF was compared to those of the FWRB, ODB, and car-to-car tests. The vehicle deceleration pulse depends on the crash configuration, and it was necessary to take the vehicle deceleration-time history into account when examining whether the TTF is determined to be at the proper time. Therefore, the "5 inch (127 mm) – 30 ms" criterion was used to evaluate the airbag deployment start time. The unbelted occupant displacement (x) with respect to the vehicle is calculated as [3]:

$$x = -\int_0^t \int_0^t a(t)\,dt\,dt \qquad (3)$$

where $a(t)$ is the occupant acceleration. The unbelted driver will not be injured by a deploying airbag if the airbag deployment is completed by the time when the displacement of the unbelted driver (x) reaches 127 mm. Taking the airbag inflation time into account, the TTF should be 25 to 30 ms before this time. Figure 14 provides a plot of the airbag deployment start time (t_s) vs. time when the unbelted occupant reaches 127 mm ($t_{5''}$) for minicars in FWDB, FWRB, and car-to-car crash tests. The time difference from when the airbag starts to deploy to when the unbelted occupant reaches 127 mm (t_s–$t_{5''}$), can be a measure of the delay of the TTF or the airbag deployment initiation time. From Figure 14, it is found that the airbag deployment start time (t_s–$t_{5''}$) in FWDB tests is between the FWRB tests and ODB tests, and is later than that in the car-to-car crashes with a large overlap ratio (>50%). It is likely that the airbag deployment start time (t_s–$t_{5''}$) is more dependent on crash configuration (overlap ratio).

The late TTF of minicars in the FWDB tests could be improved if the sensor locations and the vehicle structures were improved. This modification will contribute to ensure an appropriate airbag deployment initiation time in the cases where the structural interaction is not acceptable. However, the effectiveness of this modification would need to be verified because the late TTF of minicars in the FWDB tests might not reflect the TTF in car-to-car crashes.

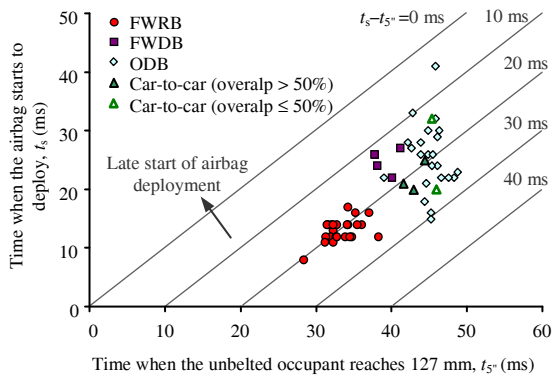

Figure 14. Minicar crash tests shown by airbag deploy start time and the time when the unbelted occupant reached 127 mm

ODB TESTS

In the ODB tests, the vehicles side are impacted on the driver side into an EEVC barrier with 40% overlap of vehicle width. The ODB tests can be used to evaluate the integrity of the passenger compartment. Generally, the average acceleration of the vehicle model in the ODB tests is lower and proportional to that in the FWRB tests. The stiffness mismatch between minicars and other size cars can be observed relative to the honeycomb stiffness. For minicars, the honeycomb still deforms even during the phase of the passenger compartment deformation, and after the test there remains residual crushable depth available in the honeycomb. This situation is different from other size cars for which the honeycomb bottoms out completely. Particularly for a large car, the honeycomb bottoms out even when only the structure in front of the engine is deforming.

Figure 15 shows the relation between the firewall intrusion and the maximum vehicle deformation. Because of the limited size of the engine compartment, the firewall intrusion of minicars increases from the maximum vehicle deformation of 0.8 m, and it exceeds 0.1 m with a vehicle deformation of 0.9 m. For small cars, the firewall intrusion tends to be large; however, for medium and large cars, the firewall intrusion increases as the maximum vehicle deformation is 1.2 m or more.

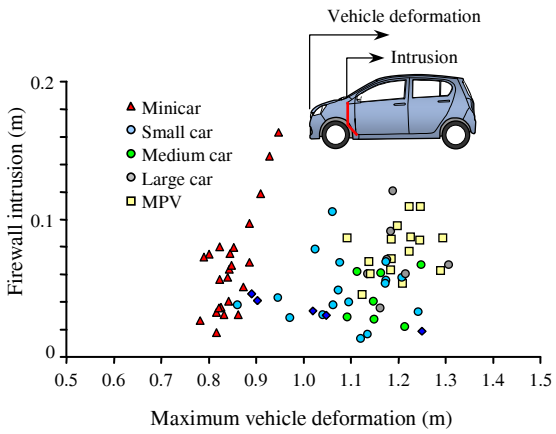

Figure 15. The intrusion into the passenger compartment in ODB tests at 64 km/h

The injury measures of the driver dummy (Hybrid III AM50th) in the ODB tests are shown in Figure 16. Several parameters were examined that could relate with the injury measures. The average vehicle deceleration, chest acceleration and chest deflection from the FWRB tests, and the firewall intrusion were selected to determine if they had a correlation with each injury measure. The injury measures in the ODB tests are lower than those in the FRWB tests, except for the tibia index. There is a tendency that the chest acceleration and chest deflection in the ODB tests are proportional to and lower than those in the FWRB tests. The tibia index is higher as the firewall intrusion is 0.12 or more, which corresponds to maximum vehicle deformation of minicar 0.9 m (see Figure 15). The tibia index in the ODB tests is higher than that in the FWRB tests because of this large intrusion.

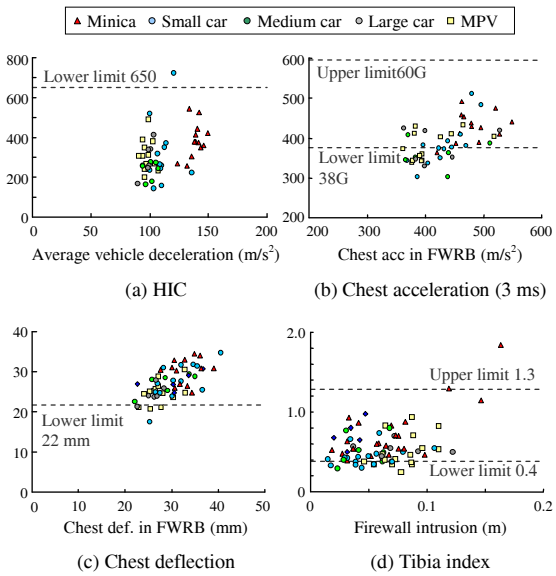

Figure 16. Injury measures of driver dummy in ODB tests (64 km/h)

CAR-TO-CAR CRASH TESTS

Three car-to-car crash tests including minicar were reviewed. Table 1 presents the crash test conditions. In addition to the closing velocity, the velocity change of the minicar from the initial velocity V_{10} to the common velocity V_c during impact is tabulated to compare the crash severity with NCAP (55 km/h).

Table 1. Crash condition in car-to-car tests

No.	Crash configuration	Minicar (test mass)	Opposite car (test mass)	Closing vel. ($V_{10} - V_c$)
1	Offset (overlap 50%)	Minicar 1120 kg	Small car 1313 kg	100 km/h (55.5 km/h)
2A 2B	Full-width 2A: original ride height 2B: front rail height match	Minicar 1024 kg	Large car 1695 kg	100 km/h (63.3 km/h)
3	Overlap 85%	Minicar 900 kg	MPV 1760 kg	80 km/h (53.4 km/h)

In Test 1 [2], the minicar was impacted into a small car. The velocity change of the minicar was 55.5 km/h, which is similar to the NCAP impact severity (55 km/h). The front rail of the minicar made contact with the bumper cross beam of the small car; whereas the front rail of the small car contacted the air conditioner compressor of the minicar. The front rails of both cars deformed efficiently, and as a result the passenger compartment of the minicar was intact. The injury measures of the driver and the front passenger dummies (Hybrid III AM50th) in the minicar were

compared between the car-to-car test and the ODB test (64 km/h) in Figure 18. All of the injury measures of the driver dummy in the minicar in the car-to-car tests were similar to those in the ODB tests 64 km/h, and were less than the injury assessment reference values (IARVs).

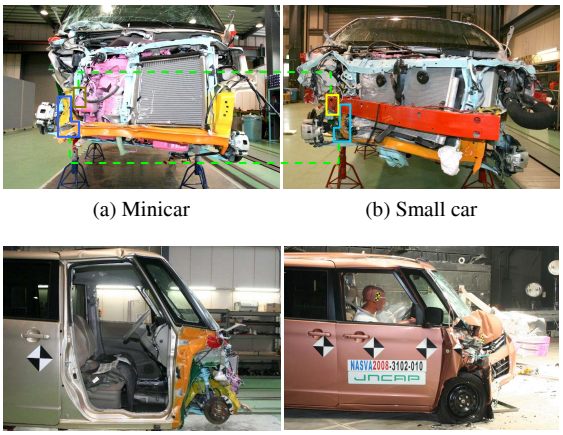

(a) Minicar (b) Small car

(c) Minicar (d) Minicar in ODB 64 km/h

Figure 17. The deformation of minicar in crash into a small car (Test 1)

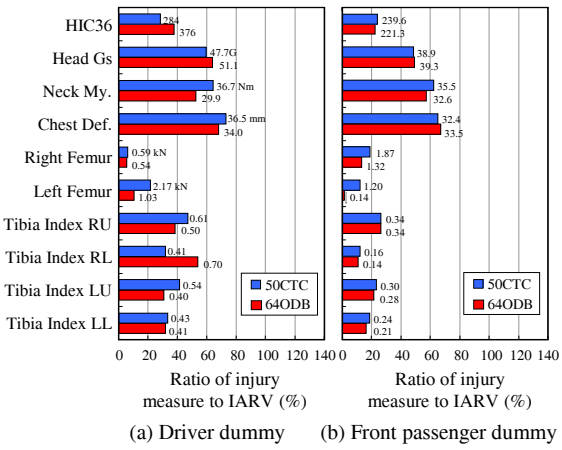

(a) Driver dummy (b) Front passenger dummy

Figure 18. The injury measures of minicars in car-to-car test (Test 1) compared with those in ODB test

The minicars and the large cars were impacted at the original ride height (Test 2A) and front rail height matching (Test 2B) [5]. In the original ride height, the front rails of both cars passed by each other, and the upper area of the minicar was engaged. The fascia moved rearward and the steering axis rotated upward. The force displacement characteristics in Test 2B were comparable with those in the FWRB tests at 55 km/h (Figure 19). Because of the mass ratio of the two colliding cars, the deceleration was higher for the minicar, and it was less for the large car than occurred in the FWRB tests. However, the car deformation in the car-to-car tests can be predicted from the crash test against a wall test since the crash interface behaves like a wall if the structural interaction is good. These tests demonstrated the effectiveness of front rail height matching.

The injury measures of the driver and the front passenger dummies (Hybrid III AM50th) were compared for the original ride height and for height matching. In Test 2A (original height), the large intrusion led to large femur force and tibia index. The steering axis upper rotation resulted in a large chest acceleration and neck extension moment.

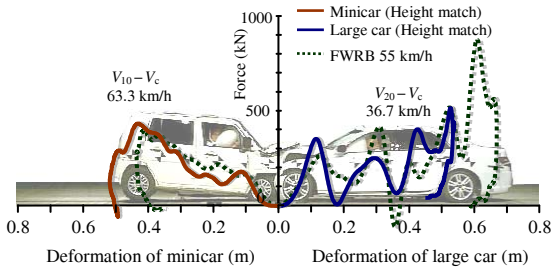

Figure 19. The deformation of minicar in crash into a small car (Test 1B: front rail height matching)

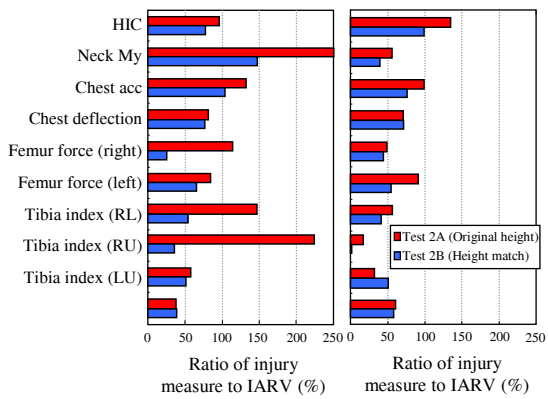

(a) Driver dummy (b) Front passenger dummy

Figure 20. The injury measures of minicars in car-to-car test (Test 2A and 2B)

Test 3 was conducted to perform an accident reconstruction for a frontal collision between minicar and multi purpose vehicle (MPV). The minicar and the MPV were impacted with an 85% overlap of the front passenger side of the minicar. A Hybrid III AF05th was seated on the driver side in the minicar. The MPV did not have a bumper cross beam, and the engine was not located in the front of the vehicle. In the test, the structural interaction was not good. However, the left front rail of the MPV was stopped by the engine of the minicar. One of

the driver seat attachment bolts (rear left-hand) on the floor fractured in the minicar, and the driver dummy moved forward. As a result, the chest acceleration was 599 m/s^2, the chest deflection was 37 mm, and the femur force was 2.3 kN. The HIC was small (298).

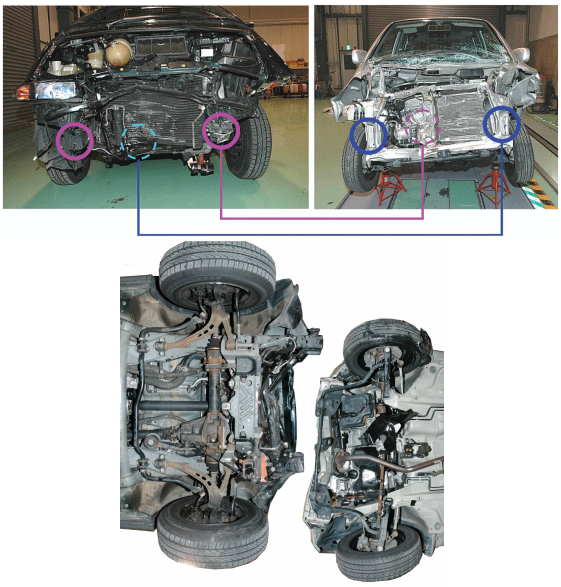

Figure 21. Structural interaction of minicar-to-MPV crash test (Test 3)

In the three car-to-car tests of the minicars, the structural interaction was determined to be acceptable because the engine of the minicar interacted with the structure of the other car, even though the minicar either has no bumper cross beam or has a weak bumper cross beam. This is not inconsistent with the general agreement that the front rail height matching between cars is a prerequisite, which was confirmed from Tests 2A and 2B. The load path from the engine to the suspension member and the passenger compartment is important for minicars.

DISCUSSION

Accident data show that the injury risk of occupants in minicar in all accidents was comparable to that for other size cars. However, the number of fatal and serious injuries to occupants in minicars is larger than other size of cars in vehicle-to-vehicle collisions. One reason for this high injury risk is due to the high deceleration pulse. Another reason is that the intrusion into the compartment of minicars is large since the length of engine compartment (i.e., available crush space) is limited.

The minicars showed good occupant protection in FWRB and ODB crash tests. The minicars have been highly optimized for severe crash tests for both FWRB (55 km/h) and ODB (64 km/h) tests. Minicars show high deceleration pulses since the size of the engine compartment is limited, and the passenger compartment is designed to remain intact. To reduce injury measures of dummies in these severe crash pulses, the seatbelt limiter force of minicars (5 kN) is designed to be higher than that of larger size cars (4–5 kN). This force level might be too severe for elderly people. From accident analysis, chest injuries constitute the largest number of injuries among the body regions to drivers [1]. The main injury sources to the chest were the steering wheel and seatbelt. Many accidents occur at lower velocities than these crash tests. Moreover, minicars are used in cities and impact velocities are inclined to be low. In order to reduce the number of serious injuries, it is necessary to consider the occupant protection of minicars at lower impact velocities than the impact speed specified for the crash tests conducted in the regulation and NCAP.

In the car-to-car crash tests, minicars showed reasonable structural interaction. Though the minicars do not have multiple load paths, the structural interaction was acceptable since the engine was located forward in the vehicle, interacted with the structures of the opposite car, and worked as a load path. In the evaluation of the structural height as measured from the barrier forces in the FWRB and FWDB tests, it might be necessary to develop a measure for the effect of engine on structural interaction. The passenger compartment was intact and the injury measures of driver dummies were less than the IARVs when the impact severity was less than NCAP (55 km/h), though the delta-V of minicars in the car-to-car crashes is inclined to be high because of the mass ratio of the colliding vehicles.

The trend of sales of minicars and small cars will continue when the user demands and the economical situation is considered. Minicars have a stiff front structure and a strong passenger compartment with optimized restraint system. The minicars will be a good example to ensure the crashworthiness of future hyper-mini electric vehicles.

CONCLUSIONS

For minicars, the size is limited and the vehicle mass is small. The crashworthiness of minicars was investigated from various crash tests.

1. The restraint system of minicars was highly optimized using a seatbelt pretensioner, force limiter, and steering axis collapse for the occupant protection when the vehicle was subjected to a high deceleration as experienced in FWRB tests.
2. In the FWDB tests, the TTFs of minicars were inclined to be later than those in the FWRB tests. Because of this later TTFs, the HIC and chest acceleration of the dummies in the FWDB tests can be higher than those in the FWRB tests even though the vehicle crash pulses in the FWRB tests were more severe for the occupants.
3. The intrusion of the passenger compartment in the ODB tests tends to be large because of the limited size of the minicars. The injury measures of the driver dummies in the ODB tests were less than those in the FWRB tests, except for the tibia index. The tibia index exceeded the IARV when the firewall intrusion was 0.12 m or more.
4. In the car-to-car crash tests of minicars, the structural interaction was found to acceptable due to the engine involvement, and the passenger compartment remained intact. When the impact severity was less than that of an NCAP test, the injury measures of the driver dummies were less than the IARVs.

ACCKNOLEGEMENT

The authors would like to express gratitude to Ministry of Land, Infrastructure, Transport and Tourism (JMLIT), National Agency for Automotive Safety & Victims' Aid (NASVA), Japan Automobile Manufacturers Association (JAMA) for their providing test data.

REFERENCES

[1] ITARDA, Report of accident investigation and analysis 2011, March 2012 (in Japanese).

[2] Japan, Performance as test procedure of the PDB and ODB tests for the light and heavy cars, Informal Group on Frontal Impact 5th meeting, UNECE, 2009.

[3] Huang, M., *Vehicle Crash Mechanics*, CRC Press, 2009.

[4] Edwards, M., Davis, H., Thompson, A., Hobbs, A., Development of test procedures and performance criteria to improve compatibility in car frontal collisions, Proc. Inst. Mech. Engrs. Vol. 217, Part D, J. Automobile Engineering, 2003.

[5] Yonezawa H., Mizuno, K., Hirasawa T. et al., Summary of activities of the Compatibility Working Group in Japan, Paper Number 09-0203, 21st International Technical Conference on the Enhanced-Safety of Vehicles, Stuttgart, Germany, June, 2009.

SEVERE PARTIAL OVERLAP CRASHES – A METHODOLOGY REPRESENTATIVE OF CAR TO CAR REAL WORLD FRONTAL CRASH SITUATIONS

Lotta Jakobsson
Anders Kling
Magdalena Lindman
Linus Wågström
Anders Axelson
Thomas Broberg
Graeme McInally

Volvo Car Corporation
Sweden

Paper Number 13-0294

ABSTRACT

Frontal crashes can occur in numerous ways, including differences in degree of overlap, impact speed and angle of interaction. This poses special challenges with respect to structural design as well as occupant protection.

Traditionally, regulatory and consumer information crash testing procedures mostly focus on full frontal overlap and 40% overlap. In the real world, small overlap crashes where load paths of less than 30% of the vehicle's width and crashes with no front longitudinal members engagement are shown to represent an important share of frontal crashes resulting in occupant injuries. Thus it is essential to understand which impact configuration that would capture the important characteristics of small overlap crashes, yet being representative for a variety of car-to-car frontal impact scenarios, providing a complement to standardized frontal impact testing.

Based on real world crash data, important car-to-car frontal impact scenarios are identified and mechanisms studied. Full scale crash tests and finite element crash simulations are performed in order to evaluate different car to car configurations, forming the basis for studying structural load paths, focusing on structural design and occupant protection.

A crash test method, addressing 25% overlap against a fixed rigid barrier with a radius of 150 mm is found representative for a variety of car-to-car frontal impact scenarios, reflects mechanisms in real world crash situations and is a good complement to conventional frontal impact test methods. These findings support the findings by Planath et al. (1993), regarding Severe Partial Overlap Collision (SPOC), with 25% overlap against a fixed rigid barrier with velocities up to 64 km/h.

INTRODUCTION

In the late 1970s, the US-NCAP began frontal crash testing, comprising full overlap into a rigid barrier with a velocity of 56.3 km/h (Hackney and Kahane, 1995).

During the 1990s, partial overlap crashes were identified as a significant contribution to frontal crash injuries and fatalities using data from the UK (Hobbs, 1991), US (O'Neill et al., 1994), Germany (Scheunert et al., 1992) and Sweden (Planath et al., 1993, Kullgren and Ydenius, 1998). Although the methodologies varied, the findings identify the important share of serious frontal crashes involving partial loading of the cars' front end. This led to consumer information crash tests, by the car magazine Auto Motor und Sport in Germany, with 50% overlap into a rigid barrier (AMS, 1990). In 1996, a method comprising a deformable barrier with 40% overlap and impact speed of 64 km/h was used in the UK, simulating a car-to-car frontal collision between two similar cars with 50% overlap. This method was soon adopted within Europe by EuroNCAP. Today most vehicles are evaluated based on these full-frontal and moderate offset crash tests.

In a more recent real world study, Lindquist et al. (2004) found that small overlap crashes where load paths of less than 30% of the car's width is engaged, represented 48% of belted occupant fatalities in frontal crashes in Sweden. This stressed the need for further development of crash test procedures to better address small overlap crashes with no front longitudinal member engagement. Brumbelow and Zuby (2009) and Rudd et al. (2009), studied real world cases in US (NASS- CDS) with serious injuries for belted occupants of modern vehicles. Both suggested that future test programs promoting structural designs that address small overlap could reduce serious injuries in frontal crashes.

Sherwood et al, (2009) assessed the characteristics of small overlap frontal crashes and concluded that despite structural improvement prompted by offset crash tests, vehicle structures must improve if they are to prevent occupant compartment intrusion when a vehicle is loaded outboard of longitudinal structural members. Eichberger et al. (2007) investigated the crash statistics using GIDAS (German In-Depth Accident Study) and Austrian databases and concluded that, in small overlap situations, the longitudinal members are not involved and the wheel-to-wheel contact provides a load path into the occupant compartment which endangers the safety cage. Eichberger et al. (2007) proposed a car-to-car test method with 17% overlap collinear impact with a closing velocity of 112 km/h, to address the small overlap scenario. Also, studies by National Highway Traffic Safety Administration (NHTSA) (Bean et al., 2009) and The Insurance Institute of Highway Safety (IIHS, 2012) have initiated development of test methods in this area.

IIHS published in 2012 results from eleven vehicles tested in a car-to-barrier method using 25% overlap of the vehicle front with an initial velocity of 64 km/h (IIHS, 2012). NHTSA stated its intent to further analyze small overlap as well as oblique frontal crashes in its Vehicle Safety Rulemaking & Research Priority Plan 2009-2011 (NHTSA, 2009). This was followed by studies on evaluating the small overlap impact procedure's ability to replicate real world injury potential, complemented with tests comparing 7 different vehicles (Saunders et al., 2011 and 2012). It was found that the tests demonstrated head contact locations that are common in the field, torso loading of the restraint system and steering wheel, as well as a distribution of injury assessment values that are representative of the field injury risk

Small overlap frontal crashes, which are not currently addressed by federal standards or consumer information testing, account for a significant percentage of serious frontal crashes (Brumbelow and Zuby, 2009, Lindquist et al, 2004). Sherwood et al. (2010) studied the configurations and speeds of these real world crashes to understand and develop a potential crash test to evaluate vehicle crashworthiness in these types of crashes. By comparing the estimated closing relative velocity (delta-V) using field reconstructions techniques to the delta-V calculated on vehicle accelerometer data for crash testing, they found that an impact speed in the range of approximately 64 km/h would represent a significant portion of such real crashes causing severe and fatal injuries.

Occupant compartment intrusion was the primary injury mechanism and was found to have a strong correlation with overall injury severity (Sherwood et al. 2009). Of the occupants with an AIS2+ head injury, 80% of the head injuries came from contact with structures on the outboard side of the vehicle (e.g. A-pillar, striking vehicle, trees), indicating an influence of lateral occupant movement (Sherwood et al. 2012). Performing numerous full-scale car crash tests in a variety of small overlap crash configurations, Sherwood et al. (2012) emphasizes the significant lateral movement during the early phases of the crash, causing the driver dummy to move forward and outboard.

Severe partial overlap crashes where engaged load paths represent less than 30% of the vehicle's width and crashes with no engagement of front longitudinal members are shown to represent an important share of frontal crashes resulting in occupant injuries. Thus, it is essential to understand which impact configuration that would capture the important characteristics of small overlap crashes.

The objective of the study is to evaluate a car-to-barrier crash test set-up in its capability to represent a variety of car-to-car frontal impact scenarios and capture important real world characteristics of severe partial overlap crashes.

METHODS

Based on real world crash data, important car-to-car frontal impact scenarios are identified and mechanisms studied. Finite Element (FE) crash simulations of different car-to-car configurations helps to identify the crash configurations of high structural loading. Full scale crash tests are performed to replicate the real world mechanisms of severe partial overlap crashes. A study lay-out is shown in Figure 1. The different parts are described in detail further down.

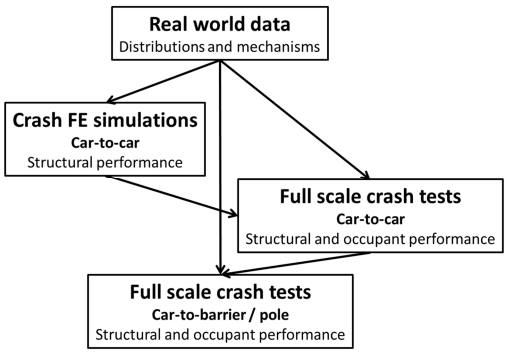

Figure 1. Study lay-out.

Real world data

The real world crash data is a subset of Volvo Cars Accident Data base, which contains Volvo passenger vehicles in Sweden where the repair cost due to a crash exceeds a specified level. The limit of repair cost criterion is currently 4,500 euro. Inspectors from Volvia (If P&C Insurance), the company with which all new

Volvo passenger cars are insured, identify the crashes. Photos and technical details of the vehicles are sent to Volvo Cars' Accident Research Team. A detailed questionnaire is sent to the owner of the vehicle to gather information about the crash, the car and the occupants. With the approval of the occupants, medical records are requested (when applicable) and coded by a physician within Volvo Cars' Accident Research Team. Injuries are coded according to the Abbreviated Injury Scale (AIS) (AAAM, 1985). To date, the database contains a total of 42,619 Volvo cars with 70,771 occupants, involved in crashes from 1976 to 2009. More information about the database is found in Isaksson-Hellman and Norin (2005).

In a selection of Volvo cars from the700-series to newer models, a total of 4,770 frontal impact cases are used to study the deformation pattern distributions and the injured body part distribution. The SAE Collision Deformation Classification (CDC) codes were used to select the dataset (SAE, 1980). Belted drivers involved in a single frontal impact (direction of impact 11-1 o'clock) were selected including crashes with deployed as well as un-deployed airbags. Multiple impact crashes and crashes with rollover events were excluded. The cars selected had vertical damage to, at a minimum, the front and up to the hood. The general damage type for the crash was either 'wide', 'narrow', 'corner' or 'sideswipe'.

Also, one real world case of severe partial overlap crash is presented in more detail to illustrate typical mechanisms.

Tests

Results from hundreds of crash simulations and several full scale crash tests are used for detailed analyses of structural performance and integrity. The full scale tests are also used for study the occupant kinematics.

Crash simulations, Computer simulations of the full vehicle response in car-to-car situations were performed.

A methodology to evaluate a large set of crash configurations was developed, using state-of-the-art FE models. This methodology aimed at expanding the capability of crash simulation beyond what is practically possible by physical crash testing. A detailed description of the methodology is published in Wågström et al. (2012). The study was based on structural evaluation criteria such as passenger compartment intrusion and vehicle deceleration. Special focus was directed to identifying “worst case” scenarios and developing means to visualize structural robustness and the imbalance that arises from oblique loading even when colliding vehicles are identical.

To cover a wide range of car-to-car crash scenarios, the lateral offset was chosen from 0 to 1,800 mm and oblique angle from 0 to 45° as illustrated in Figure 2. The combination of lateral offset and oblique angle was set up by rotating the bullet vehicle around a rotation center on the target vehicle followed by applying a lateral offset (Wågström et al., 2012). Initial velocities were chosen from 30 km/h up to 70 km/h for each vehicle, i.e. a maximum closing velocity of 140 km/h. In total, 378 full-scale car-to-car simulations in the 42 initial positions illustrated in Figure 2 were performed and compared in terms of structural response with the aim to identify a worst case structural loading in car-to-car situations.

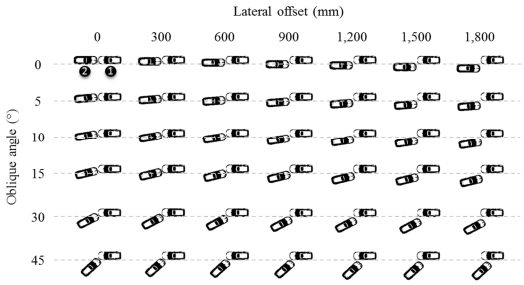

Figure 2 . Overview of simulated car-to-car crash scenarios.

Full scale crash tests, In total, seven different test set-ups, were performed and evaluated based on structural and occupant performance. Two of these are described more in detail in this study; one car-to-car test in an angle of 12 degrees and overlap arranged so that the longitudinal members strike each other without engagement, and one car-to-barrier test with a barrier radius of 150 mm and an overlap of 25% (Figure 3). The cars in the car-to-car crash were run at 35 mph each and the car in the car-to-barrier test at 40 mph.

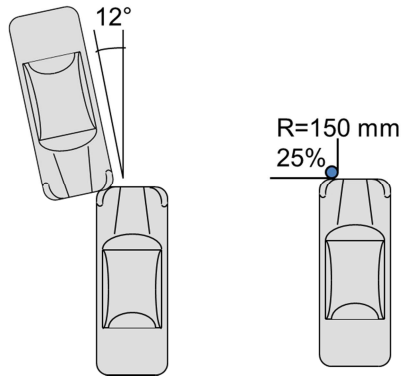

Figure 3. Car-to-car crash test set-ups.

The car-to-car test set-up was chosen based on the crash simulations and the car-to-barrier test was chosen based on correspondence to the car-to-car crash test results. The structural and occupant performance seen in the real world cases were aimed for in the tests. The desired performance was to expose the occupant area for both longitudinal and lateral accelerations in

order to promote an oblique motion of the driver against the A-pillar.

The lateral and longitudinal accelerations were measured in the door sill as shown in Figure 4a. The door aperture deformation was measured in four different points as illustrated in Figure 4b, as a measure for structural deformation.

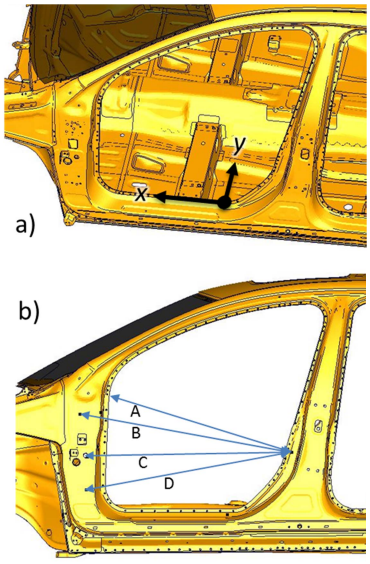

Figures 4. a). Location of accelerometer. b) Door aperture deformation measurement points.

A THOR dummy with modified shoulder enabling more humanlike motion in oblique loading conditions (Törnvall et al. 2008) was used.

RESULTS

Real world data

The distribution of 4,770 frontal impact cases with belted drivers are presented in Figure 5 with respect to the extent of frontal deformation; full overlap, 2/3 overlap and 1/3 or less overlap. It can be seen that 20% of the frontal impacts have driver side (left) overlap of 1/3 or less, while 15% and 25% is 2/3 driver side and full overlap respectively.

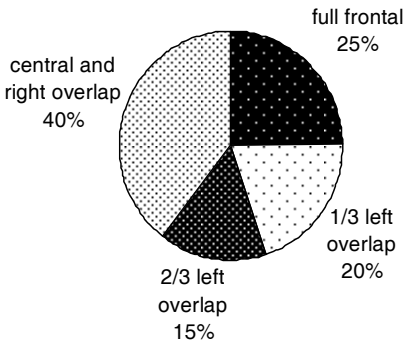

Figure 5. Distribution of horizontal deformation extent in frontal impacts with belted drivers.

For the frontal impact configurations analyzed, the distribution of some AIS2+ injured body regions of 274 injured drivers in total, is compared. Figure 6 displays the distribution of MAIS2+ injuries to the drivers' head and face, chest, lower extremities and upper extremities, respectively, per horizontal deformation extent.

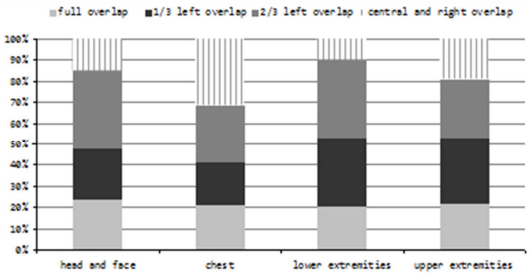

Figure 6. Distribution, by group of frontal horizontal distribution extent, of drivers MAIS2+ injuries to head and face (n=127), chest (n=95), lower extremities (n=112) and upper extremities (n=90).

Less than 1/4 of each of the drivers' injured body regions studied occur in full overlap frontal impacts, indicating that partial overlap account for a relatively higher injury outcome, Figure 6. The two driver side partial overlap groups hold a relatively higher frequency of MAIS2+ injuries. The injured drivers that were exposed to a 1/3 left side frontal impact, sustained 24% of the head and face injuries, Also, this group holds 20% out of chest injuries 35% of the MAIS2+ lower extremity injuries, and 31% of the upper extremities.

As a typical severe partial overlap real-world crash the following case was selected. A Volvo XC70 of model year 2008 impacted by a modern passenger vehicle of similar size with a narrow left side, slightly oblique (17% to the right) interaction. The car's speed at impact was approximately 80 km/h and the vehicle rotated substantially during impact. The driver of the vehicle was a 79 year old male. He sustained concussion with unconsciousness during 15 minutes, bruises on the chest and neck from the belt as well as bruises on the thighs. A photo of the exterior deformation is seen in Figure 7. The structural integrity was well maintained, resulting in an almost un-deformed foot-well area, see Figure 8. Based on vehicle kinematics as well as the head injury sustained, it is likely that the driver's head impacted the areas of the A-pillar and door structure. The frontal airbag was deployed, but not the Inflatable Curtain, which was in accordance with the specification of the vehicle.

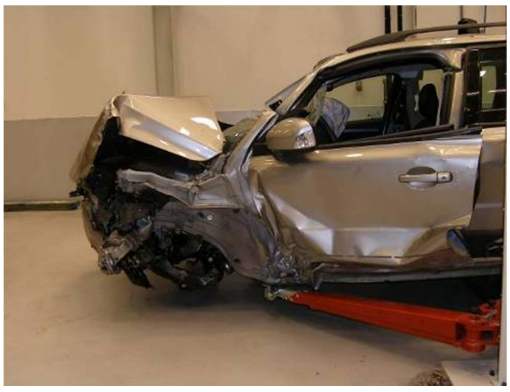

Figure 7. Exterior view of the in-depth real world case. Note, the pillars were cut for extrication purposes by the rescue squad at scene.

Figure 8. Photo of driver foot-well area of the in-depth real world case.

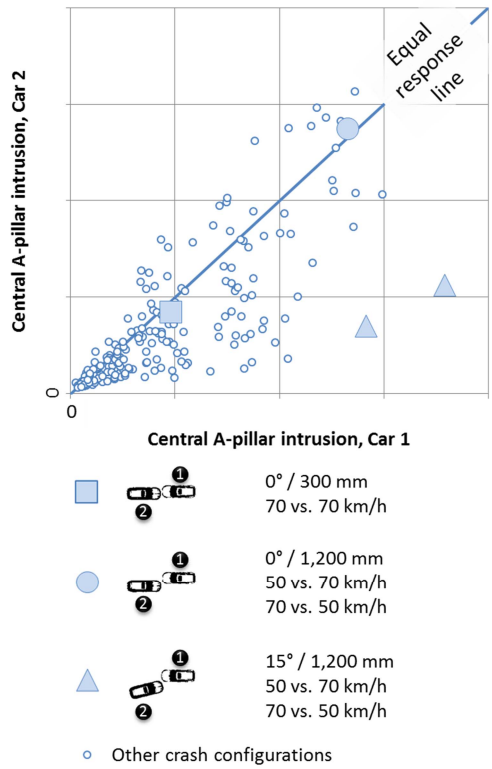

Figure 9. Central A-pillar intrusions for the two cars, respectively. Three specific load cases are highlighted.

Tests

Crash simulations, In terms of passenger compartment intrusion, a high degree of correlation between the central A-pillar intrusion and other measured intrusion areas was observed. The A-pillar intrusion was therefore proposed as a good indicator of the overall intrusion into the passenger compartment, and when this intrusion was compared between the different crash scenarios, the largest intrusions occurred at 15° oblique angle and 1,200 mm lateral offset, Figure 9. The findings from the simulation study were found to correspond well to the knowledge gained from real-world data as well as crash testing, indicating situations around 10-20° oblique angle and approximately 1/3 left overlap to represent the worst case structural loading in car-to-car situations.

Full scale crash tests, Exterior views of two cars tested in car-to-car and car-to-barrier configuration, respectively, are shown in Figure 10.

Figure 10. Exterior view of two cars tested in car-to-car (top) and car-to-barrier (bottom).

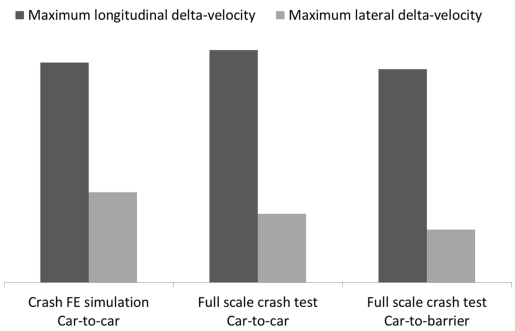

Figure 11. Longitudinal and lateral maximum delta-velocity at door sill, comparing the two full scale crash tests with the crash FE simulation.

Figure 11 shows a comparison of the longitudinal and lateral change of velocities measured at the door sill (as indicated in Figure 4a) for the two full scale tests and the car-to-car crash test simulation of 15° oblique angle and 1,200 mm lateral offset. The car-to-car and car-to-barrier full scale crash tests both include components of longitudinal as well as lateral change of velocity, in a similar magnitude. The values are also in line with the measurements from the car-to-car crash FE simulation, Figure 11. This provides an indication that the vehicle kinematics in the two test set-ups involves longitudinal as well as lateral acceleration affecting the occupant movement in line with the mechanism identified in real world situations. It is also an indication that the energy absorption and thus deformation pattern between the two test set-ups are similar.

Another measure of deformation is the door aperture opening measurement as shown in Figure 12, comparing the two full scale crash tests with the crash FE simulation of 15° oblique angle and 1,200 mm lateral offset. As can be seen in Figure 12, the deformations are overall minor and comparably similar between the two full scale crash test set-ups and the car-to-car crash FE simulation.

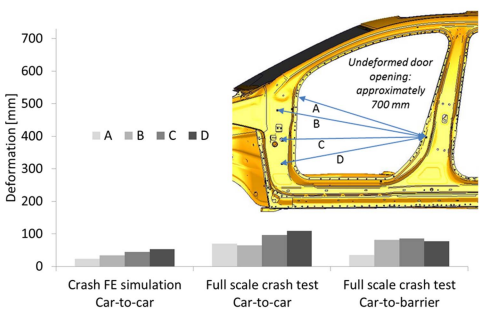

Figure 12. Deformation of door aperture deformation, comparing the two full scale crash tests with the crash FE simulation

In Figures 13 and 14, the maximum forward displacement of the driver dummy is shown, for the car-to-car and car-to-barrier full scale crash test, respectively. The crash test dummy in both tests, is the mid-size male dummy THOR, with modified shoulder as described in Törnvall et al. (2008). As can be seen in Figure 13, the driver dummy in the car-to-car full scale crash test has moved into a lateral position when in its maximum forward displacement position. The similar dummy kinematics is seen in the car-to-barrier crash test as well, illustrated with a photo of the maximum forward dummy displacement in Figure 14

Figure 13. Interior view on occupant maximum forward displacement in car-to-car test set-up.

Figure 14. Interior view on occupant maximum forward displacement in car-to-barrier test set-up.

DISCUSSION

Based on real world data, crash testing and simulations, this study confirms the crash test method which was presented already in 1993 by Planath et al. (1993). The method, called Severe Partial Overlap Collision (SPOC), addressing 25% overlap against a fixed rigid barrier was found representative for a variety of car-to-car frontal impact scenarios and a good complement to conventional frontal impact test methods. Over the years, frontal impact protection has been improved, however mostly focusing full

frontal overlap and 40% overlap in regulatory and consumer information crash testing procedures. In more recent years, the significance of small overlap crashes in relation to protection in other frontal crashes has been highlighted (IIHS, NHTSA). Using the SPOC method for more than three decades, the development of Volvo cars have improved with respect to small overlap frontal impacts. Jakobsson et al. (2013) presents real world data of Volvo cars showing continuous improved occupant protection in full frontal as well as 1/3 overlap frontal crashes.

Frontal crashes can occur in numerous different configurations. This study highlights one test configuration representative for evaluating structural integrity for a variety of crash situations of partial overlap and oblique frontal impacts, providing a valuable supplement to regulatory frontal impact test set-ups. Besides aspects concerning structural integrity, equally important is the determination and replication of occupant kinematics for reflecting real world situations with small overlap as well as oblique frontal impact scenarios. This is essential for structural performance around the occupant as well as restraint activation logic and robustness.

The knowledge regarding small overlap crash situations based on simulations of vehicle structures has been quite limited until recently, mainly for two reasons: simulation resources and model detail level. Since the response in small overlap situations by definition does not engage the main energy absorbing members of the front structure, chassis components represent the main load paths in this type of situation. This means that the FE tools, developed for axial buckling and bending of sheet metal, needs to be expanded to cover also deformation and possibly material failure of chassis components. By requiring detailed models in combination with a large set of impact configurations, exploring car-to-car robustness in small overlap situations becomes particularly intensive in terms of computer resources. The methodology developed by Wågström et al. (2012) represents an initial attempt to combine a high level of model detail with a comprehensive scope of impact configurations. However, updates to FE models appear to be needed based on the knowledge from small overlap situations; these updated models can then be employed to make even more detailed predictions on worst case scenarios and structural robustness.

Two full scale crash test set-ups were presented in this study. In total seven different full scale crash test set-ups were run. Two addition car-to-car tests were run to evaluate the sensitivity in test set-up with respect to overlap and impact point. None of them provided the structural interaction as desired. In one of the tests, too narrow overlap resulted in a side-swipe with low acceleration and too little structural interaction. In the other one, the longitudinal members just reached but did not overlap. In addition, four variations of car-to-barrier / pole were run. These tests provided information that a barrier radius smaller than 150 mm gave high structural deformations but not the desired kinematics of the driver. In a test set-up with a barrier radius of 250 mm the vehicle glanced off the barrier thus giving too low structural deformations although the desired driver kinematics were achieved.

In small overlap real world crashes, the injury causation mechanisms are often related to oblique occupant upper body movements caused by the oblique pulse direction, a large portion of glance off forces and rotation of the vehicles, increasing likelihood for injuries from outboard components such as the door and A-pillar (Lindqvist 2007, Scullion et al. 2010, Rudd et al. 2011). The driver in the in-depth real world crash described in the present study likely impacted his head due to his oblique outboard motion. In the full scale crash tests, the THOR dummy used was equipped with a modified shoulder specifically designed for oblique motions (Törnvall et al. 2008) and showed similar head impact areas as in the real world situations (Figures 13 and 14). Humanlike occupant kinematics leading to realistic head impact areas are important in order to drive the development of occupant protection technology in a real world effective way.

This study provides a wide overview including detailed analyses of car-to-car frontal collisions in oblique and small overlap situations, combining updated real-world crash data with full scale crash testing as well as state-of-the-art computer simulations. It provides insight into vehicle design for structural performance and occupant protection for these situations, offering important information on a representative test method, corresponding structural prerequisites as well as the mechanisms of injury for severe car to car frontal impacts. The car-to-barrier test set-up evaluated is found representative for a variety of real world frontal impact scenarios.

CONCLUSIONS

The Severe Partial Overlap Collision (SPOC) crash test method, addressing 25% overlap against a fixed rigid barrier with a radius of 150 mm is found representative for a variety of car-to-car frontal impact scenarios and reflects mechanisms identified in real world crash situations. This method provides a good complement to conventional frontal impact test methods especially driving the development of structural performance around the occupant as well as restraint activation logic and robustness.

REFERENCES

Association for the Advancement of Automotive Medicine (AAAM), The Abbreviated Injury Scale, 1985 Revision, Des Plaines IL, USA, 1985

AMS (Auto Motor und Sport). Die Sekunde der Wahrheit. Issue 19, page 127, 1990

Bean JD, Kahane CJ, Mynatt M, Rudd RW, Rush CJ, Wiacek C. Fatalities in Frontal Crashes despite Seat Belts and Air Bags - Review of all CDS Cases - Model and Calendar Years 2000-2007 - 122 fatalities, DOT HS 811 102, National Highway Traffic Safety Administration, Washington, DC, 2009

Brumbelow ML and Zuby DS. Impact and Injury Patterns in Frontal Crashes of Vehicles with good Ratings for Frontal Crash Protection, Proc. of the 21st ESV Conference, Paper No. 09-0257, Stuttgart, Germany, 2009

Eichberger A, Schimpl W, Werber C, Steffan H A New Crash Test Configuration for Car-to-Car Frontal Collisions with Small Lateral Overlap. Int. Journal of Crashworthiness, 2007: 12(2), 93-100

Hackney JR and Kahane CJ. The New Car Assessment Program: Five Star Rating System and Vehicle Safety Performance Characteristics. SAE Paper No. 950888, Warrendale, 1995

Hobbs C. The Need for Improved Structural Integrity in Frontal Car Impacts. Proc. of the 13th ESV Conference, Paper no. S9-O-12, 1991

IIHS (Insurance Institute for Highway Safety), "Status Report, Small Overlap Crashes", Vol. 47, No. 6, 2012

Isaksson-Hellman I and Norin H. How Thirty Years of Focused Safety Development has Influenced Injury Outcome in Volvo Cars, Proc. of the 49th Annual Association for the Advancement of Automotive Medicine Conference (AAAM), Boston, USA, 2005

Jakobsson L, McInally G, Axelson A, Lindman M, Kling A, Broberg, T, Fermér M, Wågström L. Severe Frontal Collusions with Partial Overlap – Two Decades of Car Safety Development, SAE Car Congress, Paper No. 2013-01-0759, Detroit, 2013

Kullgren A and Ydenius A. Front Impacts with Small Overlap; Real Life Data from Crash Recorder", Proc. of the 16th ESV Conference, Paper No. 98-S1-O-13, Windsor, Canada, 1998

Lindquist M, Hall A, Bjornstig U. Car Structural Characteristics of Fatal Frontal Crashes in Sweden, Int. Journal of Crashworthiness 2004, 9(6), 587-597

Lindquist M. Fatal Car Crash Configurations and Injury Panorama - with Special Emphasis on the Function of Restraint System. Umeå University Medical Dissertations, New series No ISSN 0346-6612-1079, SBM 978-91-7264-247-8, Department of Surgical and Perioperative Science, Umeå University, Umeå, 2007

NHTSA (National Highway Traffic Safety Administration). Vehicle Safety Rulemaking & Research Priority Plan 2009-2011, Docket ID NHTSA-2009-0108-0023, Washington, DC, November, 2009

O'Neill B, Lund AK, Zuby DS, Preuss CA. Offset Frontal Impacts - a Comparison of Real-World Crashes with Laboratory Tests. Proc. of the 14th ESV, Paper No. 94-S4-O-19, Munich, Germany, 1994

Planath I, Norin H, Nilsson S. Severe Frontal Collisions with Partial Overlap - Significance, Test Methods and Car Design. SAE Technical Paper No. 930636, 1993

Rudd RW, Bean J, Cuentas C, Kahane CJ, Mynatt M, Wiacek C. A Study of the Factors Affecting Fatalities of Air Bag and Belt-restrained Occupants in Frontal Crashes, Proc. of the 21st ESV Conference ESV, Paper No. 09-0555, Stuttgart, Germany, 2009

Rudd RW. Scarboro M, Saunders J. Injury Analysis of Real-World Small Overlap and Oblique Frontal Crashes, Proc. of the 22nd ESV Conference, Paper No. 11-0384, Washington, DC, 2011

SAE International Surface Vehicle Recommended Practice Collision Deformation Classification (CDC) SAE Standard J224, 1980

Saunders J, Craig MJ, Suway J. NHTSA's Test Procedure Evaluations for Small Overlap/ Oblique Crashes, Proc. of the 22nd ESV Conference, Paper No. 11-0343, Washington, USA, 2011

Saunders J, Craig M, Parent D. Moving Deformable Barrier Test Procedure for Evaluating Small Overlap/Oblique Crashes, SAE Technical Paper No. 2012-01-0577, 2012

Scheunert D, Justen R Herrmann R, Zeidler F, Decker J, Kallina I. "What is Realistic Frontal Offset Test Procedure", International Conference on Biomechanics of Impacts (Ircobi), 1992

Scullion P, Morgan RM, Hohan P, Kan C, Shanks K, Jin W, Tangirala R. A Re-examination of the Small Overlap Frontal Crash, Proc. of the 54th Annual Association

for the Advancement of Automotive Medicine Conference (AAAM), 2010

Sherwood CP, Nolan JM, Zuby DS. Characteristics of Small Overlap Crashes. Proc. of the 21st ESV Conference, Paper No. 09-0423, Stuttgart, Germany, 2009

Sherwood CP, Zuby DS, Nolan JM, Aylor DA. The Accuracy of Velocity Change Estimates in Small Overlap Frontal Crashes, ESAR Conference, Hanover, Germany, 2010

Sherwood C. Nolan J, Zuby D. Occupant Kinematics and Restraint Systems in Small Overlap Frontal Crashes, Airbag 2012

Törnvall FV, Holmqvist K, Davidsson J, Svensson MY, Gugler J, Steffan H, Haland Y. Evaluation of Dummy Shoulder Kinematics in Oblique Frontal Collisions, International Conference on Biomechanics of Impacts (Ircobi), 2008

Wågström L, Kling A, Norin H, Fagerlind H. A Methodology for Improving Structural Robustness in Frontal Car-to-car Crash Scenarios, submitted to the International Journal of Crashworthiness, 2012

DESIGN DRIVERS FOR ENHANCED CRASH PERFORMANCE OF AUTOMOTIVE CFRP STRUCTURES

Dr. Dirk Lukaszewicz
BMW Group
Munich, Germany
Paper Number 13-0302

ABSTRACT

Crashworthiness using innovative materials, such as carbon-fibre reinforced composites (CFRP) requires a new understanding of the material response to crash events. Composite fracture differs from existing plastic deformation in metallic structures. Vehicle design using composites requires a detailed understanding of the microstructural material features with respect to a given fracture behaviour, as well as updated vehicle concepts and architectures to account for this inherent difference of CFRP to metallic structures.
To design composites for energy absorption all factors need to be known and understood. This study was focused on providing an overview of the most relevant material parameters. Current challenges with respect to CFRP vehicle design are discussed and particular attention is devoted to energy absorbing composite structures
The work presented here is a preliminary approach to managing the complexity of composite development including both geometrical and microstructural design. Composite materials offer benefits in energy absorbing structures and are one way of further reducing the weight of a body-in-white while also maintaining safety levels. However, such weight savings can only be achieved with a purposeful composite design. The work presented herein will highlight innovative aspects of crashworthiness with respect to composite materials.

INTRODUCTION

The use of advanced composites reinforced by long or continuous glass (GFRP) and carbon fibre reinforced plastics (CFRP) is not recent and can be traced back to their extensive use in Formula 1 vehicles from the 1980's [1]. One motivation for the use of advanced composites in Formula 1 and sports cars was to reduce weight while also maintaining or increasing safety levels.
Since then, advanced composites have migrated into the super-sports car segment and sports car segment. All existing automotive applications have certain features in common, which can be summarized as follows:

1. Advanced Composite Manufacturing technologies are similar to aerospace and Formula 1 procedures, yielding a relatively low production volume in an automotive context.
2. Composites are used to form a monocoque around the passenger compartment, while energy absorbing crash structures are mostly made using aluminium parts, with a few exceptions mainly in the super sports car segment.

Consequently, the use of composites in mass-market applications has been limited to few parts such as roofs and bumpers [4], which do not necessarily serve as main load path in a high speed crash event for legal safety testing, such as FMVSS (USA) [2] or ECE (Europe) [3]. Future high volume plastic intensive vehicles (PCIVs) will have to achieve robustness in a crash for multiple different load cases currently not relevant to CFRP automotive structures. To achieve this the designer needs to choose not only the geometry of the structural component but also design the microstructure, such as the orientation of the fibres in the component. This work will thus be concerned with the drivers for robust vehicle design in energy absorption high-speed crash events. Existing concepts for frontal impact are used to illustrate the differences in material behaviour and this is then extended to innovative concepts for energy absorbing crash structures.

DESCRIPTION OF PROJECT i CRASH CONCEPTS

Project i is BMW's product family for innovative electric and hybrid vehicles. Until today two vehicles have been announced in the product family, the i3 (often referred to as Megacity Vehicle MCV) and the i8, see Figure 1 and Figure 2. Both vehicles share the principle vehicle architecture of a "Life"-Module, or monocoque, made from CFRP and a "Drive"-Module made from aluminium. The drive module incorporates the main load path for frontal and rear impact, which is consequently made from aluminium.

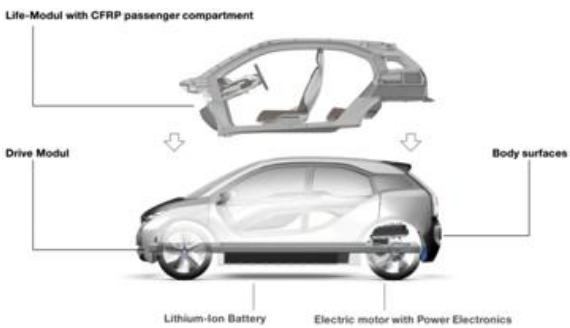

Figure 1: i3 vehicle architecture.

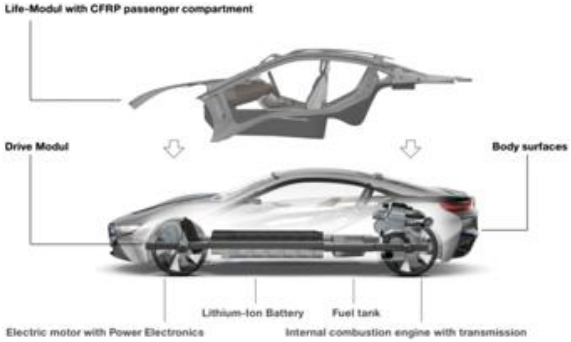

Figure 2: i8 vehicle architecture.

The drive module represents a good compromise between various requirements, such as fatigue, stiffness and crash energy absorption. However, the specific energy absorption (SEA) and stiffness for composites may be higher than for comparable aluminium structures. Consequently, composites may be one way of reducing the weight of the body-in-white (BIW) further while also maintaining crash performance.

COMPOSITE CRASH ENERGY ABSORPTION

Existing steel and aluminium vehicle structures absorb energy in a crash due to plastic deformation, work hardening and heat losses. By contrast, composites absorb energy by undergoing fragmentation, which can occur in various different modes. Figure 3 illustrates the difference between the respective progressive deformation in an aluminium (left) and a composite tube (right).

Figure 3: Comparison between plastic folding in metals (left) and fragmentation in composites (right) [5].

Overall there are four principle deformation modes for energy absorbing crash structures [6]:

1. Global buckling
2. Progressive folding
3. Progressive crushing
    a. Progressive splaying and
    b. Progressive fragmentation

The first and second deformation modes are general modes and may occur in any structure undergoing compressive loading including aluminium and steel, where progressive folding is the principle mode of energy absorption. It should be noted that composite structures may also deform in progressive folding.

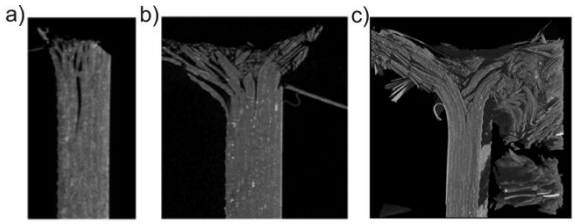

Figure 4a –c): Crushing fragmentation in a composite structure [7].

In addition composite may deform in progressive crushing or fragmentation modes, which tend to exhibit higher specific energy absorption than progressive folding. Figure 4a to 4c show the principle fracture in a composite structure during progressive crushing. In most composite structures the progressive splaying and fragmentation occur simultaneously. Initially, delaminations propagate longitudinally through the structure. The outer plies splay to the inside and outside respectively, while the plies in the middle are fragmented. These deformation modes then propagate through the structure. Energy is mostly dissipated through fragmentation and friction, both between the plies as well as the impactor. Depending on the exact sequence of deformation the amount of energy dissipated through the fracture or friction may change significantly.

To design composite structures for energy absorption the designer needs to be able to control the deformation behaviour of the component by designing the microstructure of the composite component. This is illustrated in Figure 5, where the typical design decisions affecting SEA are shown. Structural design of a metallic structure mostly requires a choice of suitable alloy.

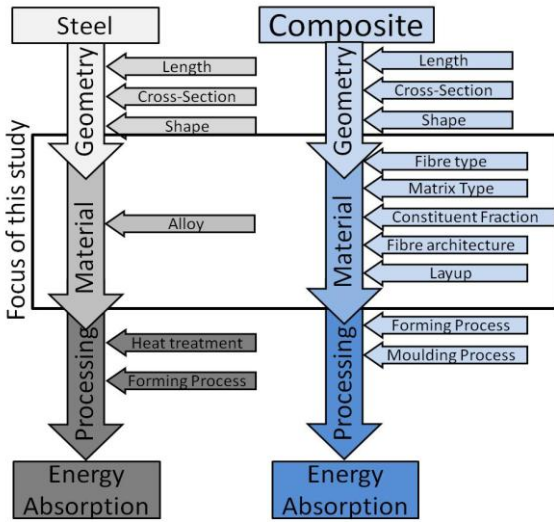

Figure 5: Comparison between typical design decisions affecting the specific energy absorption of a component.

When designing composite structures for energy absorption the designer needs to make informed decisions about the exact material configuration, such as fibre architecture and layup to achieve the desired crash properties. The focus of this work is thus a detailed understanding of the effect of the microstructure on SEA. The following sections will thus aim to illustrate the range of properties that can be achieved with geometrically identical composite specimens having different microstructures.

ENERGY ABSORPTION IN AXIAL AND OBLIQUE IMPACT

Sample Description

Composite specimens were manufactured from openly available carbon fibre for the braiding yarns and BMW proprietary carbon fibre for the axial yarns using triaxial braiding. In triaxial braiding three principle material orientations can be realized for each layer, such as (45, 0, -45). Braiding was chosen here as the principle manufacturing method since is it a highly automated manufacturing process with very low scrap ratios making it suitable for large-scale production. In addition the interlocking of the fibres in braided or woven structures has previously been shown to offer higher SEA than comparable unidirectional (UD) ply configuration [8].
To understand the potential performance benefits of composites specimens the fibre architecture was varied. In a first test the axial fibre fraction was varied between 28% and 60% and the thickness was varied, while the braiding angle was held constant, see Table 1. All specimens had a fibre volume fraction of 50%.

Table 1: Specimen Configurations for axial and oblique impact testing.

Parameter		low	high
UD-Volume fraction	[%]	28	61
Braid layers	[-]	2	4
Aspect ratio	[-]	1:2	1:1.08

Samples were manufactured to a final length of 400mm. The cross-section of the specimens was 140x70mm or 140x130 with a 15mm corner radius measured on the outside, Figure 6. The specimen ends were machined to the final length and then prepared with a chamfer trigger, which was necessary to initiate crushing and reduce the peak load.

Testing

The specimens were tested using a vertical sled configuration, see Figure 7. The specimen was fixed and was impacted by a drop mass. The test speed was 8.2m/s and the mass was varied to achieve a defined test length while not entirely disintegrating the specimen.

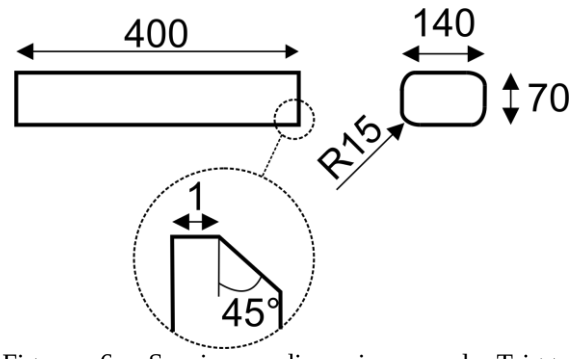

Figure 6: Specimen dimensions and Trigger configuration for an example specimen with a 1:2 Aspect ratio.

For the oblique tests the specimen was affixed identically to axial impact to the load cell and the impactor was canted. The reaction force was recorded using a piezoelectric load cell. An example of the deformation sequence is shown in Figure 8.

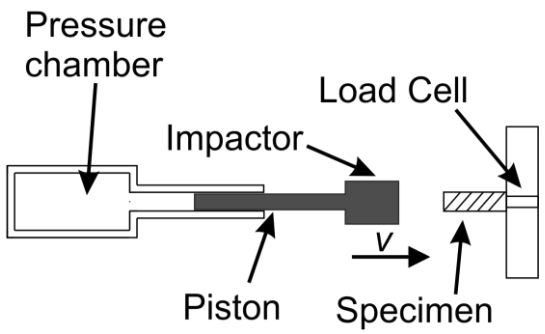

Figure 7: Impact test configurations.

Initially the trigger was destroyed, then the outside plies splayed out while the plies and in the centre and most of the axial fibres were destroyed through fragmentation. This principle sequence of deformation events was the same for all specimens; however some specimen exhibited a strong tendency to splay while others fragmented.

Results

Using the force displacement data the total energy absorbed by the specimens was calculated from Eq. 2

$$E = \int_{s=0}^{s} F(s)ds \qquad (2)$$

with E being the absorbed energy, F the instantaneous force and s the crushed specimen length. The specific energy absorption (SEA) was then calculated by dividing the crushed component mass by the absorbed energy

$$SEA = \frac{El}{ms} \qquad (3)$$

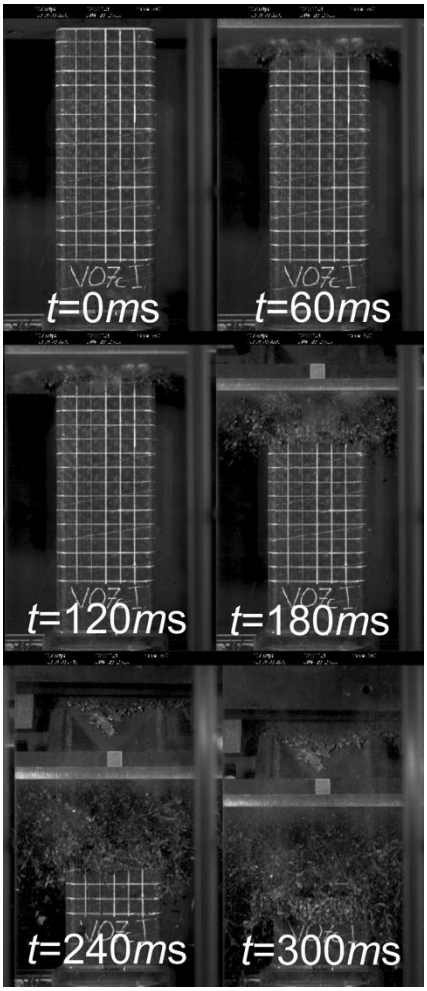

Figure 8: Deformation sequence for specimen V04 during high speed impact testing

with *l* being the initial component length, *m* the component mass and *s* the crushed specimen length. The SEA for the tested specimen configurations is given in Table 2.

Table 2: Calculated SEA data for the axial crush specimens.

Test #	Corner Radius [mm]	UD-Fraction [%]	Braid Layers [-]	Aspect Ratio [-]	SEA [kJ/kg]
V01	15	28	2	1:2	26.2
V02	15	61	2	1:2	29.6
V03	15	28	4	1:2	29.4
V04	15	61	4	1:2	35.8
V05	15	28	2	1:1.08	20.2
V06	15	61	2	1:1.08	24.7
V07	15	28	4	1:1.08	30.8
V08	15	61	4	1:1.08	38.9

When comparing the test results a few trends can be seen. First the energy absorption is always higher for specimens with a higher UD Fraction; the typical increase varies between 13% and 26%. When comparing specimens with identical aspect ratio and UD fraction it can be seen that specimens with a higher number of braid layers, i.e. thickness, have a higher specific energy absorption. Specimen V08 has a 57% higher SEA when compared to specimen V06. Lastly, the aspect ratio can have an impact on SEA, however the trend is less clear. Specimens with two braid layers have a higher SEA with a 1:2 aspect ratio, while specimens with four layers have a higher SEA for a 1:108 aspect ratio. From the variables investigated the specimen thickness has the highest impact on SEA and it is therefore the primary design variable when aiming to improve SEA in composite structures. However, by altering the microstructure of the composite structure, such as the ratio of axial to braid fibres the SEA can be increased by up 26%.
The results for the oblique tests are shown in Table 3, the specimen configurations were identical to Table 2. When comparing the test results to the axial impact data we can see that the SEA at an oblique angle of 10*deg* is actually higher in most cases, than for the same axial test specimens. This effect is more pronounced for the specimens with a 1:2 aspect ratio. At 20*deg* almost all specimens, with the exception of specimen V04 exhibited a lower SEA than for the axial impact case.

Table 3: SEA for oblique testing at 10 and 20 degree.

Test #	10 deg [kJ/kg]	20 deg [kJ/kg]
V01	28.9	24.2
V02	33.4	24.0
V03	28.6	32.3
V04	44.0	37.8
V05	25.8	21.5
V06	26.1	20.4
V07	29.8	29.8
V08	33.6	28.7

As discussed previously energy absorption in composites is amongst other things a function of the friction at the impactor surface and the energy that is dissipated by disintegrating the specimen. It is therefore likely that for small oblique angles, such as 10*deg*, the increase in contact length between the impactor and the specimen may yield higher SEA. For higher oblique angles the composite microstructure may disintegrates differently compensating the additional energy absorption due to friction and resulting in overall reduction of SEA.

HYBRIDISATION

As we have previously seen the energy absorption of composites may be controlled by changing the microstructure of the specimen, such as axial fibre fraction. This section will thus study the impact of

hybrid braiding, i.e. braiding with different fibre types such as glass and carbon, as well as braiding angle on SEA.

Sample Description and Testing

Specimens were again manufactured using triaxial braiding. Specimens were manufactured using both glass and carbon fibre for the axial and braid fibres. In addition the fraction of axial fibres was varied between 0.6 and 0.8 and the angle of the braiding fibres was varied between 45 and 75 degree, see Table 4. For all variations specimens were manufactured using glass fibre for both the axial and braid fibres, using carbon for the axial and braid fibres or using glass for the braid fibres and carbon for the axial fibres.

Table 4: Specimen Configurations for hybridisation testing

Parameter		low	0	high
Axial Fibre Fraction	[%]	60	-	80
Braid Angle	[deg]	45	-	75
Fibre architecture	[-]	Glass	Carbon	Glass/ Carbon

Overall specimen dimensions were identical to previous tests with a 140x70 cross-section, see Figure 6. The test configuration was identical to previous tests as shown in Figure 7. A total of 12 different specimen configurations were tested.

Results

The results for the energy absorption were calculated as previously described and are summarised in Table 5. Glass specimens yielded low SEA values around 20*kJ/kg*, while both carbon and glass/carbon specimens yielded similar SEA values from 49 to 60*kJ/kg*. An interesting aspect is the impact of braiding angle on SEA. When comparing specimen V09 and V10 with 45deg and 75deg braiding angle respectively, the specimen with a higher braiding angle yields higher SEA and a comparable effect can be observed for glass/carbon specimens.
Similar to previous results the SEA mostly increases with increasing axial fibre fraction for carbon axial fibres. However, while the increase was previously up to 26% for an increase between 0.28 and 0.61, increasing the axial fibre fraction from 0.6 to 0.8 yields increases between 8% and 14%. In addition, for the glass fibre specimens, the SEA actually decreased when increasing the amount of axial fibres. While carbon and glass/carbon specimens exhibit similar SEA and important aspect is component cost. Although the composite specimens have a higher SEA, glass may be a more cost effective material due to the fact the cost for the fine 3k carbon braiding yarns is significantly higher.

Table 5: Specific Energy Absorption for glass, carbon and glass/carbon hybrid braiding.

Test	Braid Fibres	Axial Fibres	Braid Angle	Axial Fibre Fraction	SEA
-	-	-	*deg*	*%*	*kj/kg*
V09	Glass	Glass	45	60	23.0
V10	Glass	Glass	75	60	32.6
V11	Glass	Glass	45	80	17.7
V12	Glass	Glass	75	80	22.2
V13	Carbon	Carbon	45	60	50.2
V14	Carbon	Carbon	75	60	54.7
V15	Carbon	Carbon	45	80	57.0
V16	Carbon	Carbon	75	80	53.6
V17	Glass	Carbon	45	60	48.9
V18	Glass	Carbon	75	60	55.3
V19	Glass	Carbon	45	80	55.7
V20	Glass	Carbon	75	80	59.9

Consequently, by replacing carbon braiding-yarns with relatively cheap glass fibre glass/carbon hybrid specimens may exhibit higher cost specific performance. They may thus be a viable option to replace steel and aluminium energy absorbing crash structures due to potential weight savings.

CONCLUSION

To design effective energy absorbing composite structures, both geometric and microstructural features need to be understood. To this end, two sets of studies were introduced here, where the geometry, such as aspect ratio was varied. In addition microstructural features, such as braiding angle, fibre type and UD fraction were varied to study their impact on specific energy absorption. From these tests SEA values from 20 to 60*kJ/kg* could be obtained, illustrating the importance of informed decisions regarding the geometry as well as microstructure of composite energy absorbers. The design drivers for SEA in descending order are:

1. Laminate thickness
2. Fibre type(s)
3. Axial Fibre Fraction
4. Braiding Angle
5. Aspect ratio

However, to harness such potential weight savings requires changes in the vehicle architecture, which in turn may act as multipliers yielding more dramatic weight savings, in return. With new drivetrain architectures, such as hybrids and electric vehicles, innovative vehicle architectures are required and this may both be an opportunity for composite vehicle structures as well novel crash structural concepts utilizing composites. In conclusion, the results indicate that composites may be one way of reducing

the weight of vehicle structures while maintaining or enhancing the current level of passenger safety.

REFERENCES

[1] Barnes G, Coles I, Roberts R, Adams DO, Garner DMJ. *Crash Safety Assurance Strategies for Future Plastic and Composite Intensive Vehicles (PCIVs)*. Cambridge, Massachusetts, USA: Volpe National Transportation Systems Center, 2011.

[2] Anon. *U.S. Departement of Transportation: Federal Motor Vehicle Safety Standards and Regulations* <http://www.nhtsa.gov/cars/rules/import/fmvss/index.html%3E. Accessed 23rd Feburary 2013, 1998.

[3] Anon. *United Nations Economic Comission for Europe: Vehicle Regulations* <http://www.unece.org/trans/main/welcwp29.html%3E. Accessed 23rd February 2013, 1958.

[4] Jacob A. *BMW counts on carbon fibre for its Megacity electric vehicle* <http://www.reinforcedplastics.com/view/11691/bmw-counts-on-carbon-fibre-for-its-megacity-electric-vehicle/%3E. Accessed 23rd Feburary 2013, 2010.

[5] Lukaszewicz DH-JA. *Automotive Composite Structures for Crashworthiness*. Elmarakbi A (ed). (unpublished), 2013.

[6] Hull D. *A unified approach tp progressive crushing of fibre-reinforced composite tubes*. Comp Sci Tech. 1991;40: 377-421.

[7] Johnson AF, David M. *Failure mechanisms in energy-absorbing composite structures*. Philosophical Magazine. 2010: 1-17.

[8] BIsagni C, Di Pietro G, Fraschini L, Terletti D. *Progressive crushing of fiber-reinforced composite structural components of a Formula One racing car*. Comp Struct. 2005;60(4): 391-402.

ENERGY DISSIPATION AND STRUCTURAL INTEGRITY IN FRONTAL IMPACT

Izabella Ferenczi
Dr. Stefan Kerscher
Dr. Frank Möller
BMW Group
Munich, Germany
Paper Number 13-0321

ABSTRACT

Currently, vehicle structures for series production mainly consist of metals. Lightweight structures are becoming increasingly important to ensure vehicles utilizing alternative electric drives are competitive. This is one of the driving forces behind the use of CFRP (Carbon-Fiber-Reinforced Plastics) in vehicle structures at BMW. However, in crash impact events, the material behavior of CFRP in terms of energy dissipation may be different compared to that of ductile materials such as steel. Notwithstanding, the potentially high specific mechanical properties of lightweight materials like CFRP make these appealing for applications in vehicle structures. In order to take advantage of the specific material properties in frontal impact applications a new approach to energy dissipation whilst maintaining structural integrity is required.
The primary objective in passive safety is to ensure the protection of the car occupants, who are enclosed by the passenger compartment. In order to protect the occupants from potential injury in the case of a crash, the passenger compartment must meet highly demanding requirements. To this end, the front structure is divided into separate energy dissipation zones. Each zone has different requirements with regard to residual load capacity and integrity, both of which increase in proportion to the proximity to the occupant cell. This use of effective energy management ensures the structural integrity of the occupant cell is maintained.

STRUCTURAL INTEGRITY

Conventional vehicle structures consisting of metals have a long history of crash design. The requirements for structural integrity are well established and the criteria for fulfilling these are known. As a general rule one does not allow significant rupture in load paths, connections such as spot welds or in the structures of the passenger compartment. This standard ensures a certain degree of robustness in the crashworthiness of a vehicle. Vehicles made of lightweight materials such as CFRP are no new innovation. There is a long history of using CFRP for racing cars or in low volume super sports cars, see also [1]. In contrast to normal series production these vehicles have different requirements for passive safety and are not generally tested by consumer protection authorities. CFRP currently used in series productions is usually limited to individual parts of the vehicle such as the roof panels. The large scale use of CFRP in crash relevant vehicle structures (main load paths, passenger compartment) demands a new approach for structural integrity. The requirement of minimizing significant damage as used in metals is no longer suitable, since energy dissipation involves splintering in CFRP structures in contrast to plastic deformation of steel structures.
Our goal is a crash design which exploits the advantages of CFRP and other lightweight materials in order to maintain or even improve the crashworthiness compared to conventional vehicles. The goal is achieved by clear definition of the structural behavior dependant on the crash zone and material/geometry used.

BMW i3

The classification of the crash zones will be illustrated using the example of the i3, BMWs electric mega-city vehicle. The general vehicle concept is based on a horizontal-split variant of a Life/Drive-architecture:

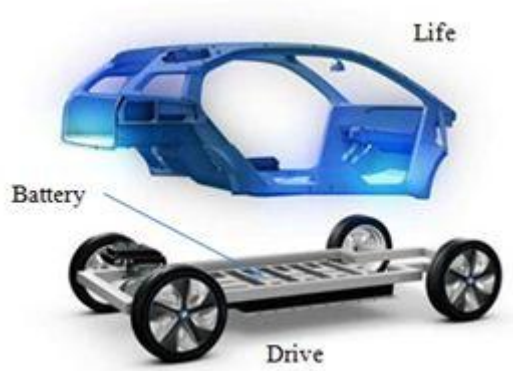

Figure 1: Life/Drive concept BMW i3

The battery is enclosed by the aluminum Drive structure with the advantages of a low center of mass, balanced weight distribution and ideal protection against external impact. This space-efficient storage in the under floor section has also the advantage of significantly more interior space than other vehicles with the same wheelbase due to omission of a centre tunnel. The front and rear structures are part of the 'Drive' module and as such made of aluminum. The 'Life' cell (passenger compartment) is a CFRP-shell construction which is mounted and affixed on top of the 'Drive' module. In case of frontal or rear impact the main part of the energy absorption is completed

by crash active aluminum structures. The principal function of the 'Life' cell is passenger protection. In case of side impact the cell (especially the CFRP-rocker panel and roof rail) plays a decisive role in energy absorption and provides an optimal protection against intrusion.

DEFINITIONS

The requirements for structural integrity depend on the actual material used, the respective energy dissipation zone and the geometry. In order to specify these, it is necessary to provide the following definitions:

1. **Structures**:
    - **a. Membranes** are parts, formed by bent surfaces, whose thickness is small compared to their other dimensions. Examples are the roof, floor panel, bulkhead, …
    - b. **Profiles** are parts with a significant length/width-ratio. Examples are the rocker panel, roof rail, A-, B-… pillars, engine support beams…
2. **Materials**:
    - **a. Ductile metals** are materials with high fracture toughness and show a ductile rupture pattern. Examples are cold worked steel panels, extruded aluminum profiles, …
    - **b. Castings** are materials with low fracture toughness and show a brittle damage pattern. Examples are aluminum die-castings, sand castings, magnesium-castings…
    - **c. CFRP** is carbon-fiber-reinforced plastic
    - **d. Composite design:** CFRP combined with metals.

ENERGY DISSIPATION ZONES

The description of the energy dissipation zones is illustrated for the front part of the vehicle including the A-pillar. An equivalent classification of energy dissipation zones is also defined for the rear and side parts of the vehicle.

Zone 1: Front-End – Bumper and Crash Boxes.

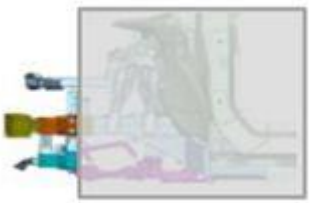

Figure 2: Crash Zone 1

In zone 1 plastic deformation is allowed. Separation or damage of the bumper cross beam or the crash boxes is acceptable as long as function and continuous energy absorption is maintained by the following structures.

Zone 2: Longitudinal Beams to Suspension Turret Inclusive Subframe Front Area.

Figure 3: Crash Zone 2

In zone 2 plastic deformation and damage within deformed components acceptable. Separation or damage of the load paths is to be minimized. The first front subframe connection to the longitudinal beams and the front branch of the suspension turret may separate to enable more deformation in the main load path and therefore increase energy absorption.

Zone 3: Longitudinal Beams between Bulkhead and Suspension Turret Inclusive Subframe Rear Area

Figure 4: Crash Zone 3

In zone 3 plastic deformation and damage within deformed components acceptable. Separation or damage of the load paths is to be minimized. Separation of the different load paths (front subframe to longitudinal beams, suspension turret to longitudinal beam) is to be minimized. This enables protection of the 'Life' cell.

Zone 4: 'Life' Cell – Bulkhead, Side frame

Figure 5: Crash Zone 4

In zone 4 deformations are allowed. Significant damage is to be minimized. The detailed description of acceptable crash-behavior in this zone is enclosed in the next section.

MATERIAL BEHAVIOR

As mentioned before the criteria for structural integrity depend on

- Energy dissipation zone (1-4)
- Material (metals, castings, CFRP)
- Geometry (membranes, profiles)

Since the front part of the BMW i3 mainly consists of aluminum structures and the requirements for structural integrity for metallic structures are well known, the following explanations focus on the passenger compartment which mainly consists of CFRP structures. The requirements for structural integrity in zone 4 (passenger compartment) are the same for frontal, side and rear impact.

Structural integrity after crash is given for…

….profiles made of CFRP located in a crash zone where damage is minimized (zone 4) and/or a certain load bearing capacity is maintained for example by ensuring that several fiber layers remain intact.

…membranes made of CFRP as part of the Life cell (bulkhead, floor panel, roof...) if damage is minimized and/or splintering can be controlled (e.g. fiber layers in different directions).

…connection of membranes and profiles made of CFRP (for example floor/rocker panel) if damage to the connection (adhesive, rivet…) is minimized or is bridged by another (intact) structure.

While splintering in CFRP structures is acceptable, significant rupture in metallic structures (profiles and membranes) located in zone 4 should be minimized. The reason for this difference is that, in contrast to structures made of CFRP (as shown in the next section "test results"), rupture in metallic structures is difficult to control and metallic structures have little load bearing capacity once significant rupture occurs.

In spite of the occurrence of damage for example in the bulkhead (in case of frontal impact) or the side frame (in case of side impact) the intrusion level of a passenger compartment made of CFRP is comparable to that of similar conventional vehicles (i.e. size and mass) made of steel. As figures 6 and 7 show, the intrusion after frontal impact as well as after side impact (oblique pole) are in similar ranges.

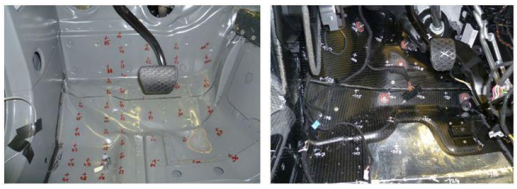

Figure 6: foot well after frontal impact steel vs. CFRP

Figure 7: passenger compartment after side impact steel vs. CFRP

The main difficulty when judging damage and splintering in CFRP structures is the determination of the degree of damage (i.e. are all fiber layers affected or are there still intact fiber layers). Usually one cannot determine this by a simple sight check. One possibility for checking such undetermined damage is CT-scanning. This was done for example for typical damage and splintering in the bulkhead (see figure 8) after frontal impact.

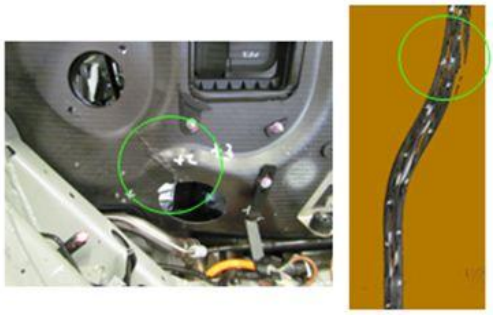

Figure 8: CT-scan of splintering in bulkhead after frontal impact

The results of the CT-scanning show that permitted splintering in this area is not significant, i.e. many fiber layers are still intact. The resulting documentation for characteristic damage modes in different laminate layups can be used as an assessment catalogue for further visual inspections.

TEST RESULTS

Splintering can be accepted in CFRP structures due to the fact that CFRP structures maintain load bearing capacity even after damage occurs, the fiber layer structure of membrane elements provides a natural crack arrestor. Several test results confirm these assumptions, as shown in this section:

Regarding frontal impact, see also [2], the same test was executed with an increased load on the bulkhead. Although permitted splintering occurred in case of the lower impact, the damage was only lightly increased in case of the higher impact (see figure 9). The requirements for dynamic and static intrusion where fulfilled in both cases.

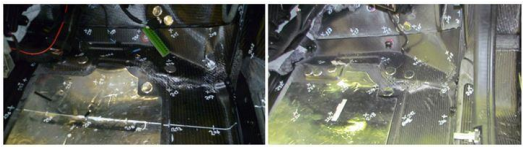

Figure 9: foot well after frontal impact in CFRP Life-Cell with lower (left) vs. higher (right) load impact

For side impact component tests showed similar results:

The experimental setup is a dynamic 5 point bending test with CFRP crash structures (roof rail and rocker panel) which approximates the impact of a FMVSS214 oblique pole test, see also [3].

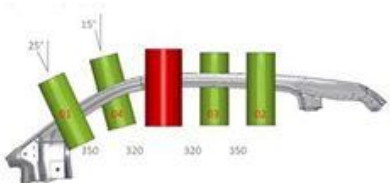

Figure 10: Component test setup roof rail

The test was repeated with the same, now partially damaged, structure. The set up, thus the load impact (mass and velocity of impactor) was equal to the first test. Although the characteristic of the damage in the CFRP structures corresponded to the damage after a FMVSS214 oblique pole test, the structures were able to absorb the same energy a second time (as shown in figures 11 and 12). Even the load level was nearly the same. In case of metal structures one would expect a considerable drop off of the force level if a significant rupture occurs.

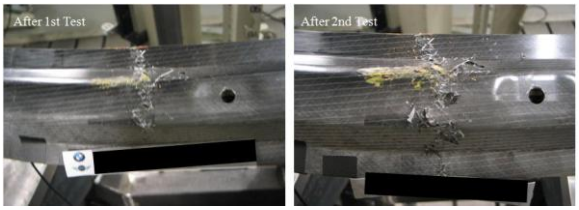

Figure 11: roof panel after 1st (left) and 2nd (right) impact

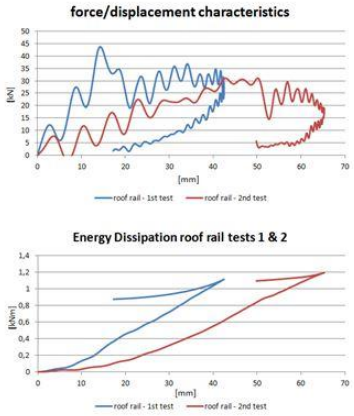

Figure 12: Force/Displacement characteristics of both roof rail tests

CONCLUSIONS

CFRP structures require different evaluation criteria when compared to structures made of ductile metals. The reason is, that metal structures may collapse if the load continues after significant rupture occurs whereas CFRP structures have ongoing load bearing capacity even after significant splintering occurs. Furthermore, CFRP structures show different performance regarding crack propagation. The fiber layer structure provides a natural crack arrestor as shown with the help of CT-scans.

This paper provides a basis for the definition and interpretation of future vehicle architectures and the use of lightweight materials with non-ductile material behavior in crash structures.

CFRP is a suitable material for crash applications, due to the high specific mechanical properties. State of the Art crashworthiness requirements in terms of structural integrity can also be fulfilled.

REFERENCES

[1] Barnes G, Coles I, Roberts R, Adams DO, Garner DMJ. Crash Safety Assurance Strategies for Future Plastic and Composite Intensive Vehicles (PCIVs). Cambridge, Massachusetts, USA: Volpe National Transportation Systems Center, 2011.

[2] U.S. Department of Transportation National Highway Traffic Safety Administration, Laboratory Test Procedure for FMVSS 208, Occupant Crash Protection, TP208-14, April 2008.

[3] U.S. Department of Transportation National Highway Traffic Safety Administration, Laboratory Test Procedure for FMVSS No. 214, Dynamic Side Impact Protection – Rigid Pole Side Impact Test Requirenments- TP-214P-01, September 2012.

ASSESSMENT OF AN OBLIQUE MOVING DEFORMABLE BARRIER TEST PROCEDURE

James Saunders
Dan Parent
National Highway Traffic Safety Administration (NHTSA)
USA
Paper Number: 13-0402

ABSTRACT

In September 2009 the National Highway Traffic Safety Administration (NHTSA) published a report that investigated the incidence of fatalities to belted non-ejected occupants in frontal crashes involving late-model vehicles. The report concluded that after exceedingly severe crashes, the largest number of fatalities occurred in crashes involving poor structural engagement between the vehicle and its collision partner, such as corner impacts, oblique crashes, or impacts with narrow objects.

In response to these findings, NHTSA began researching a test procedure intended to mitigate the risk of injuries and fatalities related to motor vehicle crashes involving poor structural engagement. This research demonstrated that an offset impact between a "research" moving deformable barrier (RMDB) and a stationary vehicle at a 15 degree angle can reproduce vehicle crush, occupant kinematics, and risk of injury seen in vehicle-to-vehicle crashes. It was also demonstrated that injury risk related to poor structural engagement has not been entirely mitigated in the current fleet, as newly-designed vehicles are still prone to large intrusions and potential injuries to the head, chest, knee/thigh/hip, and lower extremity.

The current study adds additional oblique RMDB-to-vehicle crash tests with high sales volumes vehicles in order to capture a larger portion of the current and future fleet for further analysis. These additional tests bolster the utility of the existing database of oblique RMDB-to-vehicle crash tests with a THOR 50th percentile male occupant in the driver's seat.

INTRODUCTION

Saunders et al, 2012 [1] performed paired vehicle test in both "Small Overlap Impact" (SOI) and "Offset Oblique" (Oblique) test procedures with vehicles that were redesigned or introduced in 2010 and 2011. Most of these vehicles received the highest ratings in current US consumer rating systems. Saunders et al, 2012 [1] demonstrated that even though these vehicles had good ratings in consumer information crash tests and were newly designed, there still exists potential for vehicle design improvements that could mitigate real-world injuries and fatalities in both of these crash types. When comparing the average injury assessment values (IAVs) for each body region in each of the two procedures, similar trends appeared in both the SOI and Oblique test modes, which mirrored the real-world data, including the risk of knee-thigh-hip, lower extremity, head, and chest injuries. There were, however, some differences in IAVs between the SOI and the Oblique modes; head and chest IAVs were slightly higher in Oblique, while knee-thigh-hip IAVs were higher in SOI. Rudd et al. 2011 [4] also found similar findings when they reviewed Oblique and SOI vehicle crashes included in the Crash Injury Research and Engineering Network (CIREN) and National Automotive Sampling System Crashworthiness Data System (NASS-CDS) databases.

Saunders et al, 2013 [2] demonstrated that the repeatability of the two test procedures were similar to existing vehicle tests in the full frontal and offset deformable barrier crash test conditions.

To help support NHTSA's decision on its small overlap/oblique program, this paper adds addition high sales volume vehicles to the previous study in order to capture the safety performance of a larger portion of the current and future fleet. In additional to the previous left-side Oblique test configuration, this paper presents Oblique impacts to the right side of the vehicle and evaluates the kinematics of an

occupant positioned on the non-struck side of the vehicle.

METHODOLOGY

Oblique Crash Testing

Figure 1 shows the left side impact (LSI) Oblique test procedure setup. In this setup, the RMDB impacts the target vehicle at 90 kph (56 mph) and the stationary vehicle is positioned such that the angle between the RMDB and the vehicle is 15 degrees and the overlap is 35 percent on the driver side of the vehicle.

The vehicle was instrumented with a rear accelerometer to record the X and Y accelerations of the vehicle. Between test series some of the procedures for measuring intrusions were modified, therefore the following list gives the general locations of the intrusions measured for each test.

1. A 4 by 5 matrix of points on the toepan/floorboard (Figure 2). The location with the maximum X intrusion is used for analysis in this paper.
2. Left and right instrument panel (Figure 2)
3. Steering wheel (Figure 2),
4. Bottom A-pillar (B A-pillar) (Figure 3)
5. Rocker panel (Figure 3)

Table 1 shows the list of vehicles tested in LSIs and Table 2 shows the list of vehicles that were tested in right side impacts (RSI). Throughout this paper, the LSI conditions are referenced by the vehicle name itself, and the RSI conditions are referenced by the vehicle name followed by an "R" to indicate the right-side impact.

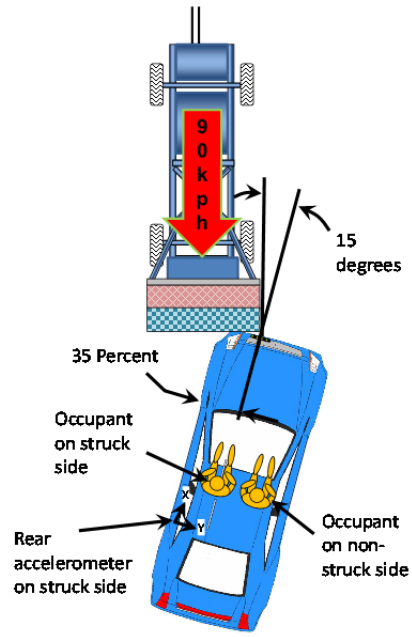

Figure 1: Test setup for LSI

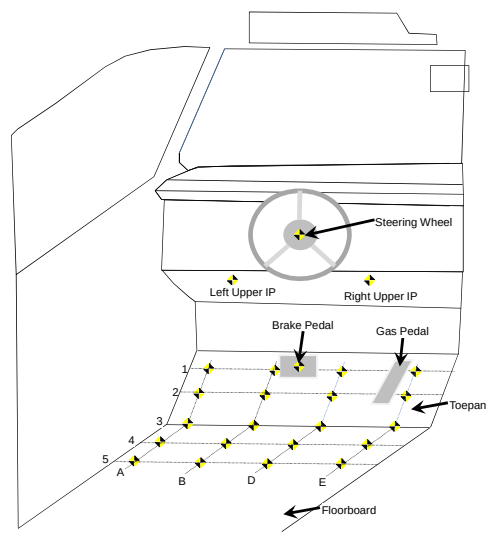

Figure 2: Interior intrusion measurements

Figure 3: Location of B A-pillar and rocker panel intrusion points

Table 1: LSI matrix and naming convention of each vehicle

NHTSA TEST NUMBER	MAKE	MODEL	YEAR	TEST WEIGHT (KG)
7458	Smart	Fortwo	2011	1034
7441	Toyota	Yaris	2011	1331
7428	Ford	Fiesta	2011	1371
8084*	Nissan	Versa	2013	1451
8089*	Hyundai	Elantra	2013	1590
7431	Chevrolet	Cruze	2011	1662
8088*	Toyota	Camry	2012	1759
7467	Buick	LaCrosse	2011	1944
8087*	Ford	Taurus	2013	2123
8097*	Honda	Odyssey	2012	2210
8096*	Honda	CRV	2012	1757
7476	Ford	Explorer	2011	2363
7457	Dodge	RAM1500	2011	2611
8099*	Chevrolet	Silverado	2012	2624

* THOR positioned in both driver and right front seating position

Table 2: RSI matrix and naming convention of each vehicle

NHTSA TEST NUMBER	MAKE	MODEL	NAME	TEST WEIGHT (KG)
8086*	Nissan	VersaR	2013	1438
8085*	Toyota	CamryR	2012	1752

* THOR positioned in both driver and right front seating position

Occupant Response Assessment

Previous Oblique RMDB crash tests included an anthropomorphic test device (ATD) seated in the driver (near-side) position. This ATD was a 50th percentile male Test Device for Human Occupant Restraint (THOR) which met the specifications of the Mod Kit [5]. For the most recent 7 of the LSI tests included in this study, a second THOR was seated in the right front passenger seat (far-side) (Table 1). The far-side THOR met the specifications of the Mod Kit, with the addition of a shoulder assembly intended to improve anthropometry and biomechanical response of the shoulder-torso complex. This shoulder assembly, known as the "SD-3," is a derivation of the Chalmers shoulder [6] which was further developed through the European Union's THORAX project [7]. Since only one SD-3 shoulder assembly was available at the time of these tests, it was installed on the far-side THOR to investigate the interaction with the shoulder belt when the occupant is moving laterally away from the belt, while minimizing the risk of damage due to direct contact with the door which would be more likely on the near-side.

For the RSI tests, the ATDs positions were reversed such that the THOR with the SD-3 shoulder was in the driver (now far-side) position and the THOR with the standard shoulder was in the passenger (now near-side) position. In both the LSI and the RSI conditions, each ATD was positioned according to the Federal Motor Vehicle Safety Standard (FMVSS) No. 208 seating procedure.

Figure 4. Position of two THOR ATDs in the driver and front passenger position.

RESULTS

Vehicle Response

In general, the total velocity change (delta-V (DV)) in the X-direction decreases as the weight of the vehicle increases for both LSI and RSI (Figure 5). One exception to this general trend occurs with the Versa, where the RSI condition fits the general trend but the LSI condition shows a lower-than-predicted X-direction DV and a higher-than-predicted Y-direction DV. There is no general trend in Y-direction DV for either LSI or RSI.

Except for the ForTwo and the Versa, the toepan intrusion in the X-direction was between 100 mm and 150 mm (Figure 6). The maximum IP intrusion decreased as weight increased, except for the Taurus. The A-pillar intrusions were all below 50 mm, except for the ForTwo, the Fiesta, and the Versa. Only the ForTwo had a Rocker Panel intrusion higher than 50

mm. Toepan intrusions seemed consistent for all vehicles, while the IP intrusion tended to be higher for the lightest vehicles. All steering wheel (SW) intrusion in the X-direction were below 60 mm except for the ForTwo, the Versa, and the Ram1500 (Figure 7). The Yaris, the Versa, the Cruze, and the Camry SW intrusions in the Z-direction were higher than 50 mm.

Figure 8 shows the X-direction intrusions for VersaR and CamryR. VersaR had over 200 mm intrusion for B A-pillar and Rocker Panel.

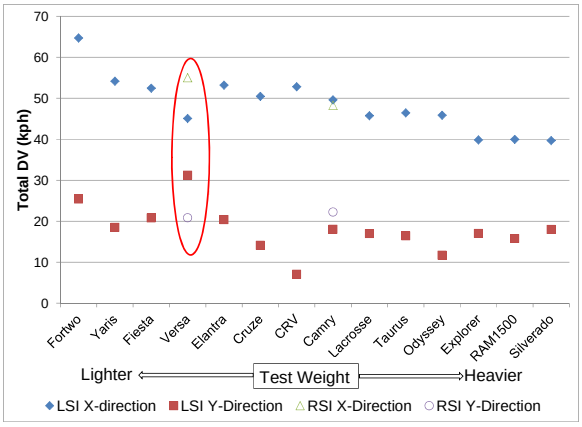

Figure 5: Total DV for LSI and RSI

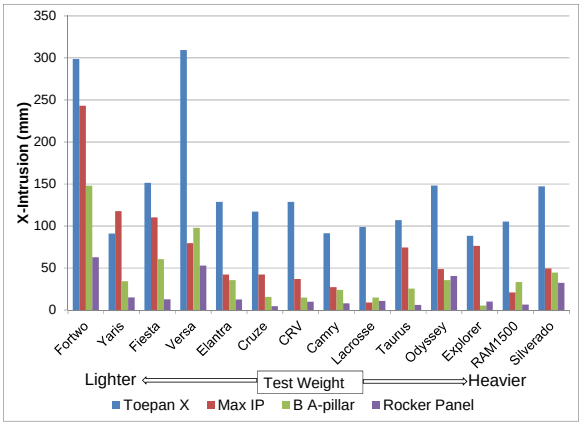

Figure 6: Intrusions for LSI

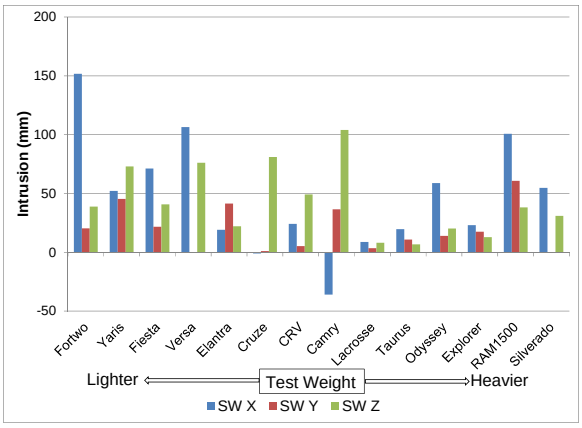

Figure 7: SW intrusions for LSI

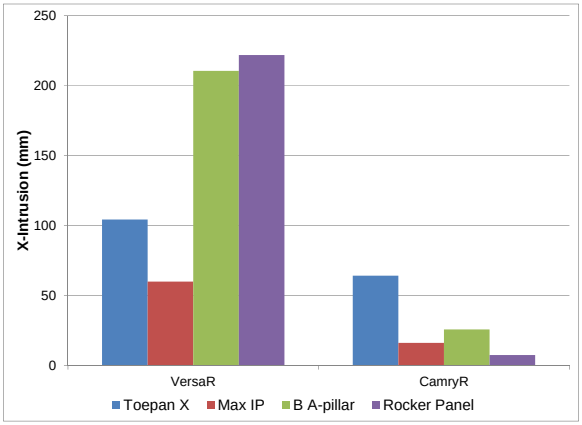

Figure 8: Intrusions for RSI

Occupant Response

<u>Restraint Deployment</u>

In all nine vehicle crash tests carried out, the occupant restraint systems deployed frontal air bags and safety belt pretensioners for both the driver and the right front passenger. In all but one case (LSI condition for the Taurus), a side curtain air bag was deployed on the near-side impact location. Note that the side curtain air bag on the far-side impact location was disabled to allow improved high-speed video visibility, since the principal direction of force would direct the far-side occupant away from this curtain air bag.

Frontal air bag deployment time varied across vehicles, but deployed no later than 28 milliseconds after barrier contact with the bumper of the target vehicle. Safety belt pretensioners triggered before or at the same time as the frontal air bag deployment, no

later than 20 milliseconds after impact, and triggered at the same time for both the driver and right front passenger. The side curtain air bags generally deployed later than the frontal air bags, except for the Camry and the Silverado, which deployed both frontal and side curtain air bags simultaneously. Restraint deployment times and head contact locations are summarized in the Appendix (Table 3).

Lap belt loads varied with no apparent relationship to vehicle mass or DV in both the near-side and far-side occupant locations. For the near-side (Figure 9), the lightest vehicle had the lowest peak lap belt load while the second-lightest vehicle had the highest peak lap belt load, while other tests were clustered around the mean (μ = 3590 N, σ = 1860 N). For the far-side (Figure 10), there was a large range and dispersion of peak lap belt forces (μ = 5870 N, σ = 1850 N).

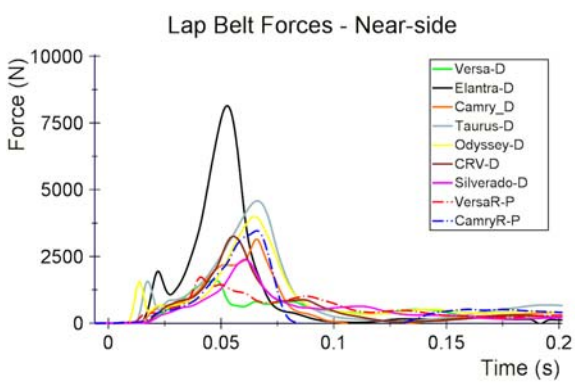

Figure 9. Lap belt forces in the near-side occupant location.

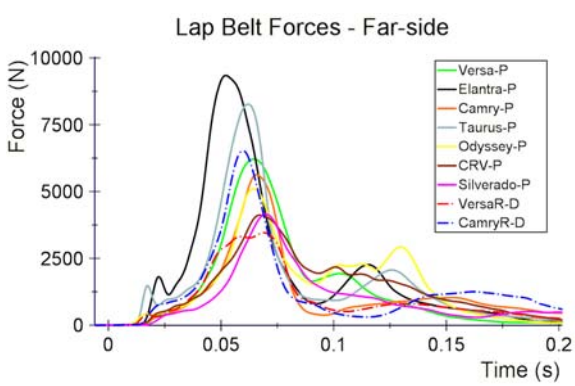

Figure 10. Lap belt forces in the far-side occupant location.

Peak shoulder belt loads were more consistent for both the near-side (Figure 11; μ = 4160 N, σ = 730 N) and the far-side (Figure 12; μ = 4030 N, σ = 920 N) occupant locations, though the shoulder belt load cell for the near-side occupant failed in two tests. In the far-side shoulder belt force time-histories, there are several abrupt drops in the force shortly after the time of peak load, the most obvious occurring in the Taurus between 65 and 70 milliseconds and in the Versa between 50 and 55 milliseconds. These times may correspond to the time that the shoulder belt loses engagement with the shoulder and slides laterally away from the torso.

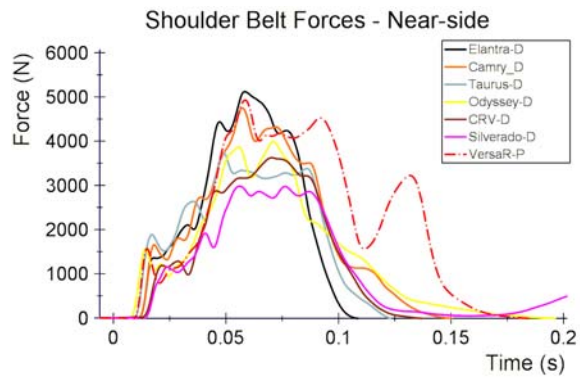

Figure 11. Shoulder belt forces in the near-side occupant location.

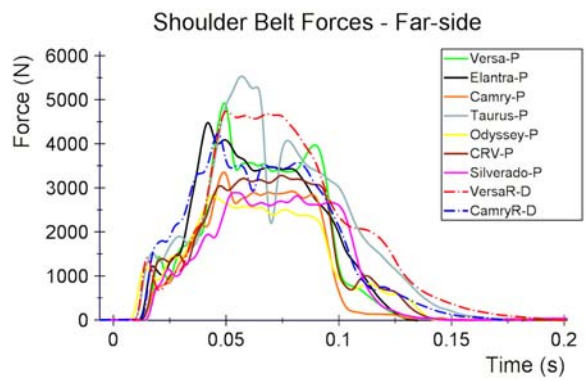

Figure 12. Shoulder belt forces in the far-side occupant location.

Near-side Occupant Kinematics

In the LSI condition, the occupant in the driver's seat begins moving directly forward with a gradually-increasing outboard translation. The head contacts the center or left-center of the frontal air bag with a laterally outboard velocity and is deflected towards the side curtain air bag. Contact with the side curtain air bag was generally minor and focused on the left side of the head, and in one condition (Silverado) the head only contacted the side curtain air bag on

rebound. The head then translates into the gap between the frontal air bag and the side curtain air bag and contacts the door panel. Though, in most cases it was a glancing blow that did not impart much acceleration on the head.

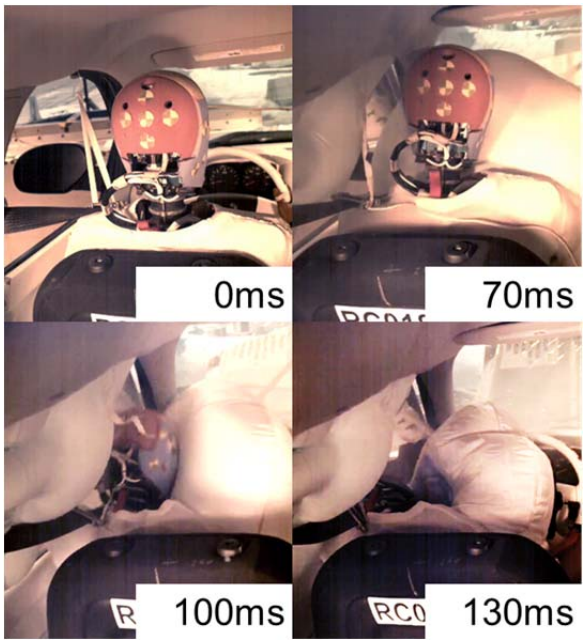

Figure 13. Near-side occupant head kinematics in the LSI Silverado test.

In the RSI condition, the occupant kinematics were essentially a mirror-image of the kinematics in the LSI condition. The occupant moved forward and to the right, the head glanced off the frontal airbag to the right and moved into the gap between the frontal and side curtain air bags. In the Versa, the occupant contacted the door frame at the window sill (Figure 14), while in the Camry, the occupant showed initial upward motion that resulted in contact with the roof (Figure 15). This initial upward motion appears to be the result of a nose-down pitch of the vehicle body during the initial interaction with the RMDB.

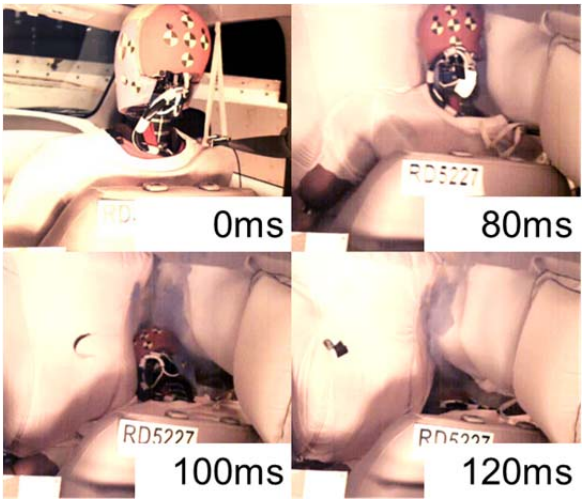

Figure 14. Head kinematics of the near-side occupant in VersaR. The head slides between the gap in the frontal and side curtain air bags and contacts the door frame.

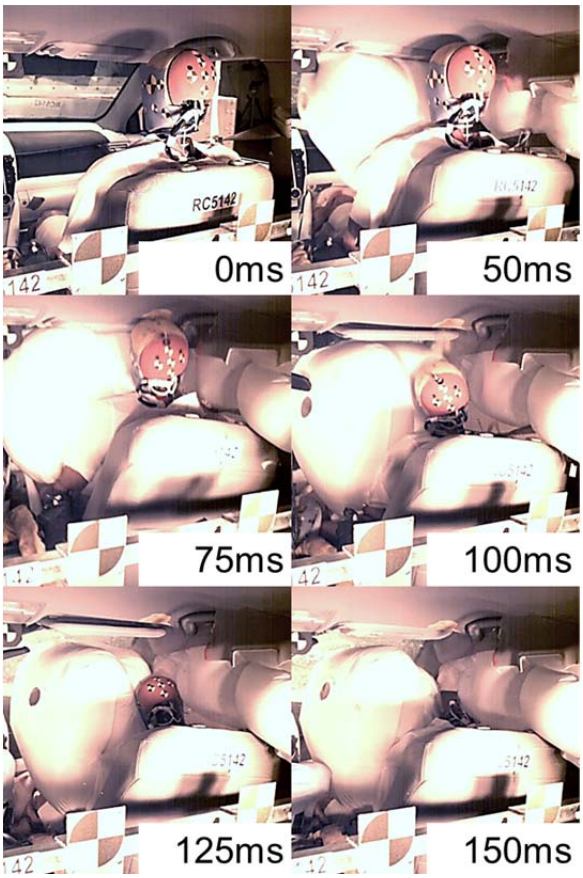

Figure 15. Head kinematics of the near-side occupant in the CamryR test. The head initially translates upward and contacts roof at 75 ms, then continues to travel forward and outboard between frontal air bag and side curtain air bag.

Far-side Occupant Kinematics

In the LSI condition, the far-side occupant is seated in the right front passenger seat. Like the near-side occupant location, the ATD begins moving forward with an increasing left lateral trajectory. In all of the LSI vehicles, the frontal air bag is fully inflated by the time of head contact. Though, unlike the near-side location where the bag is initially closer to the occupant, the head of the far-side occupant always contacts left-of-center on the frontal air bag (Figure 16). Friction between the head and the air bag results in positive rotation of the head about its local Z-axis. In most cases the head then contacts the center IP, either through the bag or directly leaving a paint transfer. Two exceptions to this behavior were the Taurus, where the head remained in contact with the frontal air bag for the duration of the crash event, and the Silverado, where the far-side occupant translated far enough laterally to contact the steering column-mounted gear shift lever. In all of the LSI conditions, the torso of the occupant translates laterally away from the shoulder belt and the belt loses engagement with the shoulder at around 100 milliseconds after the impact.

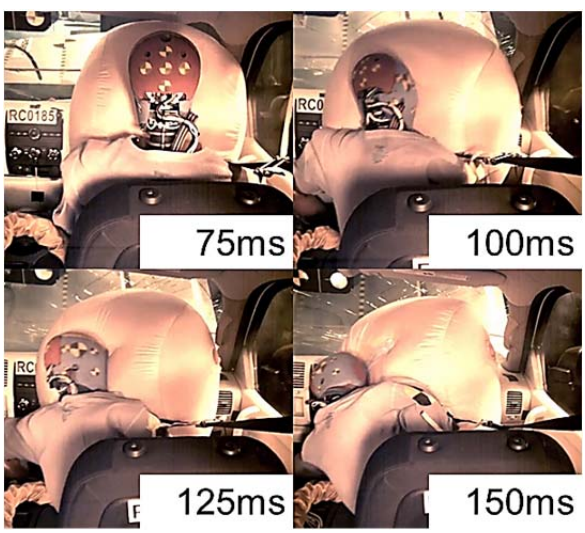

Figure 16. Typical kinematics of the far-side occupant in the LSI condition (Silverado in this case).

In the RSI condition, the kinematics were a mirror-image of the LSI condition with a few exceptions related to the differences in driver-side and passenger-side restraints. The frontal air bag on the driver side is initially closer to the occupant, so head contact occurs with the center of the air bag before lateral translation begins. Though, similar to the far-side occupant in the LSI condition, friction between the RSI far-side occupant's head and the driver-side air bag results in head rotation away from the principle direction of force (PDOF) about its local Z-axis. Since the THOR is positioned with its hands on the steering wheel, similar to the positioning of a Hybrid III in the FMVSS No. 208 seating procedure, , the arm ends up between the head and the center IP at the point of peak head excursion. For both of the RSI tests, the head of the far-side occupant contacts the right forearm which is in contact with the center IP at the point of peak excursion (Figure 17). Like the LSI condition, the torso of the far-side occupant in the RSI condition translated away from the shoulder belt, losing engagement with the shoulder at around 100 milliseconds after the impact.

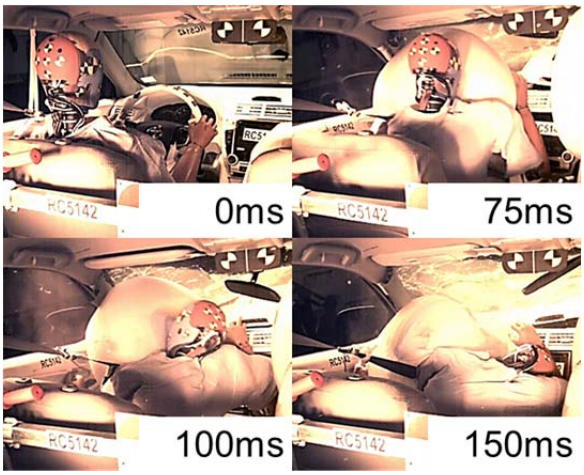

Figure 17. Typical kinematics of the far-side occupant in the RSI condition (CamryR in this case).

Occupant Injury Assessment

A set of IAV metrics were selected based on the available measurements and the existence of preliminary injury assessment reference values (IARVs) for the THOR ATD. IAVs are calculated for each test, whereas IARVs refer to tolerance values, usually tied to a given probability of a certain injury, used to assess the relative severity of the occupant response. As an overall assessment, the metrics that suggest the highest probability of injury include the kinematic brain injury criterion (BRIC),

acetabulum resultant force, tibia index, and ankle rotation. These metrics show good agreement with the field injury exposure presented by Rudd et al 2011 [4], where the body regions with the highest incidence of injury were the knee/thigh/hip, chest, lower extremity, and head. Summaries of the IAVs calculated for the near-side (Table 4) and far-side (Table 5) occupants are included in the Appendix, while this section will focus on the head, chest, knee/thigh/hip, and lower extremity. This section will describe the response of occupants in both the driver seat (near-side occupant in LSI and far-side occupant in RSI) and the right front passenger seat (far-side occupant in LSI and near-side occupant in RSI).

Head

Four out of the eighteen sets of occupant IAVs exceeded the provisional IARV for the 15 ms head injury criteria (HIC15) (Figure 18). All four of these instances coincide with the time of contact of the head to either the door panel (for near-side occupants) or the center IP (for far-side occupants). The head acceleration in the near-side impacts was equally high in the local X- and Y- directions, suggesting a 45 degree effective angle of contact with the door panel. The head acceleration in the far-side impacts was primarily oriented in the positive Y-direction, since the head in both of these cases was rotated 90 degrees to the right and the left side of the head impacted the center IP. There are no apparent trends of HIC15 with vehicle mass, LSI vs. RSI, or near-side vs. far-side.

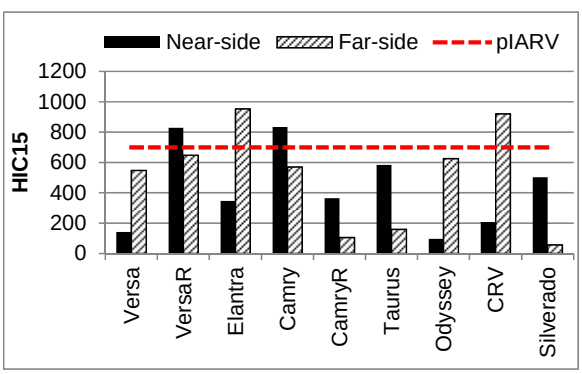

Figure 18. HIC15 head injury metric for LSI and RSI tests.

The BRIC injury assessment metric was calculated using the method and critical values described in Saunders et al, 2012 [1]. The BRIC metric considers the angular velocity and angular acceleration of the head (Eqn 1), as measured by angular rate sensors installed in the head of the THOR ATD. Five out of the nine near-side occupants exceeded the provisional IARV for BRIC of 0.89 (Figure 19), which corresponds to a 30% risk of AIS 3+ traumatic brain injury [8]. One of the highest BRIC values occurred in the Taurus for the near-side occupant, where there was not a side curtain air bag present. While there was a spike in angular acceleration upon contact with the door frame, the primary factor in exceeding the BRIC provisional IARV was the local head X- and Z-direction angular velocity imparted to the head after contact with the frontal air bag.

$$BRIC = \frac{\omega_{max}}{\omega_{cr}} + \frac{\alpha_{max}}{\alpha_{cr}} \qquad (1)$$

In all nine of the far-side cases, the calculated BRIC was higher than the provisional IARV (Figure 19). In each test, head contact with the frontal air bag imparted an outboard rotational velocity on the head about its local Z-axis. Angular velocity was the driving factor in the BRIC metric, as four out of the nine far-side occupants would have exceeded the BRIC provisional IARV based on the angular velocity component alone. On the other hand, none of the near-side or far-side responses would have exceeded the BRIC provisional IARV based on the angular acceleration component alone.

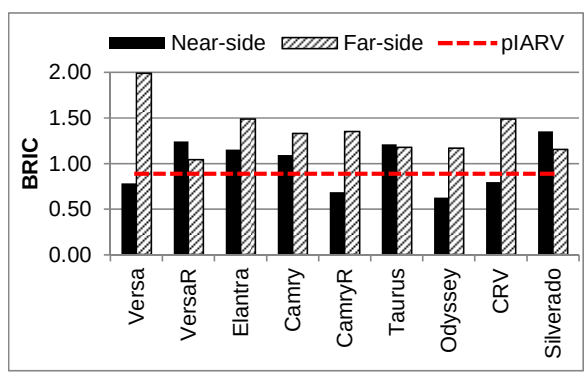

Figure 19. BRIC rotational head injury metric for LSI and RSI tests.

It is worth noting that since the head angular velocity is the driving factor in the BRIC calculation, the

timing of the HIC and BRIC IAVs are not coincident. As an example, consider the near-side (right front passenger seat) occupant in the CamryR test (Figure 20). The head linear acceleration results in a HIC_{15} window of between 59 and 72 milliseconds. While there is an increase in head angular velocity in this same time window, the peak angular velocity does not occur until 130 milliseconds.

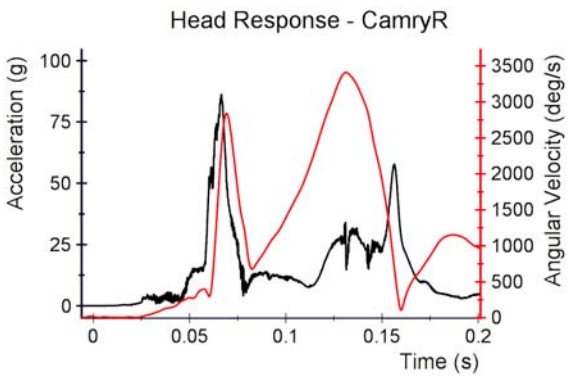

Figure 20. Near-side head resultant linear acceleration (black) and angular velocity (red) in CamryR.

Chest

Chest deflections presented in Figure 21 represent the maximum deflection at any of the four chest quadrants measured by the THOR ATD at any point in time. This deflection is calculated as the peak change in length of the vector between the attachment point of the thoracic deflection instrumentation on the anterior rib cage and the anchor point on the local spine segment. In all but one of the tests in this series (Versa LSI), chest deflection was higher for the near-side occupant than for the far-side occupant.

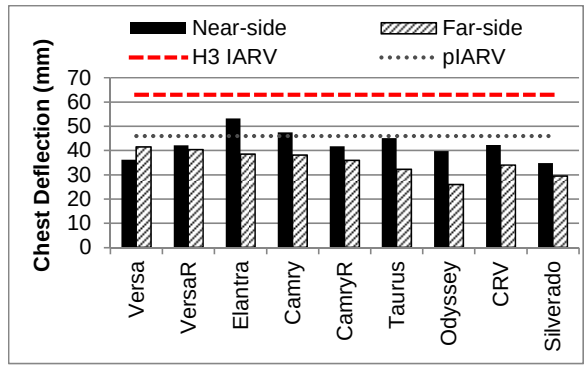

Figure 21. Peak chest deflection for LSI and RSI tests.

The relationship between injury risk and chest deflection as measured by the THOR ATD has not yet been developed. Figure 21 shows the existing IARV for the Hybrid III 50th percentile male (63 millimeters) as well as a provisional IARV (46 millimeters). This provisional THOR IARV was selected based on a limited series of PMHS tests which measured the three-dimensional rib deflections at the same locations as the THOR ATD. In these PMHS tests, the average deflection of the lower measurement location on the same side as the belt (which was the peak deflection location in a majority of the near-side occupants in the LSI and RSI tests) was 45.8 millimeters, which resulted in at least 2 and as many as 27 rib fractures [9]. Research is currently underway to further develop the injury risk functions and associated IARVs for rib deflection measured by the THOR ATD.

Knee/thigh/hip

While the loads measured by the distal femur and acetabulum are intrinsically related due to the shared load path, some divergent trends were observed. While none of the tests in this series exceeded the provisional femur compressive force IARV (Figure 23), eight of the tests exceed the provisional IARV for resultant acetabulum load (Figure 22). Femur loads were highest for the near-side occupant in all but one of the vehicles, while acetabulum loads were higher for the near-side occupant in only five of the nine vehicles. The highest acetabulum loads were recorded in the lightest (Versa) and the two heaviest (CRV, Silverado) vehicles.

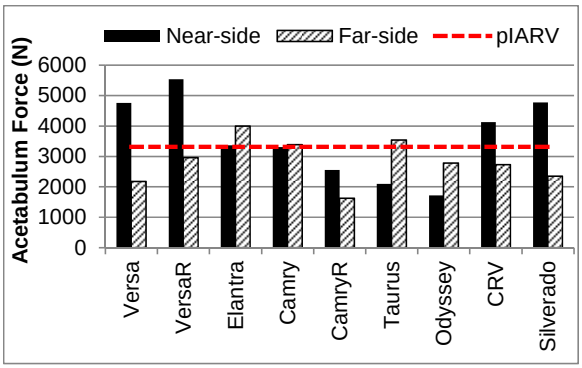

Figure 22. Peak acetabulum force in LSI and RSI tests.

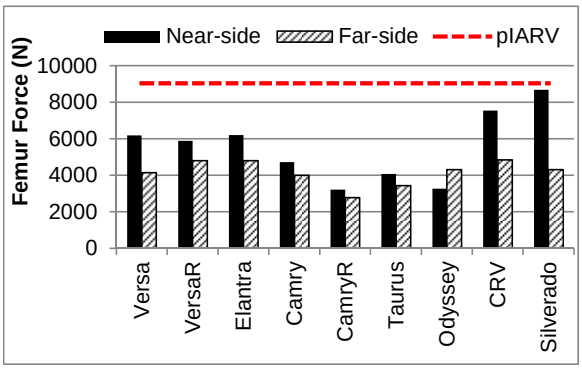

Figure 23. Peak femur compressive force in LSI and RSI tests.

<u>Lower Extremity</u>

The near-side occupant generally recorded a higher risk of lower extremity injury, quantified here using the Revised Tibia Index (Figure 24). This result was expected since intrusion into the occupant compartment is more likely on the near-side than the far-side. While this effect was exaggerated in the lightest (Versa) and heaviest (CRV, Silverado), there wasn't a consistent difference in the remainder of the vehicles. In one case (Elantra) the Tibia Index was noticeably higher in the far-side occupant location, though both values were below the provisional IARV.

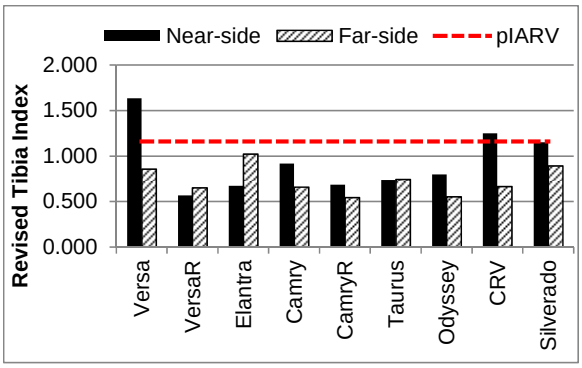

Figure 24. Maximum Revised Tibia Index in LSI and RSI tests.

DISCUSSION

Vehicle Response

It is normally assumed the vehicle response would be similar when impacted on the left or right of the vehicle. This appeared to be true for both intrusions and DVs for Camry and CamryR, but there were some apparent differences between the Versa and VersaR, conditions. In the LSI condition for the Versa, the toepan had the highest intrusion in the X-direction with over 300 millimeters of intrusion. VersaR showed the highest X-direction intrusion at the Bottom A-pillar and rocker panel, while the toepan intrusion was only 100 millimeters (Figure 25). Versa and VersaR DVs in the X- and Y-directions differed by around 10 kph (Figure 26).

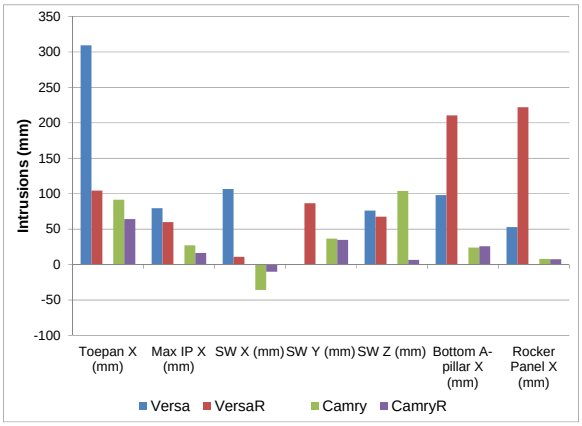

Figure 25: Comparison of intrusions between LSI and RSI

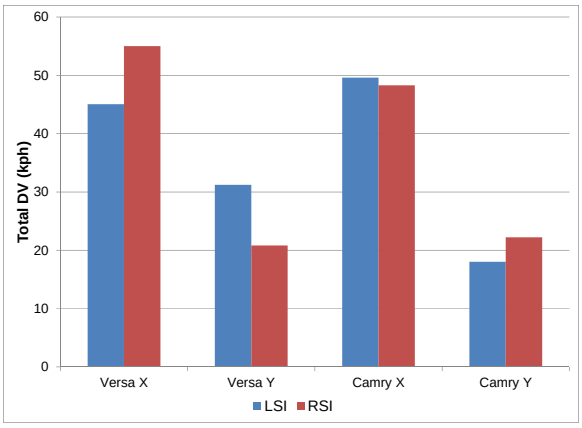

Figure 26: Comparison of Total DV between LSI and RSI

After the crash tests, it was noticed that the RSI condition had different frontal crush patterns than the LSI condition. In the LSI condition of the Versa, the frame and bumper were pushed inwards (Figure 27), whereas for VersaR the bumper was pushed straight back (Figure 28). Also, the separation of the wheel well and rocker panel may have caused the differences in the crush between Versa and VersaR (Figure 29).

Saunders et al, 2013 [2] showed that the max difference from three repeat test of a Chevrolet Cruse in the toepan and Rocker Panel was 14mm and 59 mm, respectively. Saunders also showed the max difference in DV was 2.4 kph. Even though, some of the differences in the LSI versus RSI may be explained by test variability, the difference is most likely due to asymmetric loading of the vehicle.

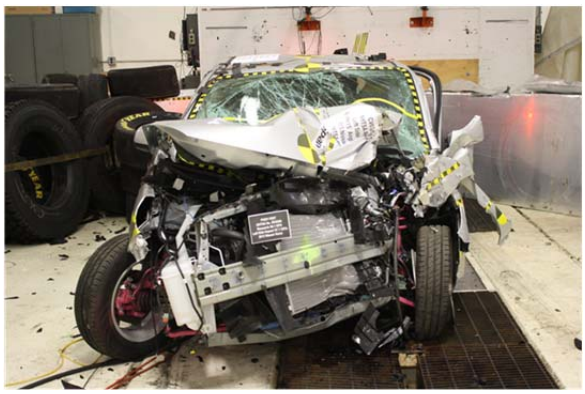

Figure 27: Deformation in a LSI of the Versa

Figure 28: Deformation in a RSI of the Versa

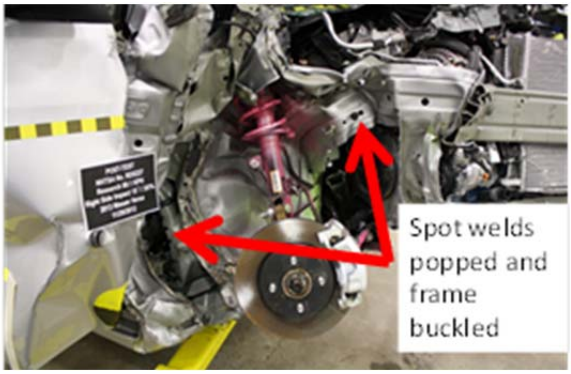

Figure 29: Buckling of the frame and separation of the wheel well and rocker panel

Occupant Response

The addition of both a right-side impact and a far-side occupant added two layers of complexity to the existing data in the Oblique RMDB crash test condition. Theoretically, the left-side impact and the right-side impact should be similar on the vehicle level, although the responses were not identical (see Figure 25 and Figure 26). Some components of the occupant response should be similar, including the acceleration pulse and interaction with the assumedly-symmetric belts and side curtain air bags, though the lack of symmetry in the frontal air bag could drive occupant response differences.

The two vehicle tests that were run in both the RSI and the LSI condition were the Versa and the Camry. In the Versa comparison, there was more engagement of the near-side occupant's head with the frontal air bag in the LSI condition, since the occupant was in the driver location and the frontal air bag was closer to the occupant initially. In contrast, the passenger's

head contacts the far outboard edge of the frontal passenger air bag in the RSI condition, which does not dissipate as much energy as the driver-side frontal air bag. The passenger's head continues to traverse forward and outboard at a higher relative velocity, resulting in a higher acceleration at the point of impact with the door panel (Figure 30).

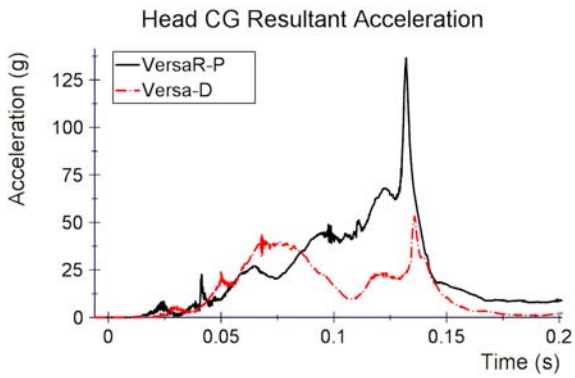

Figure 30. Near-side occupant head response in the Versa, comparing the RSI condition (black) to the LSI condition (red dash-dot).

In the Camry comparison, the occupant kinematics at the onset of the crash were noticeably different between the LSI and RSI modes. In the RSI mode, the front passenger seat appears to move upward relative to the vehicle floor, which allows upward motion of the occupant. The head contacts the roof (Figure 15), which imparts a large magnitude of acceleration early in the event (Figure 31). In the LSI mode, the same motion of the seat relative to the floor is apparent, but not at the same magnitude as in the RSI case. The driver's head does not impact the roof, but instead impacts the door frame at a higher velocity, resulting in a high acceleration peak later in the event (Figure 31).

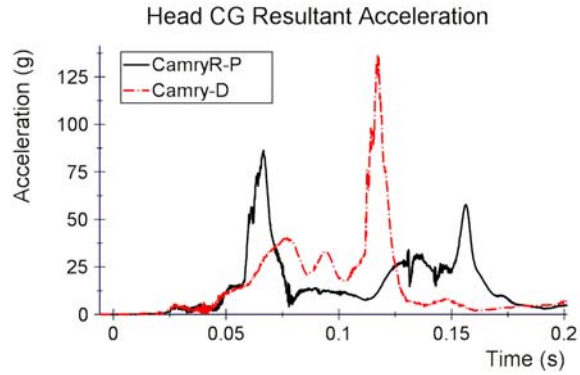

Figure 31. Near-side occupant head response in the Camry, comparing the RSI condition (black) to the LSI condition (red dash-dot).

Similar differences in head kinematics also occurred in the far-side occupant location due to the local interaction with frontal air bags of different sizes and shapes. The difference in head kinematics resulted in large discrepancies in the HIC15 and BRIC IAVs between the LSI and RSI conditions for both vehicle pairs (Figure 18, Figure 19). IAVs for other body regions, however, were relatively similar between the LSI and RSI for both the near- and far-side occupants. One other exception to this is the Tibia Index (Figure 24), where the Versa LSI near-side occupant exceeded the provisional IARV while the VersaR near-side occupant registered the lowest Tibia Index of all near-side tests.

Comparing near-side to far-side occupants, the biggest differences in the response were seen in the head region, specifically the angular rotation of the head. Interaction of the head of the far-side occupant with the frontal air bag resulted in large Z-axis rotations that were not present in most of the near-side occupant responses, with the exception of the Taurus, in which the side curtain air bag did not deploy, or the Silverado, where there was no head contact with the side curtain air bag. These cases resulted in the highest BRIC value.

The kinematics of the far-side occupant response were in part dictated by the interaction with the shoulder belt. The THOR ATD in the far-side location for each of these tests was equipped with the SD-3 shoulder, which was designed to improve occupant interaction with the shoulder belt in oblique crashes [6]. In both the LSI and RSI condition, the

far-side occupant lost engagement between the shoulder and the shoulder belt in all tests where the onboard video was available (note that the on-board high-speed video mount failed in the VersaR test, so it is not clear if and when the shoulder lost contact with the shoulder belt).

CONCLUSIONS

In general, this new set of testing of high sales volume vehicles tested in the Oblique condition showed the following:

- The near-side occupant in Oblique RMDB crash tests demonstrated similar trends and injury assessment values to the previously-evaluated Oblique tests.
- All nine of the far-side occupants measured BRIC IAVs in excess of the provisional IARV, primarily due to high angular velocities imparted by interaction with the frontal air bag and subsequent impact to the center instrument panel.
- RSI and LSI modes resulted in varied occupant kinematics due to differences in the interaction with the driver-side or passenger-side frontal air bag.
- Among the tests were two sets of LSI and RSI for the same vehicle models and the vehicle response, crush and DV were different for a LSI when compared to a RSI for the Versa, but similar for the camry vehicle tested on both sides. It should be noted that there is not enough data to conclude that the LSI and RSI vehicle responses are the same or different.

REFERENCES

1. Saunders, J., Craig, M. and Parent, D., "Moving Deformable Barrier Test Procedure for Evaluating Small Overlap/Oblique Crashes," SAE World Congress, paper no. 2012-01-0577, 2012
2. Saunders, J. and Parent, D., " Repeatability of a Small Overlap and an Oblique Moving Deformable Barrier Test Procedure," SAE World Congress, paper no. 2013-01-0762, 2013
3. Halloway, D.E., Saunders, J., Yoganandan, N. and Pintar, F. (2011) “An operational definition of small overlap impact for published NASS data.” SAE World Congress, paper no. 2011-01-0543.
4. Rudd, R., Scarboro, M., Saunders, J., “Injury Analysis of Real-World Small Overlap and Oblique Frontal Crashes,” 22nd ESV Conference, Paper No. 11-0384, 2011
5. Ridella, S., Parent, D., “Modifications to Improve the Durability, Usability, and Biofidelity of the THOR-NT Dummy,” 22nd ESV Conference, Paper No. 11-0312, 2011.
6. Törnvall, Fredrik. A New Shoulder for the THOR Dummy Intended for Oblique Collisions. Chalmers University of Technology, 2008.
7. Lemmen, P., Been, B., Carroll, J., Hynd, D., Davidsson, J., Song, E., Lecuyer, E., “Development of an advanced frontal dummy thorax demonstrator,” Proceedings of the 2012 IRCOBI Conference, 2012.
8. Takhounts, E.G., Hasija, V., Ridella, S.A., Rowson, S., Duma, S., “Kinematic Rotational Brain Injury Criterion (BRIC),” 22nd ESV Conference, Paper No. 11-0263, 2011.
9. Shaw, G., Parent, D., Purtsezov, S., Lessley, D., Crandall, J., Kent, R., Guillemot, H., Ridella, S.A., Takhounts, E., Martin, P., “Impact Response of Restrained PMHS in Frontal Sled Tests: Skeletal Deformation Patterns Under Seat Belt Loading,” Stapp Car Crash Journal, 53: 1-48, November 2009.

Table 3. Head contact locations and restraint deployment timing.

Mode	Vehicle	Contact Location (Evidence)	Frontal Air Bag Deployment	Side Curtain Air Bag Deployment	HIC15	Pretensioner Trigger Time
Left Front Driver						
LSI Oblique	Versa	AB (V, PT), SAB (V, PT), DP (V)	AD (18)	AD (46)	142	18
	Elantra	AB (V, PT), SAB (V, PT), DP (V)	AD (16)	AD (36)	346	16
	Camry	AB (V, PT), SAB (V, PT), DP (V, PT)	AD (26)	AD (26)	**835**	16
	Taurus	AB (V, PT), DP (V, PT)	AD (24)	AN	584	14
	Odyssey	AB (V, PT), SAB (V, PT)	AD (12)	AD (40)	96	12
	CRV	AB (V, PT), SAB (V, PT)	AD (26)	AD (44)	207	18
	Silverado	AB (V, PT), DP (V)	AD (20)	AD (20)	502	20
RSI Oblique	VersaR	AB (V, PT), IP/arm (V, PT)	AD (14)		647	14
	CamryR	AB (V, PT), IP/arm (V, PT)	AD (28)		105	18
Right Front Passenger						
LSI Oblique	Versa	AB (V, PT), IP (V, PT)	AD (18)		546	18
	Elantra	AB (V, PT), IP (V, PT)	AD (16)		**953**	16
	Camry	AB (V, PT), IP (V, PT)	AD (26)		569	16
	Taurus	AB (V, PT), IP (V)	AD (24)		157	14
	Odyssey	AB (V, PT), IP (V, PT)	AD (12)		624	12
	CRV	AB (V, PT), IP (V, PT)	AD (18)		**920**	18
	Silverado	AB (V, PT), column-mount gear shift (V, PT)	AD (24)		56	20
RSI Oblique	VersaR	AB (V, PT), SAB (V, PT), DP (V, PT)	AD (14)	AD (36)	**828**	14
	CamryR	AB (V, PT), SAB (V, PT), RR (V, PT)	AD (28)	AD (28)	364	18

AB	Air Bag
SAB	Side Curtain Air Bag
RR	Roof Rail
IP	Instrument Panel
DP	Door Panel
V	Video
PT	Paint Transfer

AD ( )	Available and Deployed (time deployed in ms)
AN	Available and Not Deployed
N	Not Available

Table 4. Summary of IAVs for near-side occupants in LSI and RSI Oblique crash tests

Body Region	Metric	Location	Units	Ref.	Versa [8084]	VersaR [8086]	Elantra [8089]	Camry [8088]	CamryR [8085]	Taurus [8087]	Odyssey [8097]	CRV [8096]	Silverado [8099]
Head	HIC15	Head CG		700	142	828	346	835	364	584	96	207	502
	HIC36	Head CG		1000	243	1102	721	835	364	759	140	289	502
	BRIC	Head CG		0.89	0.78	1.24	1.15	1.09	0.69	1.21	0.63	0.80	1.35
Neck	Tension	UNLC	N	2520	1828	2486	2047	1576	1216	2002	1536	1692	1376
	Compression	UNLC	N	-3640	-83	-739	-518	-113	-1583	-721	-134	-87	-450
Chest	Deflection	UL	mm	63	10.5	42.2	19.6	6.1	30.0	11.0	10.0	7.9	7.9
	Deflection	UR	mm	63	36.2	10.9	37.5	34.1	10.8	31.7	27.3	26.3	26.4
	Deflection	LL	mm	63	10.3	39.1	5.0	4.6	41.8	13.2	6.4	3.9	9.9
	Deflection	LR	mm	63	34.4	18.4	53.2	47.5	11.4	45.1	39.8	42.3	34.8
	Deflection	Peak	mm	63	36.2	42.2	53.2	47.5	41.8	45.1	39.8	42.3	34.8
	3ms Clip		G	60	42.7	44.5	45.8	34.8	41.9	47.8	34.9	44.6	29.2
Abdomen	Deflection	Peak	mm	90	71.3	75.9	69.9	73.4	79.1	69.6	64.0	66.2	65.4
Acetabulum	Force (Res.)	Left	N	3316	4757	2488	2290	2951	1865	2093	1638	4132	3439
	Force (Res.)	Right	N	3316	3514	5540	3363	3305	2557	1948	1716	2688	4775
Femur	Force (Axial)	Left	N	9040	6185	3865	4196	3725	3090	2689	3271	7536	5970
	Force (Axial)	Right	N	9040	5898	5880	6202	4718	3211	4069	2898	5048	8687
Tibia	Tibia Index	LU		1.16	0.830	0.430	0.503	0.577	0.637	0.302	0.734	0.550	1.151
Tibia	Tibia Index	RU		1.16	1.635	0.526	0.491	0.779	0.684	0.641	0.797	1.134	0.697
Tibia	Tibia Index	LL		1.16	0.779	0.558	0.604	0.696	0.427	0.251	0.791	0.491	0.783
Tibia	Tibia Index	RL		1.16	0.610	0.567	0.672	0.917	0.668	0.736	0.678	1.248	0.971
Tibia	Tibia Index	Max		1.16	1.635	0.567	0.672	0.917	0.684	0.736	0.797	1.248	1.151
Ankle	[in/e]version	Left	deg	35	22.5	23.7	30.8	33.7	27.3	28.5	13.3	21.2	42.9
Ankle	[in/e]version	Right	deg	35	36.5	41.2	51.8	40.6	38.7	33.8	37.5	35.7	31.4
Ankle	[p/d]flexion	Left	deg	35	21.4	21.7	29.5	36.4	24.1	36.5	33.7	37.9	34.7
Ankle	[p/d]flexion	Right	deg	35	36.6	43.2	21.3	18.4	35.6	27.8	22.5	35.5	48.2
Ankle	Rotation	Max	deg	35	36.6	43.2	51.8	40.6	38.7	36.5	37.5	37.9	48.2
Belt	Lap Belt	Max	N	NA	1612	1725	8143	3146	3461	4578	3997	3249	2375
	Shoulder Belt	Max	N	NA	IM	4928	5119	4749	IM	3733	3995	3624	2979

Table 5. Summary of IAVs for far-side occupants in LSI and RSI Oblique crash tests

Body Region	Metric	Location	Units	Ref.	Versa [8084]	VersaR [8086]	Elantra [8089]	Camry [8088]	CamryR [8085]	Taurus [8087]	Odyssey [8097]	CRV [8096]	Silverado [8099]
Head	HIC15	Head CG		700	546	647	953	569	105	157	624	920	56
	HIC36	Head CG		1000	600	800	953	569	193	265	633	920	94
	BRIC	Head CG		0.89	1.99	1.04	1.49	1.33	1.35	1.18	1.17	1.49	1.15
Neck	Tension	UNLC	N	2520	2527	IM	1465	1428	4908	1205	1977	2183	930
	Compression	UNLC	N	-3640	-145	-23	-752	-1167	-896	-42	-212	-345	-223
Chest	Deflection	UL	mm	63	38.5	16.2	31.4	33.5	13.2	32.1	23.9	33.9	29.4
	Deflection	UR	mm	63	16.8	40.3	33.3	38.1	35.8	27.4	13.7	17.7	11.9
	Deflection	LL	mm	63	41.4	5.9	38.5	30.9	2.5	32.2	25.9	27.8	29.0
	Deflection	LR	mm	63	3.0	30.5	11.1	11.0	25.3	11.8	4.9	6.0	8.7
	Deflection	Peak	mm	63	41.4	40.3	38.5	38.1	35.8	32.2	25.9	33.9	29.4
	3ms Clip		G	60	46.5	52.4	35.5	26.3	30.4	39.9	22.2	28.9	24.9
Abdomen	Deflection	Peak	mm	90	53.7	66.5	62.8	67.0	61.3	67.3	56.7	63.7	66.1
Acetabulum	Force (Res.)	Left	N	3316	2055	2956	3994	2694	1508	2624	1718	2415	1652
	Force (Res.)	Right	N	3316	2174	2617	3226	3379	1618	3541	2777	2724	2344
Femur	Force (Axial)	Left	N	9040	3270	4783	4784	3983	2124	2468	4256	4354	4301
	Force (Axial)	Right	N	9040	4126	4445	417	3359	2757	3415	4297	4826	4054
Tibia	Tibia Index	LU		1.16	0.852	0.584	0.672	0.476	0.323	0.739	0.536	0.587	0.888
Tibia	Tibia Index	RU		1.16	0.402	0.541	1.017	0.656	0.540	0.501	0.508	0.661	0.365
Tibia	Tibia Index	LL		1.16	0.690	0.645	0.566	0.392	0.210	0.402	0.548	0.190	0.651
Tibia	Tibia Index	RL		1.16	0.285	0.535	0.821	0.465	0.539	0.328	0.396	0.485	0.305
Tibia	Tibia Index	Max		1.16	0.852	0.645	1.017	0.656	0.540	0.739	0.548	0.661	0.888
Ankle	[in/e]version	Left	deg	35	42.7	45.5	101.0	78.8	31.9	90.4	81.9	94.4	57.7
Ankle	[in/e]version	Right	deg	35	41.7	61.4	16.9	52.8	36.3	84.4	37.8	76.6	68.0
Ankle	[p/d]flexion	Left	deg	35	21.6	26.0	27.9	26.5	22.5	29.8	32.4	38.4	25.6
Ankle	[p/d]flexion	Right	deg	35	19.9	16.5	45.9	31.2	26.5	34.2	22.2	34.6	14.5
Ankle	Rotation	Max	deg	35	42.7	61.4	101.0	78.8	36.3	90.4	81.9	94.4	68.0
Belt	Lap Belt	Max	N	NA	6213	3461	9346	5629	6536	8271	5108	4118	4153
	Shoulder Belt	Max	N	NA	4923	4740	4479	3354	4236	5531	2823	3280	2889

PARAMETRIC STUDY USING THE OLC AND SPÜLL TO QUALIFY THE SEVERITY OF THE FULL-WIDTH RIGID TEST AND DESIGN AN IMPROVED FRONT-END

Christophe Picquet,
Richard Zeitouni,
Céline Adalian
PSA Peugeot Citroën
France
Paper number 13-0442

ABSTRACT

Self-protection of car occupant is a crucial topic all over the world. Restraint systems have to be designed to protect various sizes of occupants involved in several type of crash and therefore several types of crash pulses.
Considering the additional constraints applied on the car design these days (CO_2 emission and therefore mass reduction, or reduction of front overhang) improvements and optimisation on the car structure are needed to better control the pulse. Otherwise, if the pulse is too severe, it will be difficult to design adequate restraint systems.

PSA Peugeot Citroën launched a large programme with physical crash tests and modelling on the full-width rigid barrier test.
This was applied to several types of cars and car architecture (small family, large family cars).
The 8 x 16 (128) load cell wall was used in each crash test to get a lot of measurements essential for the correlation of the numerical models.

The physical crash tests permitted to identify the contribution of each load path on OLC and spüll (pulse severity). The load paths analysed are the subframe, the side members, the engine, the upper structure of the body in white...
These tests were used to create correlated numerical model of each car size or architecture.
Then, correlated crash simulations were used to carry out a parametric study via changing the impact speed, mass, subframe stiffness, longitudinals stiffness, engine size and position.
This parametric study helped in defining the major contributors for each car size or architecture.

As expected, the influence of car mass and test velocity were highlighted to have a similar equivalent consequence on the severity of the crash (OLC and Spüll severity) whatever the car size or architecture.
But for other parameters such as subframe stiffness, longitudinals stiffness, engine size and position, it was surprising to see that their influence is not as high as expected.
One last surprising result is to see that front end internal components have a low influence on the pulse severity with respect to the stiffness of the components in charge of transferring the load from the front end to the cockpit and subframe.

INTRODUCTION - AIM OF THE STUDY

Frontal impact on a rigid obstacle are the most severe impacts with respect to change of velocity (deceleration) sustained by the occupants.
This test configuration will be used worldwide in the near future (already in China [1], Korea, Japan, USA [2] + possible new regulation on frontal impact and Euro NCAP 2015 [3]). It will also be used with more demanding biomechanical criteria designed to better protect vulnerable users.
In parallel, the new constraints applied on CO_2 emission imply a huge work on mass reduction. And the current trend in car designs requires a reduction of front overhang.
These features have a negative effect on passive safety: they increase the pulse severity in frontal impact when the full width of the car is involved.
In order to control the pulse severity and achieve a good passive safety protection level, PSA Peugeot Citroën launched a programme to identify the main parameters that influence the car deceleration.
Test programmes and numerical analyses on several types of vehicles were carried out.
Mixed results were found. Some car structures do not need to be changed to reach a good passive safety performance in this new test and occupant characteristics. But others would naturally reach a too high level of acceleration and need to be improved to limit the pulse to be able to correctly protect the occupants.
This paper presents the study on these latter vehicles focusing on 2 architectures: small car and sedan car.

METHOD

A test programme was carried out in order to correlate numerical models. These numerical models were then used to assess the most influent parameters via parametric studies.

In addition to the standard parameters such as load cell wall forces, B-Pillar pulse, velocity and displacement, two other parameters were used in the analysis. They are presented below.

Analysis was made on several cars, but this paper details the results found on the small car, and gives the overall conclusion for the sedan car as well.

Deceleration severity criteria: OLC and SPÜLL

To assess the severity of the change of velocity in a frontal impact, we are using two criteria. The first one is the spüll.
Its definition is:

$$\text{Spüll} = v^2/t \qquad (1).$$

where t is the impact duration, and v is the vehicle velocity calculated via the acceleration (with v(t=0)=0). Unit of spüll is W/kg.

The second criterion is OLC (Occupant Load Criterion) [4], defined as shown in Figure 1.

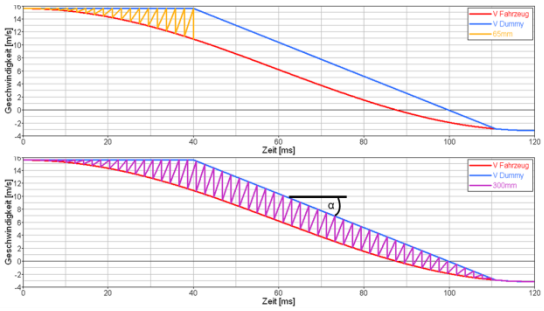

- 65mm free motion of occupant (relative to vehicle)
- idealised deceleration of occupant until 235mm forward displacement
- the slope is equal to the OLC (tan(α) = OLC [g])

Figure 1. OLC definition

OLC has the same dimension as an acceleration and its unit is in G (G = 9.8 m/s²).

PHYSICAL TESTS

Test configuration

For our test programme, an instrumented rigid wall 126 load cells) was used (see Figures 2 and 3). It should be note that 2 cells were missing with respect to the standard 128 load cell wall: the extreme bottom left and the extreme top right load cells.

Figure 2. Load cell wall.

A1	B1	C1	D1	E1	F1	G1	H1	I1	J1	K1	L1	M1	N1	O1	
A2	B2	C2	D2	E2	F2	G2	H2	I2	J2	K2	L2	M2	N2	O2	P2
A3	B3	C3	D3	E3	F3	G3	H3	I3	J3	K3	L3	M3	N3	O3	P3
A4	B4	C4	D4	E4	F4	G4	H4	I4	J4	K4	L4	M4	N4	O4	P4
A5	B5	C5	D5	E5	F5	G5	H5	I5	J5	K5	L5	M5	N5	O5	P5
A6	B6	C6	D6	E6	F6	G6	H6	I6	J6	K6	L6	M6	N6	O6	P6
A7	B7	C7	D7	E7	F7	G7	H7	I7	J7	K7	L7	M7	N7	O7	P7
	B8	C8	D8	E8	F8	G8	H8	I8	J8	K8	L8	M8	N8	O8	P8

Figure 3. Illustration of load cell wall and numbering.

Test analysis: load cell wall break down

As shown in Figure 4, the efforts sustained by each load cell are measured throughout time.

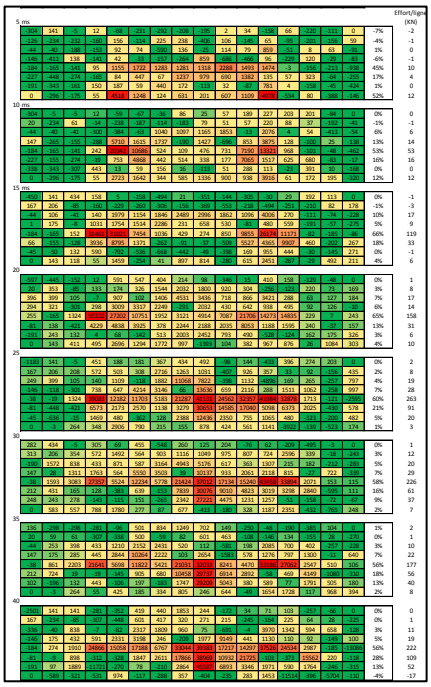

Figure 4. Load breakdown

For the analysis, some cells are grouped together (we used the numbering presented in Figure 2):

- Left longitudinal: cells D[4…6]+E[4…6]+F[4…6]
- Right longitudinal: cells K[4…6]+L[4…6]+M[4…6]
- Engine block: cells G[3…7]+H[3…7]+I[3…7]+J[3…7]

This grouping helps to analyse the contribution of the main load path throughout the impact (see Figures 5 and 6).

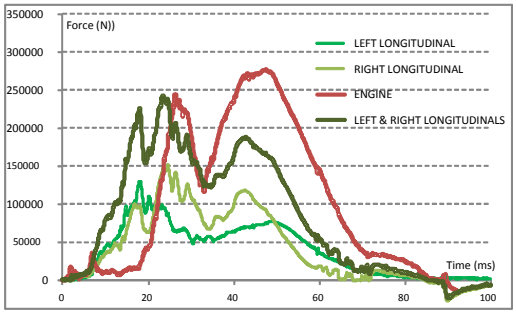

Figure 5. Load (in N) throughout time –small car

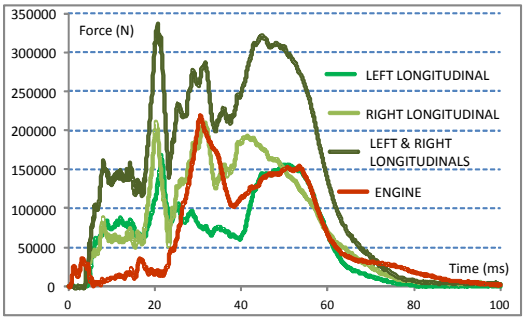

Figure 6. Load (in N) throughout time –sedan car

One can notice easily that the breakdown is different between the two architectures.

For the small car, the longitudinals contribution is predominant in the first part of the impact (up to 25 ms). Then the engine block load path (GMP) is the major contributor up to the end of impact.
It can be guessed that it is the stopping of the engine that is essential in the vehicle deceleration.

For the sedan car, the breakdown is radically different even if the longitudinals contribution is predominant in the first part of the impact. Indeed, the engine block load (GMP) is never higher than the longitudinals. And between 40 to 60 ms the ratio is 1:2. Therefore, on the sedan architecture, the longitudinals are essential to stop the vehicle.

Use of the Spüll to quantify and confirm the contribution of the load path of the overall vehicle deceleration

In order to link the contribution of each load path to the overall vehicle deceleration, a study was carried out using the steps described below.

Calculation of the effective mass

We used the average of the two B-Pillar accelerations to calculate the vehicle velocity.

From this vehicle velocity (v_{veh}) and from the effort measured on the load cell wall, we can calculate the effective mass M(t) :

$$M(t) = 2/v_{veh}(t)^2 \, (E_{max} - \int F(t).\, v_{veh}(t)) \quad (2).$$

where E_{max}=MAX ($\int F(t).\, v_{veh}(t)$)

Figure 7 presents the evolution of the effective mass throughout the impact.

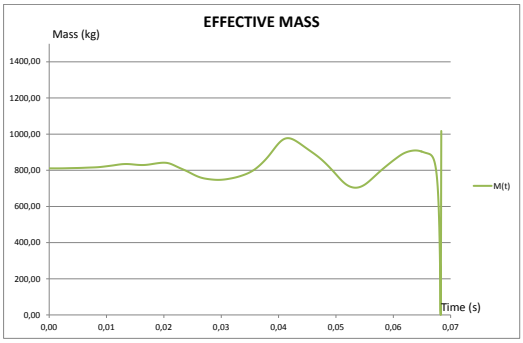

Figure 7. Evolution of effective mass throughout time

Check of the calculation of the effective mass

To check the calculation of the effective mass, we reckon the vehicle main mechanical parameters (acceleration, velocity and displacement) from the effective mass.
Acceleration is reckoned via F(t)/M(t).
Velocity is the simple integration of acceleration.
Displacement is the simple integration of velocity.
Figure 8 shows that this calculation is acceptable.

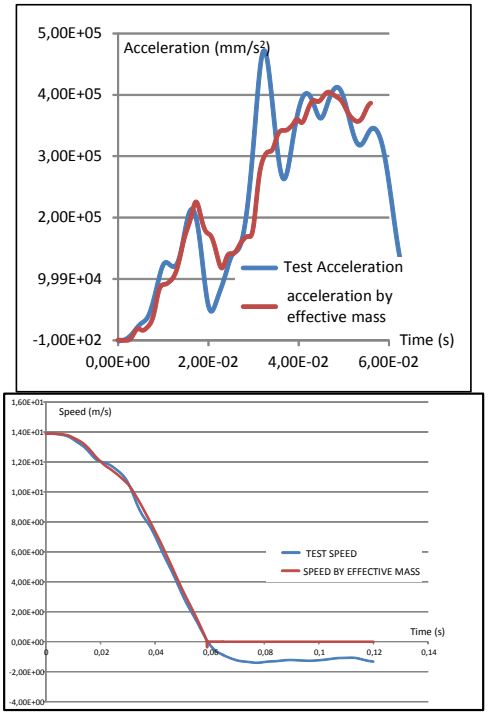

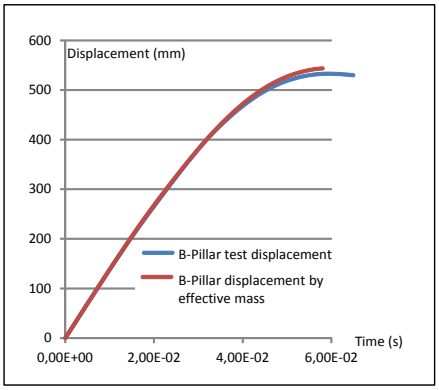

Figure 8. Check of the calculation of the effective mass

Calculation of each load path acceleration

From the effective mass and the load path forces measured on the wall, it is possible to reckon an acceleration for each load path.
For the load path i, the acceleration is given by:
$\gamma_i(t) = F_i(t) / M(t)$

Five main load paths were identified: the 2 longitudinals, the subframe, the engine block effort on the firewall, and the superstructure. The corresponding load cells are shown in Figure 9.

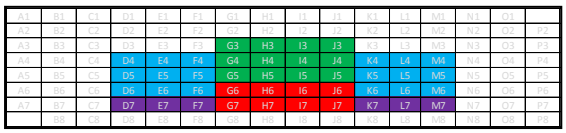

Figure 9. Corresponding load cells for each of the five main load paths (light blue = longitudinals x 2, red = subframe, green = engine block, purple = superstructure).

The integration of these accelerations leads to the change of velocity, called DV, of each load path. One can notice in Figure 10 that the sum of DV is very close to the overall vehicle DV. This means that we did not forget a major load path.

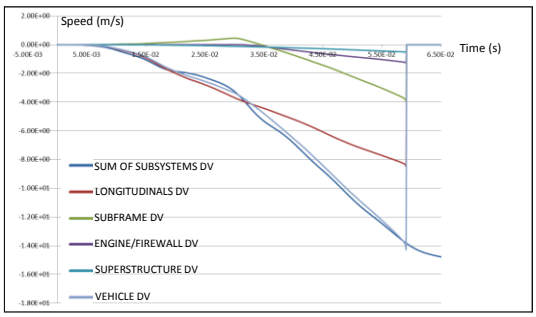

Figure 10. Comparison between sum of DV and vehicle DV.

Calculation of the spüll for each load path

Thanks to the DV, we can come back to the overall spüll and highlight the relative contribution of each load path as percentages by this formula:
Spüll = $(\Sigma_i DV_i)^2/t$ avec i = subsystem

Applying these steps to the small and sedan vehicles gives the breakdown shown in Figures 11 and 12.

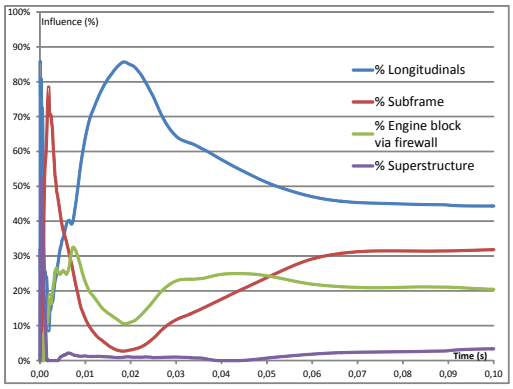

Figure 11. Small vehicle test – percentages of each load path on the overall spüll throughout time.

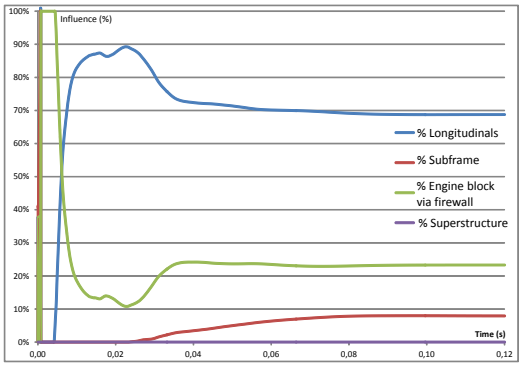

Figure 12. Sedan vehicle test – percentages of each load path on the overall spüll throughout time

At the end of the impact, the contribution of each load path on the overall Spüll is given in Table 1

Table 1.
Contribution of each load path on the overall spüll for small car and sedan car

Breakdown (%) end of test	Small car	Sedan car
Longitudinals	44	69
Subframe	32	8
Engine on firewall	20	23

The percentages are correlated to the level of force measured. Therefore, we can state that for the small car architecture the major contributors on the pulse severity are the engine block stopping in the firewall and the subframe; whereas for the sedan car architecture it is the longitudinals.

NUMERICAL MODELS CORRELATION

Numerical models of the two car architectures were created and correlated in terms of overall behaviour

(B-Pillar deceleration) but also in terms of relevance of the different load path behaviour.
The following details the results found on the small car. And later, we will give the overall conclusion for the sedan car as well.

Overall behaviour correlation

Figure 13 presents the overall deceleration measured in the physical test and compared with the numerical model for the small car. The attached table shows the main parameters: acceleration peak, OLC, time of DV=0, Spüll and time of Spüll max.

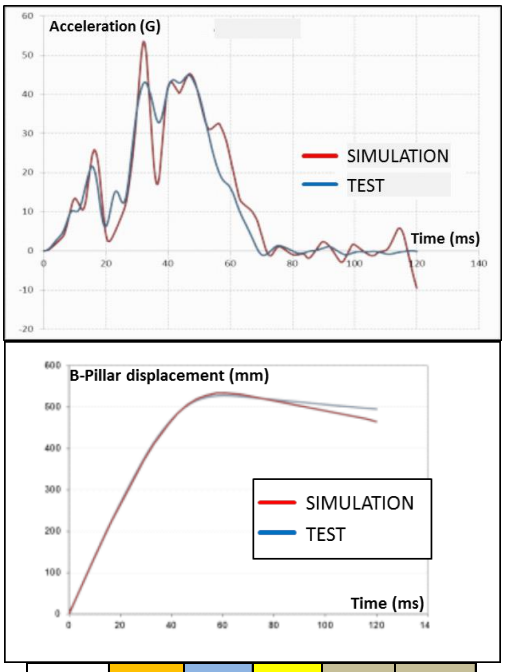

	Decel max. (g)	OLC	DV=0 Time (ms)	SPULL (W/kg)	SPULL max time (ms)
Test	48.3	31.7	62.0	3202	63.2
Simulation	53.7	32.0	59.9	3321	65.2

Figure 13. Small car – comparison of physical test vs numerical test on the overall parameters.

The level of correlation of the small car numerical model is really good when looking at the overall parameters.
Let's have a look now at the level of correlation of specific components: the load paths identified previously.

Representativeness of the load path contribution on the pulse severity criteria

The full load cell wall was numerically modelled (see Figure 14) in order to:

- Compare the overall force mesasured in the physical crash test to the numerical measurement. This will be done by comparing the force-displacement curves
- Compare the breakdown into the different load paths as calculated earlier with the ones reckoned via the parameters available in the numerical model

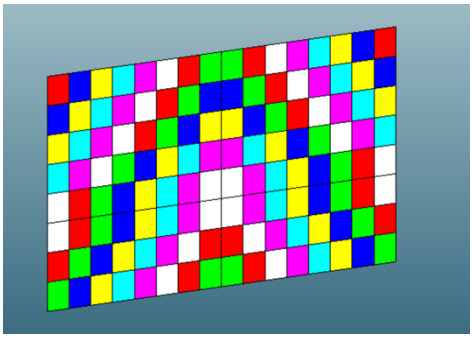

Figure 14. Modelling of the full-width rigid frontal impact test: load cell wall with its 128 load cells.

The comparison between physical test and simulation for the small car of the overall load cell wall force vs. car displacement is shown in Figure 15.

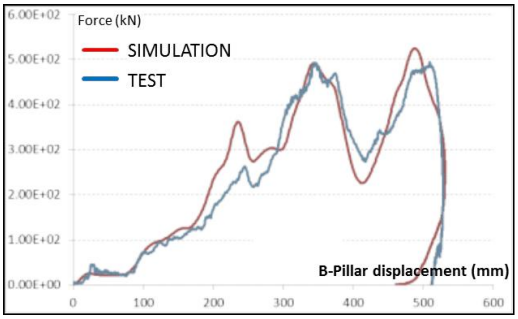

Figure 15. Small car – comparison between physical test and simulation of the overall load cell wall force vs. car displacement.

Here again, the small car model gives very good correlation: the chronology is very similar –the peaks occur at the same overall vehicle compression - as well as the magnitude, except for the first peak which magnitude is higher for simulation.

If we look at the breakdown and contribution of the main load paths on the results of Spüll, we also have good correlation.

Figure 16 presents the breakdown in percentage of each load path to the overall Spüll for the numerical model (a) and for the physical test (b). Comparison between Figure 16 (a) and Figure 16 (b) shows that the breakdown as assessed in the physical test via indirect measurement is confirmed via the parameters available in the numerical model.

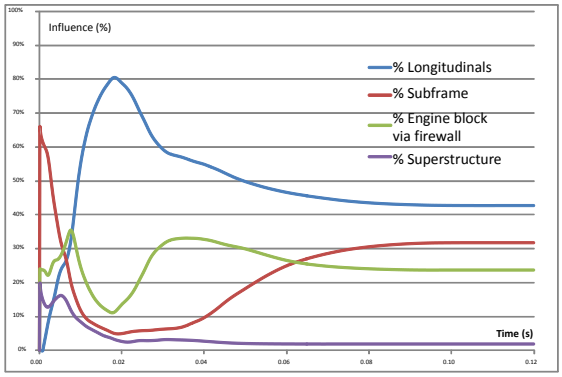

(a)

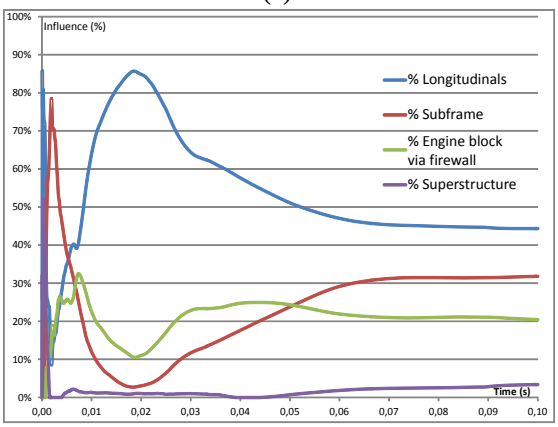

(b)

Figure 16. Small vehicle – contribution in percentages of each load path to the overall Spüll throughout time for the numerical model (a) and for the physical test (b).

This comparison between physical test and numerical model and the confirmation of the breakdown between load paths is summarized in Table 2 via the percentages of contribution at the end of the impact.

Table 2.
Contribution of each load path on the overall spüll at the end of crash for small car – comparison between physical test and numerical model

Breakdown (%) end of crash	Small car test	Small car Simulation
Longitudinals	44	43
Subframe	32	32
Engine on firewall	20	24

This part of the study allows us to state that the small car model is good to be used for a parametrical study because its level of correlation is very good.

PARAMETRICAL STUDY

We already presented the two mechanical parameters we use to translate the impact severity (OLC and Spüll) of a crash.
In order to know what are the car architecture parameters that we need to control to be able to design an ideal car architecture, we need to carry out a parametrical study on these parameters.

Method

We only focused at the individual influence of each parameter. The combination of parameters variations will be studied later.
The parameters linked to the car architecture and design are:

- car mass
- longitudinals force level
- subframe force level
- tunnel force level
- size of engine block
- firewall location
- subframe front end location

They are presented more in details in the next chapter. Then we will present the results of their variation.

The variation made were always realistic ones that could be applied in a car design. And every time the intrusion level was checked to ensure that the global car synthesis was still realistic and acceptable.

Presentation of the parameters and their variation

Change of car mass

There are increasing constraints throughout the years about CO_2 emission. This implies a huge work on car architecture to reduce their weight. Therefore we decided to analyse a 100 kg of mass reduction.
On the other hand, a same car architecture / platform can host a heavier superstructure (SW or SUV variants) and / or a heavier powertrain (Hybrid engines). This is why we also studied a 200 kg of mass increase.

Change of longitudinals force level

In the first part of our study, we highlighted that the longitudinals are one of the major contributors (or even the major) on the Spüll magnitude.
Therefore the longitudinals force level had to be part of this parametric study.
For the small car, we applied a +/- 20% variation.

Change of subframe force level

The contribution of the force transmitted from the engine block to the subframe is 32% on the Spüll for the small car as shown previously in Table 2. Here again, we applied a +/- 20% variation.

Change of tunnel force level

The tunnel plays an important part in the transfer of the front-end forces to the understructure and the cockpit. Therefore, we decided to study the influence of an increase of 20% on the force of the front-end zone of the tunnel.

Change of size of engine block and its location

It is natural to feel that the size of the engine block is of high importance to control the pulse severity as its impact on the wall should influence the time needed to stop the car, but also because the firewall will not sustain any load before the engine block starts to contact it.
This is why we decided to modify its volume via a change of +/- 50 mm in the engine + gear package.

Another independent modification was made on its location: variation of +/- 50 mm.

Change of firewall location

As already explained for the engine block, we applied the same reasoning to the firewall location. Again, we applied a +/- 50 mm variation in the zone of contact between the engine block and the firewall.

Change of subframe front-end location

Same reasoning on the subframe front-end location applied to the contact between the subframe and the engine block. But, we only use a +50 mm change.

Results

The detailed results presented here are the ones obtained for the small car architecture.

The colour code used in the following tables helps to identify the variation in percentage with respect to the reference model.
Throughout this paper, the colour code is the same:

- green means variation 10% or below
- yellow means variation between 11% and 20%,
- orange means variation between 21% and 30%,
- red means variation equal or above 30%.

Change of car mass

We took into account a variation of - 100 kg and +200 kg with respect to the reference model. Results are presented in Table 3

Table 3.
Influence of car mass on OLC and Spüll parameters

		REFERENCE	MASS INFLUENCE									
			-100 kg	% difference	-50 kg	% difference	+20 kg	% difference	+100 kg	% difference	+200 kg	% difference
OLC (g)	RIGHT	32,5	32,9	1%	32,3	-1%	32,1	-1%	31,9	-2%	30,9	-5%
	LEFT	32,2	32,4	0%	32,0	-1%	31,9	-1%	31,8	-1%	31,0	-4%
SPULL (W/kg)	RIGHT	3464,1	3520,0	2%	3445,8	-1%	3383,5	-2%	3219,8	-7%	3065,7	-12%
	LEFT	3309,1	3400,2	3%	3328,1	1%	3233,9	-2%	3148,0	-5%	3011,9	-9%

Impact weight does not have a strong influence on OLC. A difference of 300 kg would change OLC by 4% only (for the left OLC, the one obtained with the left B-Pillar). Differences on the Spüll are stronger, with a maximum increase of 15% on the right Spüll. Influence of mass is only visible on Spüll.
If we analyse the curves, relationship between vehicle mass and OLC or mass and Spüll is linear and negative (see Figure 17).

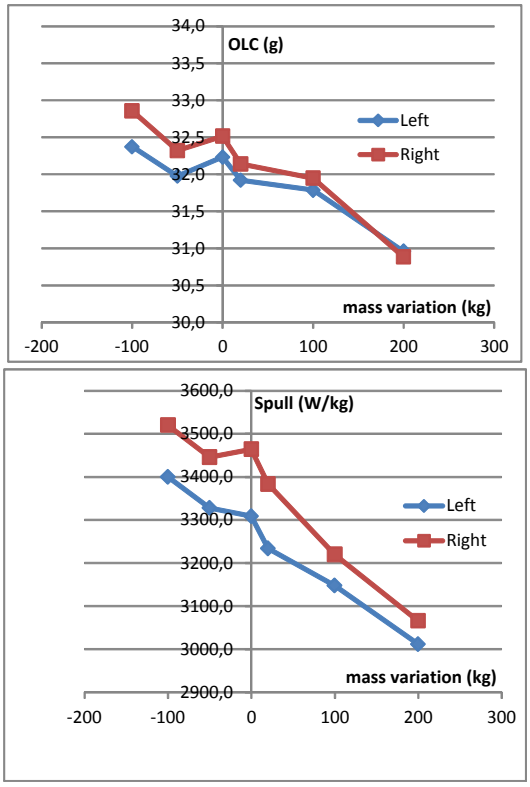

Figure 17. OLC and Spüll trends with respect to vehicle mass.

We can state that a decrease of 10 kg in the vehicle mass would increase the Spüll by 14 W/kg.

After the study of the initial condition parameters, we can pass on the influence of the load-path force levels. It is expected that if the energy is absorbed faster because the load path are stronger, the stopping of the car will be different and therefore the change of velocity (<=> pulse severity) sustained in the cockpit will be modified.

Change of vehicle design - longitudinals force level

We already stated that the longitudinals are the major contributors to the Spüll at the end of impact. We therefore expect a strong influence of the longitudinals force level on the pulse severity.

Table 4 presents the results and Figure 18 shows visually the trends.

Table 4.
Influence of longitudinals force level on OLC and Spüll parameters

		REFERENCE	LONGITUDINALS FORCE INFLUENCE			
			+20%	% difference	-20%	% difference
OLC (g)	RIGHT	32,5	32,0	-2%	32,7	0%
	LEFT	32,2	31,3	-3%	32,4	1%
SPULL (W/kg)	RIGHT	3464,1	3377,9	-2%	3254,9	-6%
	LEFT	3309,1	3258,0	-2%	3166,2	-4%

Only the peaks of deceleration show a moderate influence of the longitudinals force level. The other parameters are not or very little modified.

Figure 18 shows that it is not possible to highlight an obvious trend with OLC or Spüll.

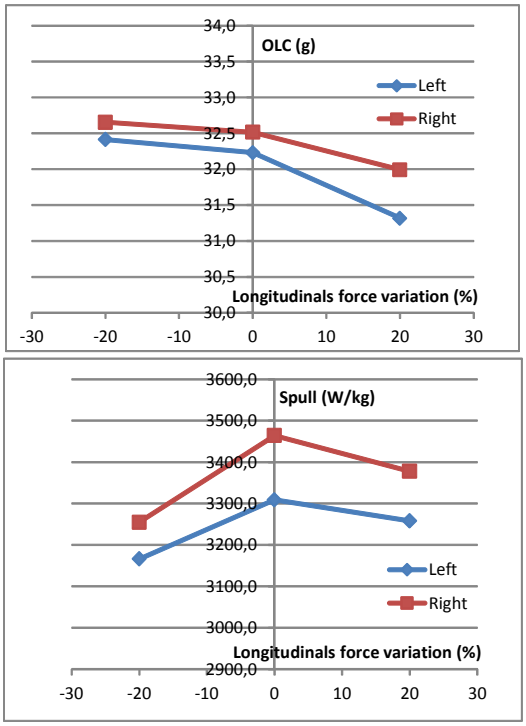

Figure 18. OLC and Spüll trends with respect to longitudinals force level

Contrary to what was expected, a strong change in the longitudinals force level will not strongly affect the pulse severity as measured via OLC and Spüll. In order to explain it, we compared the longitudinals (left and right) kinematic of the three models as shown in Figure 19.

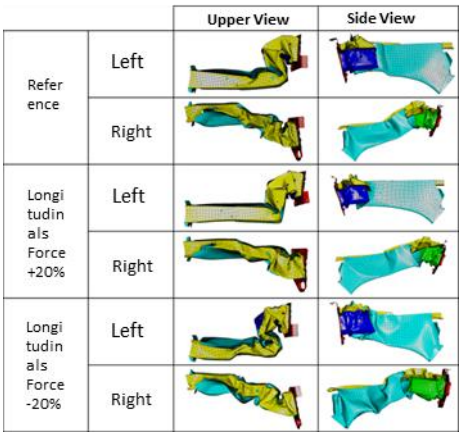

Figure 19. Longitudinals (left and right) kinematic of the three models

The kinematics are quite similar and we guess this is the reason why the pulse severity parameters we not changed by a +/-20% change in the longitudinals force level.
Indeed the energy absorption performance definitely depends on the kinematics (overall rotation or buckling) more than on the stiffness of the beam. This should be studied in a future research work on the topic.

Change of vehicle design - subframe force level

Table 5 presents the results shows visually the trends of the influence of the subframe force level on the pulse severity.

Table 5.
Influence of subframe force level on OLC and Spüll parameters

		REFERENCE	SUBFRAME FORCE INFLUENCE			
			+20%	% difference	-20%	% difference
OLC (g)	RIGHT	32,5	32,6	0%	30,0	-8%
	LEFT	32,2	32,4	1%	29,8	-8%
SPULL (W/kg)	RIGHT	3464,1	3351,4	-3%	3131,9	-10%
	LEFT	3309,1	3259,5	-1%	3063,9	-7%

The results are outstanding. If an increase of 20% in the subframe strength almost gives no change to Spüll and OLC, the same amount of decrease as a strong influence. The consequence is a decrease by 8% of OLC and 10% for Spüll.
This can be explained by an increase in compressibility offered by the softening of the subframe that decreases the deceleration.
On the contrary, stiffening the subframe do not change a lot the deceleration, because the reference model is already strong enough and do not offer a lot of deformation.

We can conclude that the softening of the subframe can be a key action to make if the deceleration needs to be decreased.

Change of vehicle design - tunnel force level

The last force level we decided to modify was the tunnel one. Table 6 presents the results.

Table 6.
Influence of tunnel force level on OLC and Spüll parameters

		REFERENCE	TUNNEL FORCE INFLUENCE	
			+20%	% difference
OLC (g)	RIGHT	32,5	32,6	0%
	LEFT	32,2	32,2	0%
SPULL (W/kg)	RIGHT	3464,1	3470,7	0%
	LEFT	3309,1	3290,6	-1%

An increase of the tunnel force level would not influence the pulse severity.

As a partial conclusion, we can state that the change in the load-path force level did not give the trends we expected. The only significant influence highlighted was the softness of the subframe that would decrease Spüll and OLC values.

We already quantified the influence of initial test conditions and of load-path force levels. Now we can pass on the influence of the load-path locations or size. These changes are expected to have an influence on the stacking and therefore on the timing, thus on the maximum severity of the pulse sustained in the cockpit.

Change of vehicle design - size of engine block

The first parameter studied was the engine block size and the results are presented in Table 7.

Table 7.
Influence of size of engine block on OLC and Spüll parameters

		REFERENCE	ENGINE LENGTH INFLUENCE			
			+50 mm engine length	% difference	-50 mm engine length	% difference
OLC (g)	RIGHT	32,5	32,3	-1%	31,7	-2%
	LEFT	32,2	32,1	0%	31,3	-3%
SPULL (W/kg)	RIGHT	3464,1	3347,7	-3%	3407,9	-2%
	LEFT	3309,1	3274,2	-1%	3251,8	-2%

There is little effect of the engine block size and no specific trend as shown in Figure 20.

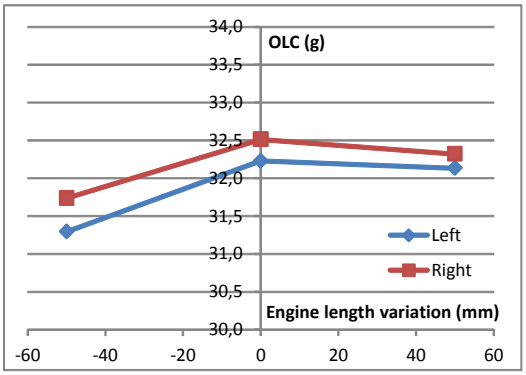

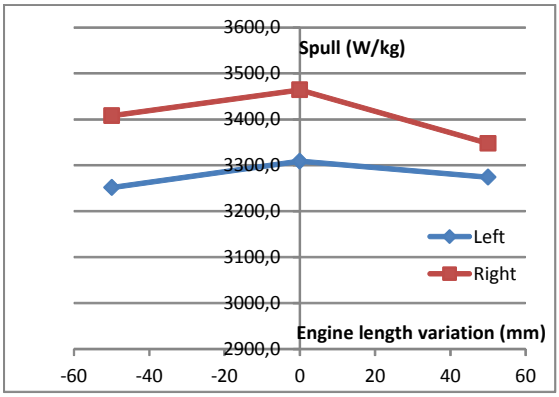

Figure 20. OLC and Spüll trends with respect to engine block size

The consequences on overall vehicle behaviour for the small car are surprising. If an increase in intrusion occurred due to a larger engine block can explain partially these results, we expected more severe level of deceleration than the one measured.

Change of vehicle design - firewall location

The second parameters that should influence the stacking and therefore the pulse severity is the firewall location. We looked at the location in front of the engine block zone of contact. We did not change the longitudinals location.
Table 8 presents the results.

Table 8.
Influence of firewall location on OLC and Spüll parameters

		REFERENCE	FIREWALL LOCATION INFLUENCE			
			50 mm X forward firewall location	% difference	50 mm X rearward firewall location	% difference
OLC (g)	RIGHT	32,5	31,7	-2%	32,5	0%
	LEFT	32,2	32,0	-1%	32,1	0%
SPULL (W/kg)	RIGHT	3464,1	3271,9	-6%	3431,0	-1%
	LEFT	3309,1	3224,3	-3%	3305,5	0%

Shifting the firewall rearward would not influence the criteria. But shifting it forward seems to improve Spüll and OLC.

To shift it forward, on the small car, we increased by 50 mm the firewall cross beam section as shown in Figure 21.

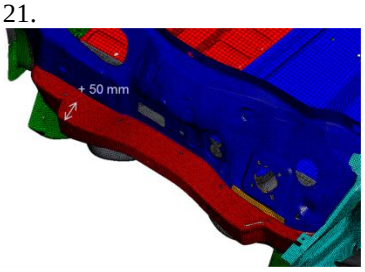

Figure 21. How we did the firewall shift forward on the small car.

A detailed look at the firewall cross beam in the model is given in Figure 22 and it shows that this element is significantly deformed.

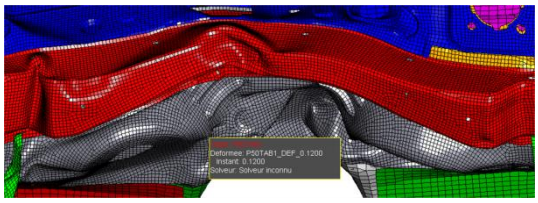

Figure 22. small vehicle model – deformation of the firewall cross beam when the firewall is put 50 mm forward

This means that the firewall was actually not shifted by 50 mm. but this also means that the stiffness/compression behaviour of the impact between the engine block and the firewall central beam was modified.
Therefore, this model allows us to state that the stiffness of the zone of impact between the firewall and the engine block has an influence on the Spüll and on the OLC for a frontal full-width impact.

Change of vehicle design - subframe front-end location

The third parameter on the stacking was the subframe front-end location. Only one value was assessed: a shift of 50 mm rearward of the front-end of the subframe. Table 9 presents the results.

Table 9.
Influence of subframe front-end location on OLC and Spüll parameters

		REFERENCE	SUBFRAME FRONT-END LOCATION INFLUENCE	
			50 mm X rearward subframe front-end location	% difference
OLC (g)	RIGHT	32,5	31,6	-3%
	LEFT	32,2	31,6	-2%
SPULL (W/kg)	RIGHT	3464,1	3287,1	-5%
	LEFT	3309,1	3213,0	-3%

This shift of 50 mm rearward of the front-end of the subframe decreases slightly the pulse severity.

This statement combined with the subframe force level one makes us conclude that to improve the small car, it is needed to re-design the subframe to better control OLC and Spüll.

Change of vehicle design - engine block location

The last parameter analysed in this study is the engine block location.
We applied a +/- 50 mm shift without changing the suspensions.
Table 10 presents the results for the small car.

Table 10.Influence of engine block location on OLC and Spüll parameters

		REFERENCE	ENGINE BLOCK LOCATION INFLUENCE			
			50 mm X forward	% difference	50 mm X rearward	% difference
OLC (g)	RIGHT	32,5	32,1	-1%	31,6	-3%
	LEFT	32,2	31,5	-2%	31,7	-2%
SPULL (W/kg)	RIGHT	3464,1	3415,1	-1%	3285,9	-5%
	LEFT	3309,1	3310,9	0%	3184,5	-4%

Shifting the engine block forward has very little influence on pulse severity.
Shifting it rearward is good for OLC and especially for Spüll. This is due to the fact that the level of deceleration is lower at the beginning of the crash and the impact duration is increased (2 ms more than the model of reference).
Therefore the engine block location is also a key parameter to control the pulse severity.

DISCUSSION AND LIMITATIONS OF THE STUDY

If we want to summarize the results presented in the previous chapter, we can have a look at the table below (Table 11).

Table 11. Summary of the analysis : effect of a change (delta) of magnitude in the highlighted parameters on OLC and Spüll parameters for the small car

Parameter	Delta param.	Deceleration	
		Decrease of parameter	Increase of parameter
Mass	*100 kg*	-	+
Subframe force level	*5 T*	++	-
Longitudinals force level	*2 T*		
Tunnel force level	*2 T*		
Engine block volume	*50 mm*	+	---
Firewall location	*20 mm*	+	--
Front-end subframe location	*20 mm*	+	
Engine block location	*20 mm*	--	+

And if we extend this summary to other car architectures not presented in details here, we can state that some parameters have strong influence on the pulse severity measured on a full-width rigid frontal impact. But depending of the characteristics of the reference model, some parameters do not need to be tuned because they are stiff or soft enough since the beginning. As an example, Table 12 presents the results for the sedan car.

Table 12.Summary of the analysis : effect of a change (delta) of magnitude in the highlighted parameters on OLC and Spüll parameters for the sedan car

Parameter	Delta param.	Deceleration	
		Decrease of parameter	Increase of parameter
Mass	*100 kg*	-	+
Subframe force level	*5 T*		
Longitudinals force level	*2 T*		
Tunnel force level	*2 T*		-
Engine block volume	*50 mm*	++	---
Firewall location	*20 mm*	+	--
Front-end subframe location	*20 mm*		
Engine block location	*20 mm*	-	+

On the other hand, there are some limitations that we should stress.
First of all, each parameter was assessed independently of the others whereas the combination could be logical and have a cumulative effect that could be non-linear.
A future analysis is planned to investigate the influence of combining the key parameters highlighted here.

A second limitation concerns the longitudinals. It was unexpected to see so little influence of the longitudinals stiffness on the pulse severity. It is guessed that an additional parameter: the change in the longitudinals kinematics would be of interest. The future analysis will take this into account as well.

Finally the consequence of changing or optimizing these key parameters to soften the pulse on the other type of impacts should also be assessed.
It is obvious but it is always good to stress that the design of a car in terms of passive safety is always a compromise between stiffness and intrusion.
Other type of crash (partial overlap) would increase the level of intrusion. The cockpit should always be preserved and intrusion strongly controlled.

CONCLUSION

This entire study was made to define the key parameters influencing the pulse severity measured in the cockpit on a full-with rigid 0° frontal impact.

The pulse severity was assessed via two scalars: OLC and Spüll that are used to design the restraint systems for different car architectures and for different type/age of occupants.

Tests were carried out on a fully instrumented load cell wall. These tests allowed us to get well correlated numerical model. In a first step, these models helped to identify the “a priori” key parameters that would influence the pulse severity via the study of their contribution to the overall Spüll.
Once these parameters were highlighted, the second phase of the analysis was to carried out a parametrical study to highlight the actual key parameters.
Some parameters were expected to be of first order and finally were not so influent. Others were highlighted and will be optimised to reach a satisfying pulse severity.
If we list the actual key parameters, we have:

- The subframe stiffness
- The firewall position
- The front-end position of the subframe

These are the ones linked to the kinematic behaviour of the engine block.

Finally, the longitudinals stiffness did not bring what was expected, and a further study is needed. It should aim at quantifying the influence of the key parameters when combined. And it should also aim at studying an additional parameter: the longitudinals kinematics.
This will be carried out in 2013 by PSA Peugeot Citroën.

ACKNOWLEDGMENTS

The authors wish to thank the internal PSA Peugeot Citroën Crash Test Centre, the Millbrook Crash Test Centre and the PSA Peugeot Citroën research teams and ACTOAT team that were involved in this study.
A special thanks to Loïc Grall who carried out the first part of this study.

REFERENCE

[1] China NCAP test protocol 2012 - http://www.c-ncap.org.cn/c-ncap_en/ep/2012english.pdf

[2] Euro NCAP Frontal Impact Working Group – draft protocol for full width test 2015.

[3] Safety Companion, Safety Wissen - Regulation and consumerism tests, 2013 edition

[4] J. Metzger, L. Kübler, S. Gargallo: Characterization and Evaluation of Frontal Crash Pulses for USNCAP 2011, Proceedings Airbag 2010 - 10th International Symposium and Exhibition on Sophisticated Car Occupant Safety Systems, 2010.

OBJECTIVE RATING METRIC FOR DYNAMIC SYSTEMS

Saeed Barbat
Yan Fu
Zhenfei Zhan
Ren-Jye Yang
Ford Motor Company
United States of America
Christian Gehre
PDB – Partnership for Dummy Technology and Biomechanics
Germany
Paper Number 13-0448

ABSTRACT

Computer Aided Engineering (CAE) has become a vital tool for product development in the automotive industry. Various computer programs and models are developed to simulate vehicle crashworthiness, dynamic, and fuel efficiency. To maximize the effectiveness and the use of these models, the validity and predictive capabilities of these models need to be assessed quantitatively.

For a successful implementation of CAE models as an integrated part of the current vehicle development process, it is necessary to develop an objective metric that has the desirable metric properties to quantify the discrepancy between physical tests and simulation results. However, one of the key difficulties for model validation of dynamic systems is that most of the responses are functional responses, such as time history curves. This calls for the development of an objective metric that can evaluate the differences of the time history as well as the key features, such as phase shift, magnitude, and slope between test and CAE curves.

In this paper, four state-of-the-art objective rating metrics are investigated. Multiple dynamic system examples for both tests and CAE models are used to show their advantages and limitations. Further enhancements are proposed to improve the robustness of these metrics. A new combined objective rating metric is developed to standardize the calculation of the correlation between two time history signals of dynamic systems. Multiple vehicle safety case studies are used to demonstrate the effectiveness and usefulness of the proposed metric for future ISO Technical Specification and Standard for the TC22/SC10/SC12/WG4 "Virtual Testing" Working Group.

INTRODUCTION

Prototype tests to evaluate safety performance of a new vehicle in order to meet current and future safety requirements are on the rise. Computer modeling and simulations are playing an increasingly important role in reducing vehicle prototype tests and shortening product development time. To achieve these goals, the validity and predictive capabilities of the computer models for various vehicle dynamic systems must be assessed objectively, quantitatively, and systematically.

Model validation is the process of comparing model outputs with experimental observations in order to assess the validity or predictive capabilities of computer models. The fundamental concepts and terminology of model validation have been established mainly by various standard committees and professional societies ([1], [2], [3], [4], [5]).

One of the critical tasks to achieve quantitative assessments of models is to develop a validation metric that has the desirable metric properties to quantify the discrepancy between functional or time history responses from both physical tests and simulation results ([6], [7], [8]). However, the primary consideration in the selection of an effective metric should be based on the application requirements. In general, the validation metric shall be a quantitative measurement to judge whether a computational model is adequate for its intended usage.

In this paper, four validation metrics for dynamic responses are investigated and they are: CORrelation and Analysis (CORA) metric [9], Enhanced Error Assessment of Response Time

Histories (EEARTH) metric [10], model reliability metric [11], and Bayesian confidence metric [12]. Several dynamic responses for both test and CAE model are used to show some limitations of these metrics. Further improvement of the CORA corridor rating and EEARTH metric are proposed to improve their robustness. Finally, a combined objective rating metric based on the improved CORA corridor metric and EEARTH is proposed to standardize the calculation of the correlation between two signals of dynamic systems. Multiple vehicle safety case studies are used to demonstrate the effectiveness and usefulness of the proposed metric for future ISO Standard.

SCOPE

The scope of ISO TC22/SC10/12/WG4 "Virtual Testing" Working Group was to provide a validated metric to calculate the level of correlation between two non-ambiguous signals (e.g. time-history signals) obtained from a physical test and a computational model of the same test. The defined metric shall be primarily aimed at vehicle safety applications.

The objective was to develop a fully documented metric instead of the development and provision of rating software.

This paper gives a general overview of the recent work. It is also an excerpt of the ISO documents ISO PDTR 16250 [13] and ISO TS 18751 [14] prepared by this expert group.

METHOD

The work on the new standard started with a literature review to determine the state-of-the-art metrics in this specific area. Black box approaches such as commercial rating software without fully documented algorithms or algorithms that are protected by intellectual property rights were excluded because of the aims of the ISO working group.

Ideal metric characteristics

There are many ideal metric characteristics that would be desirable in model assessment of dynamic systems ([6], [7], [8]). The most important ones for vehicle safety applications are:

(1) objective – produces same result regardless who conducts the assessment,

(2) generic – reflects differences in the full distribution of the simulation and experimental outcomes and key features like phase, magnitude, and slope,

(3) robust – produces consistant results with different sampling rates,

(4) symmetric – produces same result when the experiment and simulation outcomes switch,

(5) simple – easy to understand and use,

(6) contains clear physical meaning and Subject Matter Experts (SMEs)' knowledge,

(7) under uncertainty – accounts for data uncertainties in both the experiments and numerical simulations.

Pre-selected metrics

Based on the above ideal metric characteristics, four different metrics were considered for the future standard development by this expert group. An intense validation program helped to identify the most appropriate algorithms.

Algorithms that only analyze local features of a signal, e.g. peak, time of peak etc., are not considered. The approach of this working group was to develop a metric that analyzes complete signals including its local features.

CORA The objective rating tool CORA uses two independent sub-ratings, a corridor rating and a cross-correlation rating to assess the correlation of two signals [9].

The corridor rating calculates the deviation between both curves with the help of user-defined or automatically generated corridors. The cross correlation rating analyzes specific curve characteristics, such as phase shift, size, and shape of the signals. This combination of two completely independent ratings helps to compensate for each other's disadvantages.

The CORA rating tool is also trying to separate engineer's knowledge from the objective rating metric by using external parameters. It offers the possibility to fine-tune the evaluation to the specific needs of the applications by adjusting those metric parameters to reflect the SMEs' knowledge of the applications.

EEARTH The EEARTH metric is based on the Error Assessment of Response Time Histories (EARTH) [15] that provides three independent error measures: phase, magnitude, and topological. The phase error deals with the overall error in timing between two functional responses when considering all the points of the responses. Magnitude error is defined as the difference in amplitude of the two functional responses when there is no time lag between the two. Topological error deals with error associated with the shape of the functional responses, such as the number of peaks, valleys, and slope. A very unique feature of the EARTH metric is using dynamic time warping (DTW) to separate the interaction of phase, magnitude, and topological errors. DTW is an algorithm for measuring discrepancy between time histories and was first used in context with speech recognition in the 1960's [16]. The time warping technique aligns peaks and valleys as much as possible by expanding and compressing the time axis according to a given cost function [17]. Since the ranges of three errors are quite different and no single error can provide a quantitative model assessment alone, the original EARTH metric employs a linear regression method to combine the three errors into one score. A numerical optimization method is employed to identify the linear coefficients so that the resulting EARTH rating can match with the SMEs' ratings closely for a specific application. However, the resulting linear combination of the EARTH metric is mainly numerically based and application dependent, therefore, it may not be scalable to other applications.

In order to provide one intuitive rating and improve the robustness of the metric with different sampling rates while maintaining the advantages of the original EARTH metric, an enhanced EARTH metric called EEARTH is developed. The major enhancements include:

(1) developing an integrated calibration process to incorporate physical-based thresholds and SMEs' knowledge to provide phase score, magnitude score, slope score, and the combined EEARTH rating all in the standard “0” to “1” range;

(2) using a distance-only cost function for DTW instead of both distance and slope-based cost function in the original EARTH to improve the robustness of magnitude scores with different sampling rates;

(3) eliminating DTW on slope curves so that the slope error is calculated directly from the difference between the two slope curves calculated from the shifted and truncated test and CAE curves to improve the robustness of slope scores with different sampling rates.

Hence, the EARTH was enhanced by simplifying the algorithms and reducing the influence of the signal’s sampling rate on the rating score.

Model reliability metric A model reliability-based validation metric was developed for dynamic system applications [11]. The difference between CAE and test curves is taken as the validation feature. The threshold factor is defined by SMEs' experience, the lower and upper bounds of the threshold interval are defined as the product of the threshold factor and the absolute maximum amplitude of the reference signal. The model reliability metric is represented by the probability that the observed difference is within the lower and upper bounds of the threshold interval. If a pre-defined reliability target is met, the model is acceptable. Since this difference time-history curve has better normality than those of the test and CAE curves, a normal distribution of the difference can be assumed and the model reliability metric can be simply calculated.

There are only two adjusting parameters: threshold factor and reliability target, and both have clear physical meanings. The model reliability metric is one of the simplest metrics for dynamic system applications, and it is very easy to understand and interpret.

Bayesian confidence metric The Bayesian interval hypothesis testing method has been demonstrated to provide more consistent model validation results than a point hypothesis testing method [18]. Jiang and Mahadevan [19] derived a generalized explicit expression to calculate the Bayes factor based on interval-based hypothesis testing for multivariate model validation. Similar to the model reliability metric, the difference curve between the test and CAE curves is selected as the validation feature. After a prior density function is assumed, using Bayes’ theorem and assumptions given in [20] and [21], the Bayes factor for the multivariate case is equivalent to the volume ratio of the posterior density of testing data under null and alternative hypotheses.

The Bayesian measure of evidence that the computer model is valid may be quantified by

the posterior probability of the null hypothesis. Using the Bayes theorem, the confidence in the model based on the validation data can be obtained. Note that expert's opinion of the model accuracy may be incorporated in the confidence quantification in term of a prior ditribution. The decision maker or model user has to decide what threshold is acceptable.

Metric evaluation

Time history signals of forces, moments, accelerations, deflections, and angles are the most common types of signals obtained in vehicle safety applications. Various pairs of signals of those physical responses were used to analyze the pre-selected metrics in detail. The metrics must differentiate between different levels of correlation. Furthermore, they should use the whole domain of the rating scale, usually between "0" and "1". The assessment of the metrics was based on SMEs' experiences.

Selection of the most appropriate metrics

The Bayesian confidence metric and the model reliability metric can provide overall scores on whole time history curves, but they cannot identify key features like phase, magnitude, and slope.

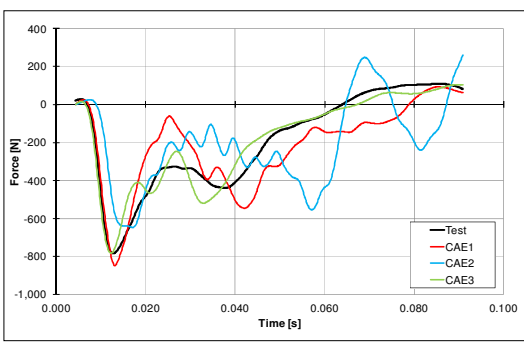

Figure 1. Force obtained in test and simulations.

The limitations of the CORA cross correlation and Bayesian confidence rating are shown in Table 1. The signals shown in Figure 1 are assessed by using the CORA and Bayesian confidence metrics. The signals are defined and evaluated in the plotted time domain.

The CORA cross correlation rating cannot differentiate between the three CAE signals because it requires signals that are defined before and beyond the interval of evaluation to calculate reasonable results.

Bayesian confidence metric grades the responses more dramatically and extremely. This is because the Bayesian hypothesis testing examines the mean of the difference distribution instead of the full difference distribution and the standard deviation of the mean of the difference is much smaller than the standard deviation of the difference. Therefore, it is more likely to give "1" score when the mean of the difference distribution is within the threshold interval, and give "0" score when the mean of the difference distribution is outside of the threshold interval.

Table 1.
Different metric ratings of force curves

	CAE1	CAE2	CAE3
CORA Total rating	0.452	0.371	0.577
CORA Corridor	0.654	0.491	0.903
CORA Cross correlation	0.250	0.250	0.250
Bayesian confidence rating	1	1	1

Since EEARTH analyzes the same characteristics of signals as the CORA cross correlation metric, but without this specific limitation, it was chosen as part of the proposed ISO metric.

Finally, two unique metrics, the CORA corridor metric and EEARTH were chosen for the proposed ISO metric.

PROPOSED ISO METRIC

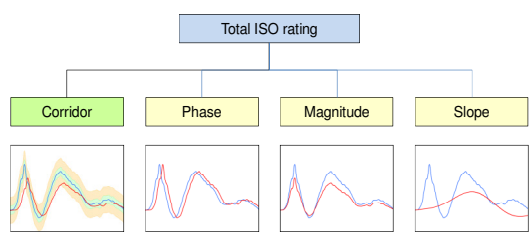

Figure 2. Structure of the proposed ISO metric.

The approach to the proposed ISO metric is to combine different types of algorithms to provide reliable and robust assessments of the correlation of two signals. The calculated score must represent a reasonable assessment for poor and for good correlations. As mentioned above, the

CORA corridor method and EEARTH are chosen. The new metric has been fully validated using responses from multiple vehicle passive safety applications.

Table 2.
Weighting factors of the sub-scores

Sub-metric	Weighting factor
Corridor	0.4
Phase	0.2
Magnitude	0.2
Slope	0.2

Figure 2 shows the structure of the proposed ISO metric. While the corridor method calculates the deviation between curves with the help of automatically generated corridors of constant width, the EEARTH method analyzes specific curve characteristics such as phase shift, magnitude, and shape. Hence, the proposed ISO metric has the advantage to compensate for the limitation of one algorithm by the other.

The total score of the proposed ISO rating metric adds up the four individually weighted sub-scores. The four weighting factors are shown in Table 2.

Corridor score

The corridor sub-metric calculates the deviation between two signals by means of corridor fitting. The two sets of corridors of constant width, the inner and the outer corridors, are defined along the test curve (reference). If the evaluated CAE curve is within the inner corridor bounds, a score of "1" is given and if it is outside the outer corridors, the score is set to "0". The assessment declines from "1" to "0" between the bounds of inner and outer corridors resulting in three different rating zones as shown in Figure 3. This transition is set to be quadratic for this proposed ISO metric.

The compliance with the corridors is calculated at each specific time of the whole interval of evaluation, and the final corridor score of a signal is the average of all scores at the specific times.

The absolute half width of the corridors is calculated by using the absolute maximum amplitude of the reference signal within the interval of evaluation and relative width factors of inner and outer corridors. The philosophy of the proposed ISO corridor approach is to use a narrow inner corridor and a wide outer corridor [22]. It limits the number of "1" ratings to only good correlations and gives the opportunity to distinguish between poor and fair correlations. If the outer corridor is too narrow, too many curves of a fair or moderate correlation would get the same poor rating of "0", like signals of almost no correlation with the reference.

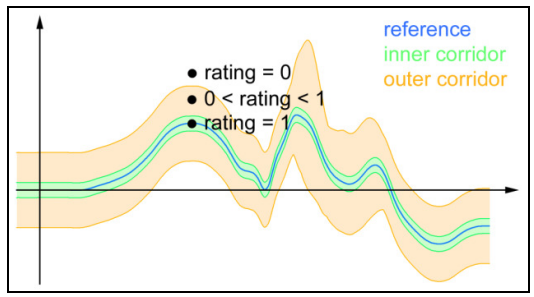

Figure 3. Rating zones of the corridor metric [9].

Phase score

The phase sub-metric is used to measure the phase lag between the two analyzed time histories. The maximum allowable percentage of time shift is pre-defined. In this step, the initial CAE curve is shifted left then right one step at a time to the original test curve, and the cross correlation between the truncated test curve and the shifted and truncated CAE curve is calculated until reaching the maximum allowable time shift limits. The best phase score is "1", which means there is no need to shift CAE curve to reach the maximum cross correlation between the initial test and CAE curves. If the time shift is equal to or greater than the maximum allowable time shift threshold, then the phase score is "0". In between, the phase score is calculated by a regression method.

Magnitude score

The magnitude sub-metric is a measure of discrepancy in the amplitude of the two time histories. It is defined as the difference in amplitude of the two time histories when there is no time lag between them. Before calculating the magnitude error, the difference between the time histories caused by error in phase is minimized by using DTW. The best magnitude score is "1", which means there is no difference in the amplitudes after phase shift and DTW. If the magnitude error is equal to or greater than the maximum allowable magnitude error threshold, then the magnitude score is "0". In between, the

magnitude score is calculated by a regression method.

Slope score

The slope sub-metric is a measure of discrepancy in slope curves of the two time histories. In order to ensure that the effect of global time shift is minimized, the slope curves are calculated from the truncated test curve and the shifted and truncated CAE curve. The best slope score is "1", which means there is no difference between the two slope curves. If the slope error is equal to or greater than the maximum allowable slope error, then the slope score is "0". In between, the slope score is calculated by a regression method.

Meaning of the results

The proposed total ISO rating R ranges from "0" to "1". The higher the rating the better the correlation of the two signals. This single-rating number can be transferred to a grade that represents the goodness of the correlation by using a sliding scale (Table 3).

Table 3.
Sliding scale of the proposed total ISO rating

Grade	**Rating** R
Excellent	$R > 0.94$
Good	$0.80 < R \leq 0.94$
Fair	$0.58 < R \leq 0.80$
Poor	$R \leq 0.58$

The thresholds of R of each grade were defined based on SMEs' experiences and are only valid if none of the parameters (e.g. weighting factors, regression schemes, sampling rates, etc.) described in the proposed ISO metric ([14]) are altered.

Excellent The characteristics of the reference signal is captured almost perfectly.

Good The characteristics of the reference signal is captured reasonably well, but there are noticeable differences between both signals.

Fair The characteristics of the reference signal is basically captured, but there are significant differences between both signals.

Poor There is almost no correlation between both signals.

VALIDATION OF THE PROPOSED ISO METRIC

Similar to the evaluation of the four pre-selected metrics to be considered for an ISO standard, the validation of the proposed ISO metric was conducted with similar sets of data.

Metric parameters

The proposed ISO metric and its sub-metrics offer several parameters to adjust and validate the rating results. They were mainly used to improve the resolution of the rating domain and to improve the differentiation between signals of a similar correlation. However, all parameters are fixed in the final proposed ISO metric to gurantee comparable rating scores.

Proposed total ISO rating The weighting factors of the four sub-scores (corridor, phase, magnitude, and slope) are the only parameters to adjust the total score.

Corridor score The widths of corridors are the most important parameters to adjust this rating results. The progression of the transition between inner and outer corridors has a considerable influence on the results as well.

The type of the corridors, constant or variable width, over whole time domain may change the outcome of this sub-metric significantly.

Phase score Two parameters are used to validate the phase sub-metric: the maximum allowable percentage of time shift and the progression coefficient for the transition between "1" and "0" rating scores.

Magnitude score Similar to the phase score, two parameters are mainly influencing the results: the maximum allowable magnitude error and a progression coefficient for the transition of rating between "1" and "0".

Slope score The maximum allowable slope error and a progression coefficient are the two parameters to adjust this sub-metric.

Pre-processing of the signals

During the evaluation and validation of the proposed ISO metric, it was concluded that a few basic conditions must be kept in order to obtain correct results. This must be done by the user.

Synchronization Initially, the signals must be synchronized by physical meanings and by its timing. At each time step of the test signal, a value of the CAE signal is required.

Sampling rate The proposed ISO metric was validated with signals of 10 kHz sampling rate. The sub-metrics to evaluate magnitude and slope are especially sensitive to the signal's sampling rate.

Filtering The algorithms do not modify the original signals. It should be considered that the calculation of the correlation could be difficult when using very noisy signals.

Figure 4 shows an example of the effect of filtering. Signals A and B are derived from the same unfiltered signal and differ only by the applied filter classes. The overall correlation rating of signal B increased by 6% compared to signal A due to the application of a higher filter class.

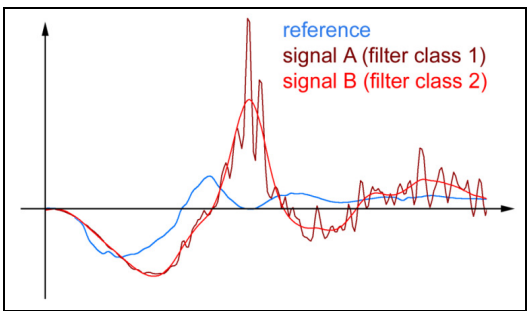

Figure 4. Differently filtered signals [9].

Interval of evaluation The assessment of the correlation should be focused on the relevant parts of the given signals. Typically, crash signals include pre-crash and post-crash phases that are usually not of interest and should be excluded from the rating. Therefore, an interval of evaluation shall be defined which describes the part of the signals that needs to be assessed. An assessment of using ratings of different sub-intervals of the same pair of signals is not allowed.

Figure 5 depicts an example of this problem. The correlation rating increases by 35% when extending the interval of evaluation from the relevant part to the whole time domain.

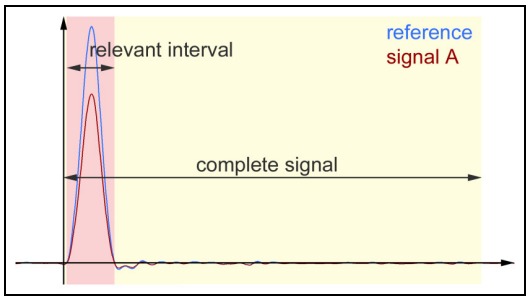

Figure 5. Different intervals of evaluation [9].

RESULTS

Four case studies that include different kinds of test and CAE signals are used to assess the potential of the proposed ISO metric. All cases are part of the mentioned ISO documents ([13], [14]) and they are defined and assessed in the time domain and fulfill all described requirements to pre-process the data.

Case 1

Figure 1 depicts a force response obtained in a test and the corresponding signals of three different CAE models. The proposed total ISO rating including the results of its sub-scores are shown in Table 4.

Table 4.
Rating of the force curves

	CAE1	CAE2	CAE3
Grade	Fair	Poor	Good
Proposed total ISO rating	0.711	0.460	0.862
Corridor score	0.654	0.492	0.904
Phase score	0.971	0.856	0.954
Magnitude score	0.738	0.372	0.929
Slope score	0.540	0.088	0.622

The rating scores reflects the different characteristics of the CAE curves. The low slope score of CAE2 correlates well with the clear shape difference of the signal compared to the test curve. The high phase score of all the CAE signals is mainly caused by the good agreement with the gradients of the signal's first peak. a The high magnitude score of CAE3 is because all peaks and valleys of the test curve are well captured. The corridor score assesses the deviation to the reference signal in the whole

time domain. CAE2 resulted in the worst rating among the three CAE signals because of the clear deviation from the test. Generally, the rating differentiates between the different kinds of correlation of the three CAE signals.

Case 2

Signals of a measured torque are shown in Figure 6. The correspondig rating scores are listed in Table 5.

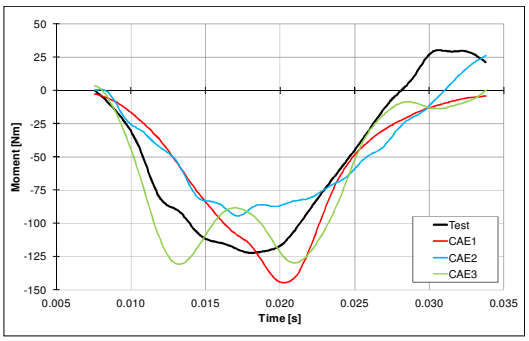

Figure 6. Moment obtained in test and simulation.

Table 5.
Rating of the moment curves

	CAE1	CAE2	CAE3
Grade	Fair	Fair	Fair
Proposed total ISO rating	0.657	0.660	0.666
Corridor score	0.539	0.538	0.556
Phase score	0.677	0.696	0.962
Magnitude score	0.840	0.798	0.735
Slope score	0.691	0.727	0.519

In spite of the different shapes of the three CAE signals, their objective rating scores are almost identical – "Fair". The twin peaks of CAE3 resulted in a low slope score. The high phase score of CAE3 is caused by the limited phase shift to reach the maximum cross correlation between test and CAE, even though the resulting maximum cross correlation number is low.

Case 3

Figure 7 shows a set of acceleration signals. The ratings are shown in Table 6.

The three CAE curves captured the gross characteristics of the test signal, but the peaks deviate. The phase and magnitude scores are the highest while the corridor scores show good correlation. The slope scores are low due to the noisy signals of the CAE curves.

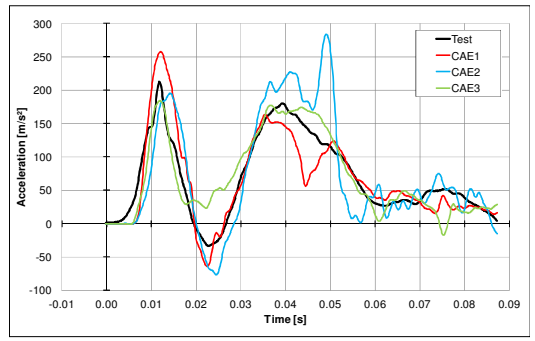

Figure 7. Acceleration obtained in test and simulation.

Table 6.
Evaluation the acceleration curves

	CAE1	CAE2	CAE3
Grade	Fair	Fair	Fair
Proposed total ISO rating	0.785	0.648	0.790
Corridor score	0.793	0.647	0.784
Phase score	0.971	0.909	0.989
Magnitude score	0.871	0.793	0.849
Slope score	0.498	0.246	0.546

This example shows that the combination of the four sub-metrics ensures reasonable ratings even if the signals are somehow difficult to handle for one of the sub-metrics.

Case 4

Figure 8 shows a set of displacement signals and Table 7 shows the corresponding rating scores.

The general characteristics of the four signals are almost identical. Therefore, the scores of phase, magnitude and slope are very high. The corridor metric does not differentiate between CAE2 and CAE3 because both signals are almost completely within the inner corridor that gives a score of "1".

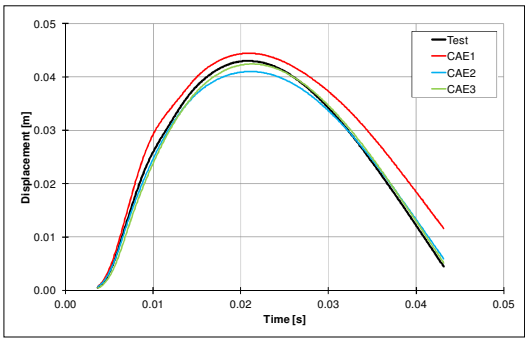

Figure 8. Displacement obtained in test and simulation.

Table 7.
Evaluation of the displacement curves

	CAE1	CAE2	CAE3
Grade	Good	Excellent	Excellent
Proposed total ISO rating	0.917	0.980	0.981
Corridor score	0.889	1.000	0.999
Phase score	0.911	0.962	0.937
Magnitude score	0.978	0.981	0.995
Slope score	0.918	0.957	0.976

CONCLUSION

This paper gives a brief overview of the capabilities of the proposed ISO metric. It is shown that the algorithms can handle different kinds of non-ambiguous signals of different qualities. The rating scheme is consistent and enables differentiated assessments of signals of different levels of correlation.

More detailed information and step-by-step procedures to implement the described metric in a software package are given in [13] and [14]. A set of ASCII curves to verify the implementation of the proposed metric is also provided with both ISO documents.

LIMITATIONS

The application of the developed metric requires some basic conditions:

(1) The metric is limited to non-ambiguous signals obtained from all kinds of tests associated with vehicle safety applications and the corresponding numerical simulations (CAE). The most commonly used signals in this field are time-history curves;

(2) The defined sliding scale to classify the proposed ISO rating score is only valid for the comparison of two signals. Any modification to the metric's parameters such as weighting factors, sampling rates, etc. requires a revision of the grade's thresholds;

(3) This proposed ISO metric is defined to calculate the level of the goodness of correlation between two signals only. If more than one pair of signals (e.g. whole set of signals from various channels of a test) is considered, the defined thresholds of the sliding scale are no longer valid.

REFERENCES

[1] Department of Energy – DOE; "Accelerated Strategic Computing Initiative (ASCI) Program Plan®"; Department of Energy; DOE/DP-99-000010592; Washington D.C.; USA; 2000.

[2] American Institute of Aeronautics and Astronautics – AIAA; "Guide for the Verification and Validation of Computational Fluid Dynamics Simulations"; American Institute of Aeronautics and Astronautics AIAA-G-077-1998; Reston; VA; USA; 1998.

[3] Department of Defense – DOD; "Verification, Validation, and Accreditation (VV&A) Recommended Practices Guide"; Department of Defense; Alexandria; VA; USA; 1996.

[4] American Society of Mechanical Engineers – ASME; "Guide for Verification and Validation in Computational Solid Mechanics"; American Society of Mechanical Engineers; ASME V&V 10; USA; 2006.

[5] American Society of Mechanical Engineers – ASME; "V&V 20-2009 Standard for Verification and Validation in Computational Fluid Dynamics and Heat Transfer"; available from ASME Codes & Standards website (June 28th 2012).

[6] Oberkampf, W. L.; "Overview of verification, validation and predictive capability"; Sandia National Laboratories; SAND2005-1824P; Albuquerque; NM; USA; 2005.

[7] Ferson, S., Oberkampf, W. L., Ginzburg, L.; "Model validation and predictive capability for the thermal challenge problem"; Computer Methods in Applied Mechanics and Engineering; 197 (29-32), pp. 2408-2430; 2008.

[8] Fu, Y., Zhan, Z., Yang, R.-J.; "A study of model validation method for dynamic systems"; SAE 101DM-0080; Detroit; MI; USA; 2010.

[9] Gehre, C., Gades, H., Wernicke, P.; "Objective Rating of Signals Using Test and Simulation Responses"; Paper Number 09-0407; 21st ESV Conference; Stuttgart; Germany; 2009.

[10] Zhan, Z., Fu, Y., Yang, R.-J.; "Enhanced Error Assessment of Response Time Histories (EEARTH) Metric and Calibration Process"; SAE 2011 World Congress; SAE 2011-01-0245; Detroit; MI; USA; 2011.

[11] Zhan, Z., Fu, Y., Yang, R.-J., Peng, Y.; "Development and Application of a Reliability-Based Multivariate Model Validation Method"; International Journal of Vehicle Design; 60 (3/4), pp. 194-205; 2012.

[12] Zhan, Z., Fu, Y., Yang, R.-J., Peng, Y.; "An Enhanced Bayesian Based Model Validation Method for Dynamic Systems"; ASME Journal of Mechanical Design; Vol.133, Issue 4, 041005; USA; 2011.

[13] International Organization for Standardization (ISO); "Road vehicles – Objective rating metrics for dynamic systems"; ISO/PDTR 16250; 2012.

[14] International Organization for Standardization (ISO); "Road vehicles – Objective rating metric for non-ambiguous signals"; ISO/TS 18571; draft; 2013.

[15] Sarin, H., Kokkolaras, M., Hulbert, G., Papalambros, P., Barbat, S., Yang, R.-J.; "Comparing Time Histories for Validation of Simulation Models: Error Measures and Metrics"; Transactions of the ASME – Journal of Dynamic Systems: Measurement and Control; Vol. 132, No. 6, 061401; 2010.

[16] Rabiner, L. R., Huang, B. H.; "Fundamentals of Speech Recognition"; Prentice Hall; 1993.

[17] Lei, H., Govindaraju, V.; "Synchronization of batch trajectory based on multi-scale dynamic Time Warping"; Proceedings of the Second International Conference on Machine Learning and Cybernetics; Xi'an; 2-5 November 2003.

[18] Jiang, X., Mahadevan, S.; "Bayesian risk-based decision method for model validation under uncertainty"; Reliability Engineering and System Safety; 92 (6), pp. 707–718; 2007.

[19] Jiang, X., Mahadevan, S.; "Bayesian wavelet method for multivariate model assessment of dynamical systems"; Journal of Sound and Vibration; 312 (4-5), pp. 694-712; 2008.

[20] Kass, R., Raftery, A.; "Bayes factors"; Journal of the American Statistical Association; 90 (430), pp. 773–795; USA; 1995.

[21] Migon, H. S., Gamerman, D.; "Statistical Inference-An Integrated Approach"; Arnold, a Member of the Holder Headline Group; London; UK; 1999.

[22] Kim, S.-A.; "Bewertung der Korrelation von Meßsignalen – Sensitivitätsanalyse der Steuerparameter der Bewertungssoftware CORA"; Master's thesis; TU Berlin; Germany; 2011.

REPEATABILITY OF IIHS SMALL OVERLAP FRONTAL CRASH TESTS

Becky C. Mueller, Christopher P. Sherwood, Joseph P. Nolan, and David S. Zuby
Insurance Institute for Highway Safety
United States
Paper Number 13-0079

ABSTRACT

This paper examines the repeatability of the Insurance Institute for Highway Safety's small overlap frontal crash test, based on repeated tests of six midsize vehicle models. Vehicle accelerations, structural measures, restraint system performance, dummy kinematics, and dummy injury measures were compared. Vehicle longitudinal acceleration pulses were similar in repeated tests of the same vehicle. The test-to-test differences of the least repeatable vehicle structural intrusion measurement targets ranged from 4 to 8 cm, with the vehicle models having higher levels of structural intrusion showing the most variation. Restraint system deployments were not always repeatable because many vehicle restraint systems were not yet tuned for this crash mode. In vehicles where restraint systems performed consistently, similar dummy kinematics was observed. Head, neck, chest, leg, and foot injury measures were similar in repeated tests for these vehicles. In the vehicle where the restraint system did not perform consistently, different dummy kinematics was observed. This resulted in large variations in femur, knee, and tibia injury measures.

None of these vehicles would have received different component or overall ratings whether the ratings were based on the results from the original or repeat test. The largest variations observed in this study were unimportant to the overall assessment of the vehicle, as measures from either test would promote the same design changes. Higher levels of variability likely reflect the fact that many of the vehicle structures and restraint systems were not specifically designed for this load case. Repeatability can be expected to improve as vehicles are redesigned to take the small overlap crash into account.

BACKGROUND

Crash tests are conducted for a variety of reasons including satisfying safety regulations, re-creating real-world crashes to better understand injury mechanisms, and comparing crashworthiness of vehicles in consumer evaluation tests. Consumer evaluation tests must be both representative of real-world crashes and designed to produce repeatable results leading to meaningful comparison of vehicle models. Due to time and monetary constraints, typically a single test of each vehicle model is conducted to obtain a rating; therefore, ensuring that results from a single test are representative of the vehicle's performance in similar configurations is important.

Previous studies have examined the crash test repeatability for full and moderate overlap frontal configurations. The National Highway Traffic Safety Administration (NHTSA) evaluated the repeatability and reproducibility of the 56 km/h (35 mi/h) full overlap New Car Assessment Program (NCAP) test through a series of twelve tests of the 1982 Chevrolet Citation (Machey and Gauthier, 1984). The recorded driver dummy head injury criterion (HIC) values varied up to 459 due to significant variation in head impact locations and dummy kinematics. Kinematics also was affected by variations in occupant compartment intrusion, steering wheel deformation, and inconsistent routing of the dummy's shoulder belt. The large variation in HIC values would have resulted in a different vehicle rating for two of the tests. These findings may be less relevant when considering modern vehicle construction methods, advanced restraint systems and lessons learned about crash test procedures since this research was conducted.

The European Experimental Vehicle Committee (EEVC) Working Group 11 collected data evaluating the repeatability of a 56 km (35 mi/h) moderate overlap deformable barrier (ODB) test, showing that the ODB configuration was a more structurally repeatable crash mode than NCAP-style rigid barrier impacts. (Hobbs and Williams, 1994). Three tests of a midsize car were conducted, showing good repeatability in vehicle responses and dummy sensor measurements. The difference between highest and lowest test measurements was 53 for driver HIC values and 5kN for peak femur forces. Variations in femur loading were attributed to different interactions with the knee bolster. None of the variations in sensors resulted in a different evaluation of the dummy.

Additional studies showing good repeatability of the ODB test mode were submitted to the EEVC Working Group 11 by Bundesanstalt für Straßenwesen (BASt, 1994; Lowne, 1996) and Japanese Automo-

bile Standards Internationalization Center (JASIC) (Oki, 1995). BASt tested three midsize hatchback cars, and JASIC tested four midsize cars. These studies compared measurements between tests using the coefficient of variation (standard deviation as a percentage of the mean measured value). Both studies found that dummy head and chest sensors had good repeatability, with coefficients of variation below 10%. Leg sensor measures were less repeatable, with coefficients of variation up to 185%, mainly due to different leg interactions with the knee bolster. The majority of intrusion measures were repeatable, with only a localized area of the occupant compartment showing high levels of variation. Both studies found high coefficients of variation, up to 320%, for the steering column.

The Insurance Institute for Highway Safety (IIHS) evaluated the repeatability of the 64.4 km/h (40 mi/h) moderate overlap deformable barrier crash test based on seven pairs of vehicles across a range of classes (Meyerson et al., 1998). Peak vehicle accelerations were within 8 g between paired vehicles. The least repeatable structural intrusion measures exhibited test-to-test differences that ranged 3-11 cm across the seven vehicle models. Only one vehicle model received a different structural rating due to variations of 5-8 cm at every location. Restraint system performance, including airbag deployment and seat belt spoolout, were reasonably repeatable. Frontal airbag deployment times were within 4 ms within each pair except one, where deployment varied by 12 ms. This vehicle also had the largest difference in peak vehicle acceleration. Total seat belt spoolout varied up to 2 cm. Differences in steering column deformation were only significant for the evaluation of two vehicles, which had high levels of intrusion. Differences in dummy kinematics were limited to different rebound impacts; none of which would have resulted in a different assessment of head injury.

Driver dummy head, chest, femur, knee, and foot injury measures were reasonably repeatable. Differences between repeated tests ranged 17-73 for HIC, 3-6 mm for chest deflection, 0.1-0.8 kN for femur forces, 1-3 mm for knee displacements, and 3-33 g for foot acceleration. None of these measures resulted in a different evaluation of injury risk for a given sensor. The largest difference between repeated measures of the tibia index was 0.8, and two of the vehicles received a different evaluation of injury risk for the tibia. Only one vehicle model would have received a different overall evaluation due to different ratings of both structure and dummy leg sensors.

This study examines the repeatability of six midsize vehicle models tested in the IIHS small overlap crash mode based on comparisons of vehicle accelerations, structural measures, restraint system performance, dummy kinematics, and dummy injury measures.

METHODS

IIHS conducted repeat tests on pairs of the 2012 Volvo S60, 2009 Mitsubishi Galant, 2012 Audi A4, 2012 Acura TSX, and 2012 Acura TL, as well as three tests of the 2009 Ford Fusion at a nominal speed of 64.4 km/h (40 mi/h) and a nominal 25% overlap with the IIHS small overlap barrier. All tests and measurements followed the IIHS (2012a) small overlap test protocol. Table 1 lists the vehicle test weights, impact speeds and measured overlaps. The largest differences between repeated tests were 63 kg for weight, 0.2 km/h for impact speed, and 2 percentage points for overlap with the barrier.

Vehicle Response Measures

Longitudinal and lateral acceleration histories were obtained from a triaxial accelerometer array mounted in the rear floorpan of the vehicles. In some vehicles, acceleration measures could not be used as an indicator of overall vehicle motion because deformation near the sensor's mounting occurring late in the crash event changed its orientation from the vehicle's frame of reference; therefore, analysis of the high-speed video footage was used to determine longitudinal delta-V, in the laboratory reference frame.

Table 1.
Repeated small overlap frontal crash tests

Vehicle	Test	Test weight (kg)	Impact speed (km/h)	Percent overlap (%)
Ford Fusion	A	1,619	64.3	25
	B	1,679	64.3	24
	C	1,616	64.4	25
Mitsubishi Galant	A	1,662	64.1	25
	B	1,656	64.3	27
Volvo S60	A	1,729	64.2	25
	B	1,766	64.2	25
Audi A4	A	1,753	64.4	25
	B	1762	64.3	25
Acura TL	A	1,840	64.2	25
	B	1,863	64.2	25
Acura TSX	A	1,733	64.2	25
	B	1,748	64.2	25

Occupant Compartment Intrusion

Occupant compartment intrusion was characterized by pre- and post-crash measurements of nine intrusion targets in two zones, the lower occupant compartment (lower hinge pillar, footrest, left toepan, brake pedal, and rocker panel) and upper occupant compartment (steering column, upper hinge pillar, upper dash, and left instrument panel), shown in Figures 1-2. Locations of these intrusion targets are defined in the IIHS (2012a) small overlap test protocol. In several vehicles (Fusion tests A, B and C; Galant tests A and B; S60 test A), the upper and lower hinge pillar, rocker panel, and upper dash locations were similar to but not exactly the same as the locations defined in the protocol.

Restraint System Response

Restraint system responses were compared for the S60, TL, and TSX pairs. For the Galant and Fusion tests, different sized dummies were used in each test. In one of the A4 tests, the airbags did not deploy because the airbag control module shut down after being powered for too long without vehicle motion. Seat belt tensioner firing and airbag deployment times (frontal, side curtain, and side torso airbags) were compared using high speed video footage. An additional optical belt spoolout sensor was installed in the TL and TSX pairs to compare dynamic seat belt movement. Steering wheel stability in vertical and lateral directions was assessed using pre- and post-crash measurements of the steering column intrusion target.

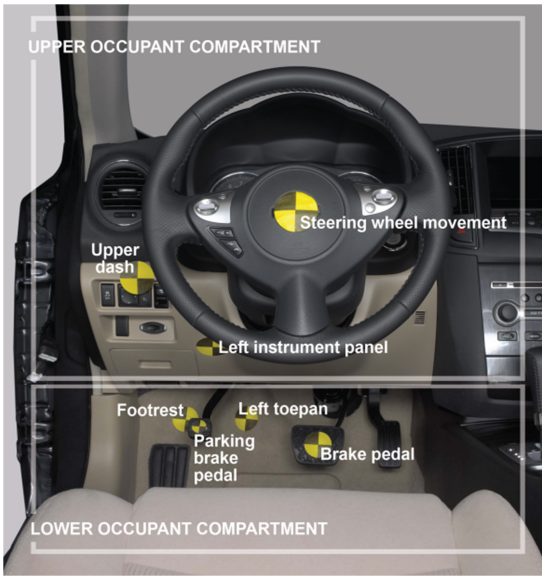

Figure 1. Driver seat view of occupant compartment intrusion targets

Dummy Response

An instrumented Hybrid III midsize male dummy was installed in the driver seat for all tests except two of the Fusion tests in which different dummies were used. All dummies were seated according to the University of Michigan Transportation Research Institute seating procedure (IIHS, 2004), and grease paint was applied to the dummy head to determine head contact locations, according to the IIHS (2012a) small overlap test protocol. Dummy kinematics and sensor measurements could only be compared for the S60, TL, and TSX pairs. Dummy instrumentation included sensors in the head, neck, chest, and lower extremities. Dummy kinematics was compared using high-speed video footage and contact evidence from paint transfer.

RESULTS

Vehicle Response Measures

Vehicle acceleration and velocity responses are compared in Table 2. The largest difference in peak longitudinal acceleration between repeated tests was 6 g for the Acura TSX pair. The corresponding longitudinal and lateral histories are shown in Figures 3 and 4. The acceleration curves were similar until the front wheel interacts with the barrier at 44 ms. In test A, the wheel is driven rearward for 16 ms before rotating outboard and detaching from the vehicle, whereas in test B, the wheel begins rotating at first contact with the barrier and remains attached to the vehicle throughout the crash.

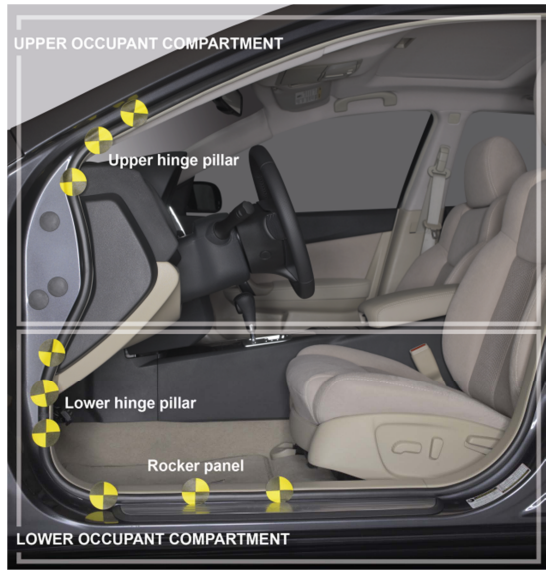

Figure 2. Door frame view of occupant compartment intrusion targets

Table 2.
Vehicle response

Vehicle	Test	Peak longitudinal acceleration (g)	Longitudinal delta-V (km/h)
Ford Fusion	A	-25	39.6
	B	-25	41.4
	C	-26	45.0
Mitsubishi Galant	A	-27	57.6
	B	-24	57.6
Volvo S60	A	-24	47.7
	B	-27	50.4
Audi A4	A	-22	54.0
	B	-22	54.9
Acura TL	A	-22	37.8
	B	-25	39.6
Acura TSX	A	-27	49.5
	B	-33	52.2

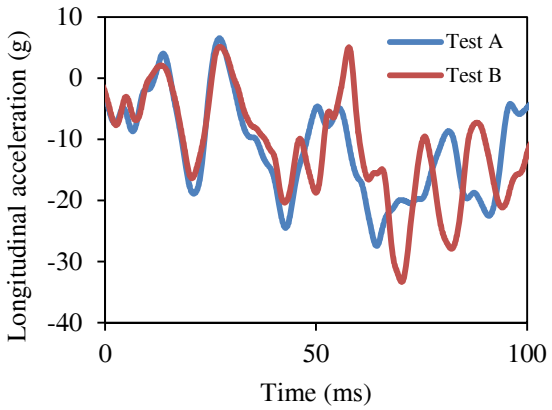

Figure 3. Acura TSX vehicle longitudinal acceleration.

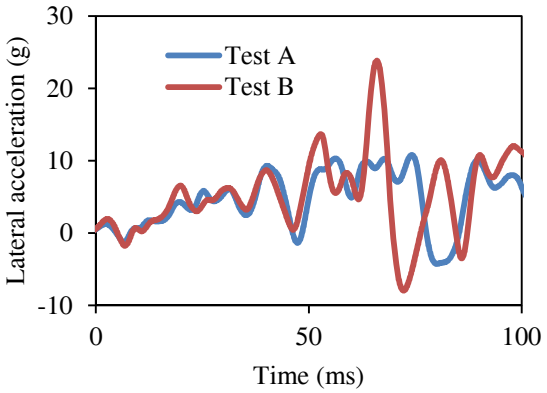

Figure 4. Acura TSX vehicle lateral acceleration

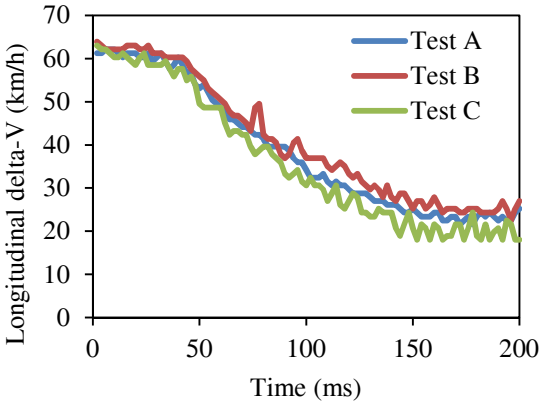

Figure 5. Ford Fusion vehicle longitudinal delta-V

The greatest variation in longitudinal delta-V of 5 km/h was observed in the Ford Fusion tests, shown in Figure 5. This variation mainly is attributed to differences in wheel interaction with the barrier starting at 140 ms.

Occupant Compartment Intrusion

Occupant compartment intrusion measurements for all vehicle sets are listed in Appendix A. The average intrusion, difference between tests at the most variable intrusion target, and coefficient of variation at the most variable target (standard deviation as a percentage of the mean measured value) are listed for all vehicles in Table 3. Vehicles with higher overall levels of intrusion tended to have the most variation. The maximum coefficients of variation for the Fusion, S60, and TSX occurred at the steering wheel, while the rocker had the greatest variation for the TL. At these locations, intrusions measures were all below 6 cm.

Table 3.
Variation in occupant compartment intrusion measures

Vehicle	Average intrusion (cm)	Maximum variation (cm)	Maximum coefficient of variation (%)
Ford Fusion	15	6	143
Mitsubishi Galant	14	4	40
Volvo S60	4	4	108
Audi A4	20	8	30
Acura TL	8	5	86
Acura TSX	11	4	86

The largest and smallest differences between repeated tests for each structural intrusion target location are shown relative to that location's good boundary in Figure 6. Six of the nine smallest test-to-test differences did not have variation; the remaining three locations varied between 1-3 cm. The Fusion accounted for six of the nine largest test-to-test differences and had levels of intrusion that exceeded the good boundary at three locations. The A4 accounted for the largest variation of 8 cm at the left instrument panel, where measures from either test were more than twice the good boundary.

A vehicle structure rating is determined based on the guidelines for rating occupant compartment intrusion in the IIHS (2012b) small overlap rating protocol. The lower occupant compartment and upper occupant compartment each receive a subrating and the structural component rating is the worse of the two subratings. A comparison of subratings for the upper and lower occupant compartment and structural rating is shown in Table 4. The upper and lower occupant compartments received the same ratings for each vehicle except for the TSX pair. In the TSX pair, the lower occupant compartment received different ratings between tests because the lower hinge pillar intrusion was 4 cm greater in test A, resulting in a marginal rating for that target compared with an acceptable rating in test B. The different lower occupant compartment subrating did not affect the structural component rating of the TSX because the worse of the two subratings was from the vehicle's upper occupant compartment.

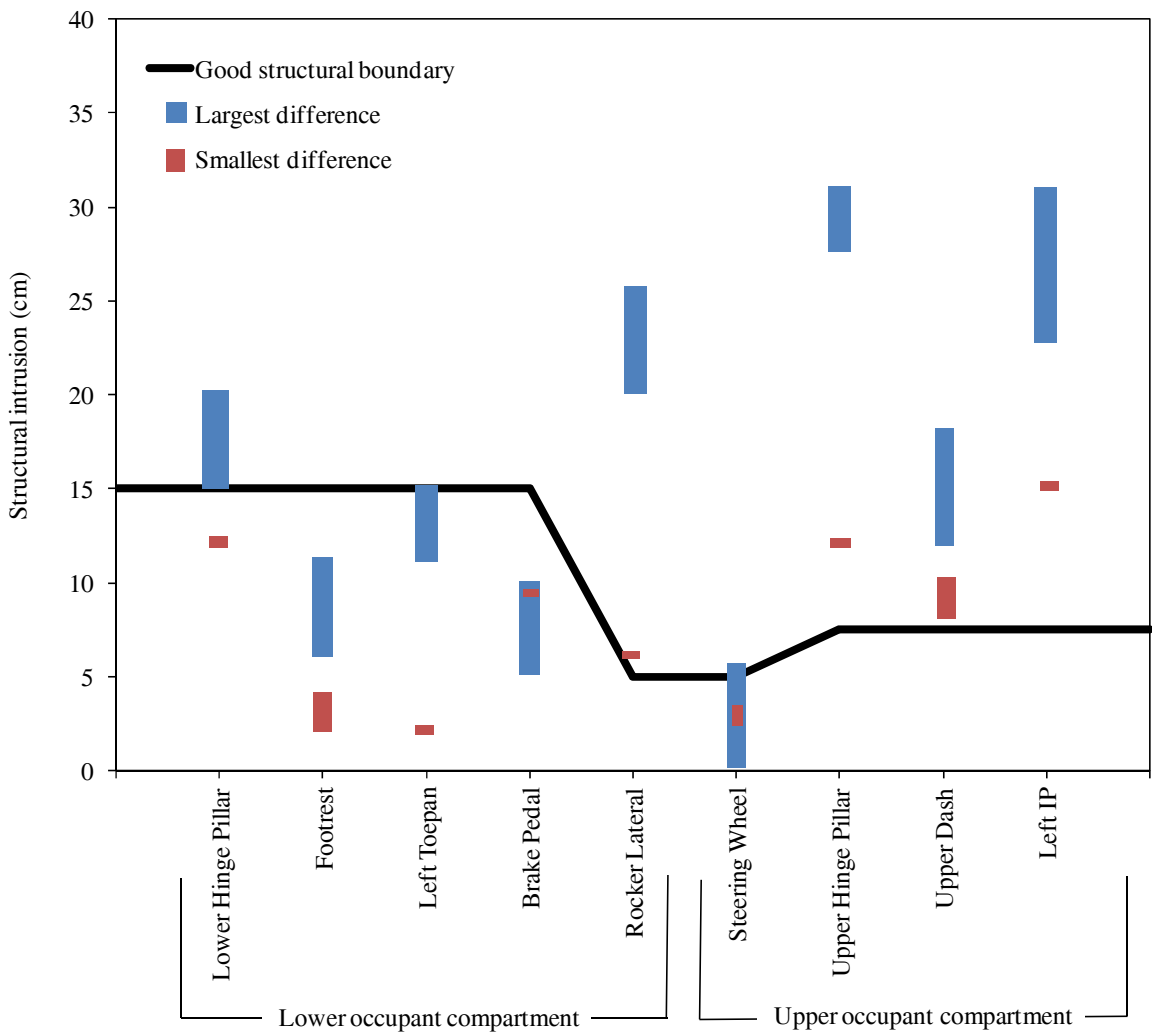

Figure 6. Variability in occupant compartment intrusion targets

Table 4.
Vehicle structural ratings

Vehicle	Test	Occupant compartment Lower	Occupant compartment Upper	Overall
Ford Fusion	A	Marginal	Poor	Poor
	B	Marginal	Poor	Poor
	C	Marginal	Poor	Poor
Mitsubishi Galant	A	Marginal	Marginal	Marginal
	B	Marginal	Marginal	Marginal
Volvo S60	A	Good	Good	Good
	B	Good	Good	Good
Audi A4	A	Acceptable	Poor	Poor
	B	Acceptable	Poor	Poor
Acura TL	A	Good	Acceptable	Acceptable
	B	Good	Acceptable	Acceptable
Acura TSX	A	Acceptable	Marginal	Marginal
	B	Good	Marginal	Marginal

Restraint System Response

Restraint system timings for the S60, TL, and TSX pairs are shown in Table 4. For the S60, all deployment times of the seat belts and airbags were within 4 ms of the original test. For the TL, the frontal airbag and seat belt deployments were consistent in timing, but the side curtain and thorax airbags varied by 8 and 10 ms, respectively. For the TSX, only the belt pretensioner deployed consistently. In test A, the frontal airbag deployed 18 ms earlier than in test B. The side curtain and side thorax airbags deployed during test A but not during test B. Data provided by the manufacturer suggested that lateral acceleration in test A was just above the threshold to deploy the side airbag system, whereas lateral acceleration in test B was just below the threshold. This variation in lateral acceleration occurring around 36 ms was not discernible in the lateral acceleration history shown in Figure 4.

Table 5
Restraint system deployment timing

Vehicle	Test	Pre-tensioner (ms)	Deployment of airbag: Frontal (ms)	Deployment of airbag: Side curtain (ms)	Deployment of airbag: Side thorax (ms)
Volvo S60	A	14	34	34	94
	B	12	34	36	98
Acura TL	A	26	34	40	44
	B	26	34	32	34
Acura TSX	A	26	32	36	38
	B	26	50	n/a	n/a

Deformation of the steering column is listed in Table 6. Deformation in both the vertical and lateral directions was within 4 cm between paired vehicles. Based on contact evidence and video footage, variation in steering wheel deformation may have contributed to differences observed in the dummy's interaction with the frontal airbag, as described in the Dummy Kinematics section.

Table 6.
Steering column deformation

Vehicle	Test	Vertical (cm)	Lateral (cm)
Volvo S60	A	2	0
	B	4	0
Acura TL	A	6	5
	B	10	4
Acura TSX	A	9	13
	B	8	9

Seat belt displacement for the TL and TSX pairs is shown in Figure 7. For the TL pair, seat belt displacement was similar throughout the duration of the crash. For the TSX pair, test A allowed 2 cm greater belt spoolout than test B. This difference in spoolout may be explained by variation in the occupant interaction with the frontal airbag, as described in the Dummy Kinematics section.

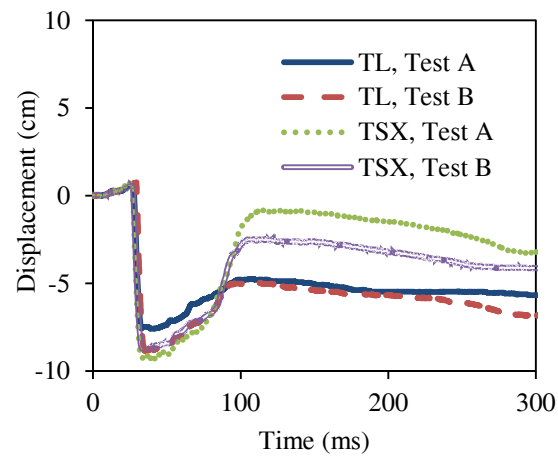

Figure 7. Acura TL and TSX seat belt displacements

Dummy Kinematics

In the S60, TL, and TSX vehicles, the dummy heads contacted the front and side curtain airbags. No hard contacts with vehicle structures were observed. A summary of contact times with these airbags is listed in Table 7. In the S60 and TL pairs, the head contact

times with both airbags were within 5 ms. In the TSX tests, the contact times varied by 6 ms.

Table 7
Dummy head contact timing

Vehicle	Test	Contact with frontal airbag (ms)	Contact with curtain airbag (ms)
Volvo S60	A	85	65
	B	80	66
Acura TL	A	72	50
	B	72	48
Acura TSX	A	70	100
	B	76	n/a

In the S60 and TL tests, dummy contact evidence on the frontal airbag showed similar paint transfer on comparable locations of the frontal airbag. Figure 8 shows the different dummy contact evidence on the frontal airbag in the TSX tests. In test A, the right-most edge of the dummy's face contacted the airbag 6 cm farther outboard than test B. Only the right side of the head was loaded by the airbag in test A, whereas both sides of the head were loaded in test B. This may be partially due to the differences in steering wheel lateral deformation between tests. The non-deployment of the curtain airbag in test B did not appear to result in additional lateral movement of the dummy. The off-center airbag interaction observed in test A may have placed additional loading on the belt system, resulting in more shoulder belt spoolout evidenced by the seat belt displacement sensor. Rebound kinematics was similar for all pairs.

In the S60 and TL tests, dummy leg contact evidence on the knee bolster showed similar paint transfer on comparable locations of the knee bolster. Different lower extremity kinematics was observed in the TSX pair. In test A, primarily, the lower part of the leg interacted with the knee bolster, whereas in test B, the knee and upper leg also had significant interaction with the knee bolster. The differences in seat belt loading and dummy head and torso kinematics contributed to these variations.

Figure 8. Post-crash paint evidence on front airbag in Acura TSX test A (left) and test B (right). Left side of head is pink; right side of head is blue.

Dummy Sensor Measurements

Injury measures for the S60, TL, and TSX pairs are listed in Appendix B. The largest and smallest differences between repeated tests of each injury measure were shown as a percentage of each sensor's injury assessment reference value (IARV) and are compared in Figure 9. The smallest test-to-test differences showed no variation for nine sensors. The remaining six sensors showed variation ranging 2-10% of the sensor's IARV, with the largest variation occurring at the left lower tibia index, where either measure resulted exceeded the IARV. The largest test-to-test differences showed variations of 2-75% of the sensor's IARV. Notable differences in dummy leg kinematics for the TSX pair contributed to the large differences in left tibia forces, left knee displacement, and right femur forces, although the latter did not contribute to a significant assessment of injury risk according to the knee-thigh-hip criteria (Kirk and Kuppa, 2009). The left upper tibia force and left knee displacement sensors would have received different evaluations of injury risk. These differences did not affect the leg injury evaluation, as the rating was based on the left lower tibia force sensor which received a poor rating for both tests.

Vehicle Ratings

A summary of component and overall evaluation ratings for the S60, TL, and TSX is shown in Table 8. Overall ratings were calculated using the weighting principles outlined in the IIHS (2012b) small overlap rating protocol. For each vehicle, repeat tests resulted in identical component and overall ratings.

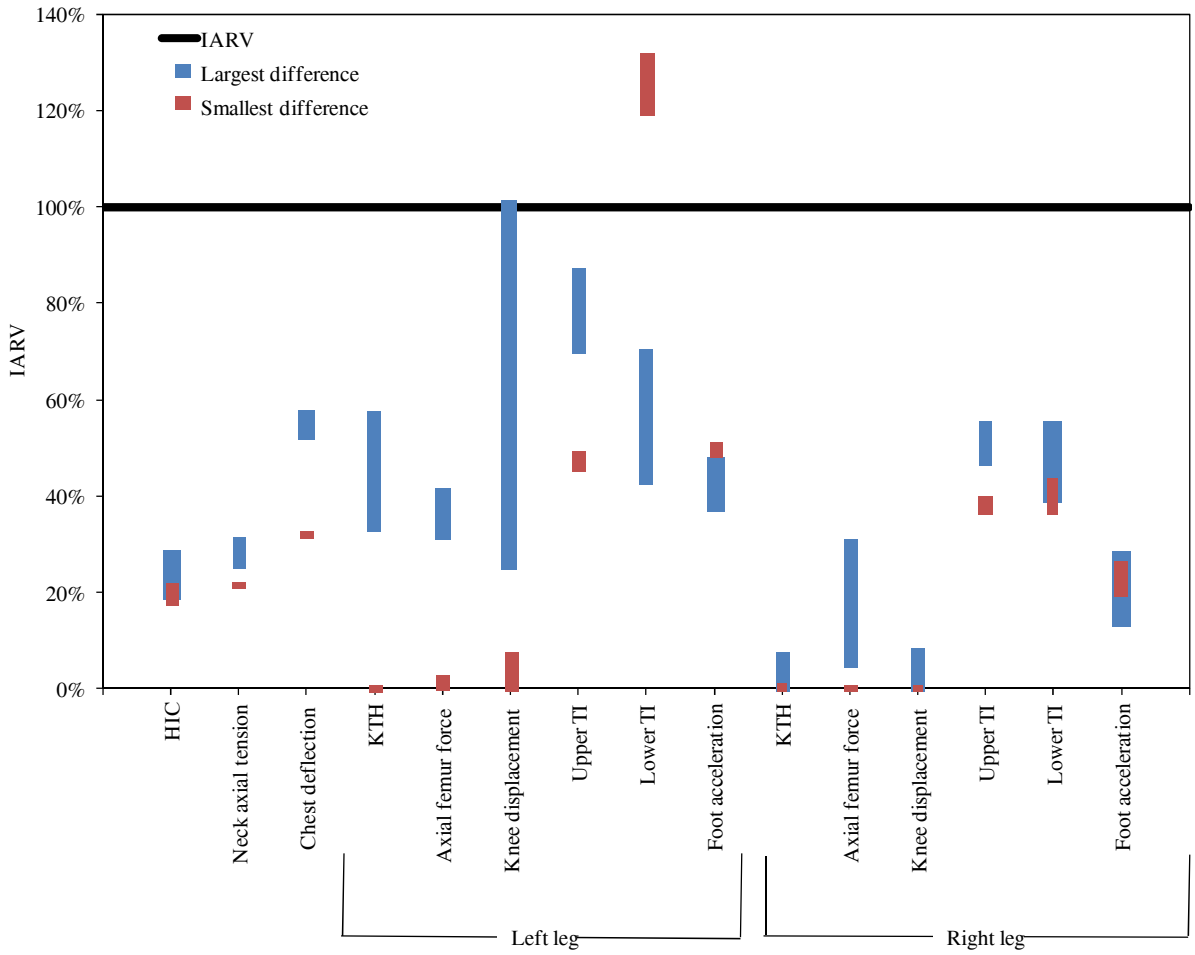

Figure 9. Variability in dummy sensor measurements

Table 8
Component and overall ratings

	Test	Structure	Restraints and kinematics	Dummy injury measures				Overall
				Head/neck	Chest	Thigh/hip	Leg/foot	
Volvo S60	A	Good	Acceptable	Good	Good	Good	Good	Good
	B	Good	Acceptable	Good	Good	Good	Good	Good
Acura TL	A	Acceptable	Good	Good	Good	Good	Good	Good
	B	Acceptable	Good	Good	Good	Good	Good	Good
Acura TSX	A	Marginal	Acceptable	Good	Good	Good	Poor	Marginal
	B	Marginal	Acceptable	Good	Good	Good	Poor	Marginal

DISCUSSION

The current study found similar or lower levels of test-to-test variation in small overlap tests compared with full and moderate overlap tests when considering vehicle accelerations, structural measures, restraint system performance, dummy kinematics, and dummy injury measures. Vehicle acceleration was more repeatable than observed in the moderate overlap test (Meyerson et al., 1998). Structural intrusion also was more repeatable than observed in studies of the moderate overlap test. Three of the seven vehicle models examined in the moderate overlap study (Meyerson et al., 1998) had maximum variations of intrusion greater than observed for all models in the current study. In the moderate overlap study, one vehicle model had high levels of variation at every intrusion location and would have been assigned a different rating between paired vehicles. In the current study, the highest levels of variation occurred at localized areas in the occupant compartment, and none of the vehicle models would have been assigned a different rating between paired vehicles. The largest coefficients of variation for structure were lower than reported by BASt (1994) and Oki (1995). These coefficients of variation were observed at the rocker panel and steering column, where all intrusion measure were below 6 cm and variations did not affect the rating of the individual intrusion target.

Restraint system and dummy kinematic repeatability were similar to those observed in moderate overlap tests. Variation in timing of the airbags and belt tensioners, overall belt spoolout, and steering column deformation were similar to those observed in the moderate overlap tests (Meyerson et al., 1998). Dummy head and torso kinematics were more repeatable than observed in the moderate overlap test because no significant variation in rebound kinematics was observed. In both small and moderate overlap evaluations, the greatest differences reported for dummy kinematics involved the lower extremities due to different interactions with the knee bolster.

Repeatability of the dummy sensors compared with those in full and moderate overlap tests was mixed. Dummy head and chest measures were significantly more repeatable than those observed in full and moderate overlap tests. These sensors also indicated a lower risk of injury than those observed in the other crash modes. Dummy leg sensor measures showed a similar range of repeatability as those observed in the moderate overlap studies by Lowne (1996), BASt (1994), Oki (1995), and Meyerson et al. (1998), with little variation for some vehicle models and significant variation in others. The S60 and TL pairs showed similar leg sensor measures and all indicated a low risk of injury, whereas the TSX pair showed large variations, leading to different assessments of injury risk for the knee and upper tibia index. These differences did not affect the component rating of the leg, as measures from the lower tibia index received a poor rating in both tests. All variations in foot acceleration were significantly less than those observed in the moderate overlap tests.

The small overlap test-to-test variation observed in this study of six midsize cars produced reasonably repeatable vehicle evaluations. Although variations observed in full and moderate overlap tests sometimes resulted in an overall change in rating for a vehicle, all vehicles in this study would have received the same component and overall ratings whether the evaluation was based on the original or repeated test.

Designing vehicles to exhibit low injury measures on dummies and low levels of occupant compartment intrusion has led to significant safety improvements in the modern fleet. Studies have found that vehicles receiving a higher rating in both NHTSA and IIHS crash test programs correlate to a reduced injury risk. Kahane et al. (1994) found that occupants of vehicles receiving a good NCAP rating have a 15-25% lower risk of fatal injury in a frontal crash compared with vehicles receiving lower scores. Similarly, Farmer (2005) found that occupants of vehicles receiving a good IIHS moderate overlap rating have a 74% lower risk of fatal injury in a head-on crash than vehicles receiving a poor rating.

The evaluation of repeatability was limited to a study of six midsize car models. Repeatability was assessed on pairs and triples of midsize cars based on availability, and the small number of repeat tests do not represent a comprehensive study of repeatability. Dummy kinematics and sensor measurements could be compared for a limited number of the test pairs. Results for the midsize cars may not reflect the variability observed in other sizes or types of vehicles.

CONCLUSIONS

Some vehicle structure measures, restraint system performance, and dummy injury measures were less repeatable than others. The large variations observed were mainly in locations where the proportionally large variations are unimportant to the overall assessment of the vehicle, as measures from either test would promote the same design changes. Variations in airbag deployments and resulting dummy kinematics will be resolved as restraint systems are specifically tuned for this load condition.

REFERENCES

Bundesanastalt für Straßenwesen. 1994. Report on frontal impact test on VW Golf VR6 at 40 percent overlap with EEVC deformable barrier (56 km/h). Collaborative Frontal Impact Test Programme, Part Sponsored by the European Commission, Germany.

Farmer, C.M. 2005. Relationships of frontal offset crash test results to real-world driver fatality rates. *Traffic Injury Prevention* 6:31-37.

Hobbs A, Williams D. 1994. Development of the frontal offset deformable barrier test. Paper no. 94-S8-O-06. *Proceedings of the 14th ESV International Technical Conference*. Washington, DC: National Highway Traffic Safety Administration.

Insurance Institute for Highway Safety. 2004. Guidelines for using the UMTRI ATD positioning procedure for ATD and seat positioning (version V). Arlington, VA.

Insurance Institute for Highway Safety. 2012a. Small overlap frontal crashworthiness evaluation crash test protocol (version I). Arlington, VA.

Insurance Institute for Highway Safety. 2012b. Small overlap frontal crashworthiness evaluation rating protocol (version I). Arlington, VA.

Kahane, C, Hackney, J., and Berkowitz, A. 1994. Correlation of vehicle performance in the New Car Assessment Program with fatality risk in actual head-on collisions. Paper no. 94-S8-O-11. *Proceedings of the 14th International Technical Conference on the Enhanced Safety of Vehicles*, Washington, DC: National Highway Traffic Safety Administration.

Kirk, K. and Kuppa, S. 2009. Application and evaluation of a novel KTH injury criterion for the Hybrid III dummy in frontal crash test environments. Paper no. 09-0196. *Proceedings of the 21th ESV International Technical Conference*. Washingtion, DC: National Highway Traffic Safety Administration.

Lowne R. 1996. The validation of the EEVC frontal impact test procedure. Paper no. 96-S3-O-28. *Proceedings of the 15th ESV International Technical Conference*. Washingtion, DC: National Highway Traffic Safety Administration.

Machey J, Gauthier C. 1984. Results analysis and conclusions of NHTSA's 35 mp frontal crash test repeatability program. SAE Technical Paper 840201. Warrendale, PA: Society of Automotive Engineers.

Meyerson S, Zuby D, Lund A. 1998. Repeatability of frontal offset crash tests. *Proceedings of the 16th ESV International Technical Conference*. Paper no. 98-S11-O-02. Washingtion, DC: National Highway Traffic Safety Administration.

Oki, K. 1995. Research for frontal impact test method in Japan. Paper presented at the EEVC WG11 meeting, Volvo Safety Center, Gothenburg, Sweden.

APPENDIX A.
OCCUPANT COMPARTMENT INTRUSION MEASUREMENTS

Table A1.
Occupant compartment intrusion measurements

Vehicle	Test	Lower hinge pillar (cm)	Footrest (cm)	Left toepan (cm)	Brake pedal (cm)	Rocker lateral (cm)	Steering wheel (cm)	Upper hinge pillar (cm)	Upper dash (cm)	Left instrument panel (cm)
Ford Fusion	A	9	13	11	5	21	0	30	12	19
	B	13	17	14	8	25	2	31	18	20
	C	10	16	15	9	24	5	28	16	21
Mitsubishi Galant	A	12	18	11	8	23	2	12	16	15
	B	12	22	14	12	22	3	12	18	15
Volvo S60	A	6	3	3	3	5	1	6	3	3
	B	8	5	4	5	3	3	7	6	5
Audi A4	A	27	29	20	10	4	16	26	30	31
	B	24	26	18	10	3	13	24	26	23
Acura TL	A	15	11	2	4	5	2	9	9	10
	B	20	6	2	5	2	3	12	11	10
Acura TSX	A	25	13	4	6	5	2	12	14	18
	B	21	11	6	9	5	5	15	16	15

APPENDIX B
DUMMY SENSOR MEASUREMENTS

Table B1.
Dummy head, chest, and lower extremity sensor measurements

		Volvo S60		Acura TL		Acura TSX	
Measurement		**A**	**B**	**A**	**B**	**A**	**B**
HIC		148	136	68	98	145	193
Axial tension (N)		1	0.9	0.7	0.7	1.1	1.1
Flexion moment (Nm)		34	48	12	27	28	31
Chest deflection (mm)		-16	-16	-25	-27	-27	-28
KTH (%)	Left	0	0	1.7	2.8	0.9	0.4
	Right	0	0	0	0	0	0.3
KTH location	Left	Femur/knee	Femur/knee	Femur/knee	Femur/knee	Femur/knee	Femur/knee
	Right	Femur/knee	Femur/knee	Femur/knee	Femur/knee	Femur/knee	Femur/knee
Axial femur force (kN)	Left	-0.3	-0.16	-4.28	-4.89	-3.66	-3.01
	Right	0	0	-0.16	-0.13	-0.55	-2.7
Knee displacement (mm)	Left	0	-1	-10	-5	-4	-15
	Right	0	0	0	0	1	0
Upper tibia index	Left	0.54	0.45	0.48	0.47	0.72	0.86
	Right	0.48	0.54	0.42	0.48	0.38	0.37
Lower tibia index	Left	0.69	0.44	0.51	0.37	1.31	1.21
	Right	0.4	0.54	0.32	0.44	0.38	0.43
Foot acceleration (g)	Left	31	42	75	73	71	58
	Right	32	39	40	23	55	60